AN ABSTRACT OF THE DISSERTATION OF

YunJi Choi for the degree of Doctor of Philosophy in Civil Engineering presented on March 8, 2018.

Title: Numerical Investigations on Sewer Geysers

Abstract approved: _____

Arturo S. Leon Sourabh V. Apte

A sewer geyser is a series of ejecting air-water mixture eruptions through vertical shafts of drainage systems. In field observed geyser incidents, manhole covers were blown into the air and they were followed by ejecting air-water mixture eruptions that lasted for several seconds at a time. Trapped air in sewer systems during the transition between open channel flow to pressurized flow and its release processes are known to play an important role in causing sewer geysers. There is a lack of detailed three-dimensional numerical simulation of the sewer geyser phenomena using techniques that can capture air-water interactions. The present study attempts to fill this gap. A Finite Volume (FV) and three-dimensional computational fluid dynamics (3D-CFD) model was used and the simulation method was validated by numerically reproducing physical experiments on spring-type geysers and violent geysers. A qualitative assessment of the flow features present in the system during a violent geyser eruption was made and compared with the physical experiment. The flow was approximated using the Reynolds-Averaged Navier-Stokes (RANS) model and the air-water interface was modeled using the Volume of Fluids (VOF) method. The $k - \varepsilon$ turbulence closure model was used. A numerical experiment

was performed to identify the influence of the initially available air and water in a sewer system on the geyser formation.

Numerical Investigations on Sewer Geysers

by

YunJi Choi

A DISSERTATION

submitted to

Oregon State University

in partial fulfillment of
the requirements for the
degree of

Doctor of Philosophy

Presented March 8, 2018
Commencement June 2018

Doctor of Philosophy dissertation of YunJi Choi presented on March 8, 2018.

APPROVED:

Co-Major Professor, representing Civil Engineering

Co-Major Professor, representing Civil Engineering

Director of the School of Civil and Construction Engineering

Dean of the Graduate School

I understand that my dissertation will become part of the permanent collection of Oregon State University libraries. My signature below authorizes release of my dissertation to any reader upon request.

YunJi Choi, Author

ACKNOWLEDGEMENTS

My sincere gratitude must be expressed to my graduate committee, Dr. Sourabh Apte, Dr. Daniel Cox, Dr. Arturo Leon, Dr. John Sessions, Dr. Harry Yeh, and Dr. Solomon Yim. Thank you for your comments and time. The School of Civil and Construction Engineering has provided me with endless support through this journey. If Dr. Apte's research group, Computational Flow Physics Laboratory at Oregon State University, had not granted me an access to the High-Performance Computing (HPC) Cluster, the majority of the simulations presented in this work would not have been possible. My sincere gratitude goes to them as well. Thank you, Dr. Jack Istok for encouraging me to keep try and helping me through the writing process. Thanks to my friends and colleagues who cheered me through this journey. Nate, Randy, Michelle, Parnian, Harry, and Jeff, I thank you from the bottom of my heart. Thomas, Jeremy, Choko, and Uyu, you babies have brought much love and sunshine to my life. Mommy loves you very much. More than ten years ago, my best friend Liz, Mr. and Mrs. Bedell accepted me to their home with an open heart. Mr. and Mrs. Bedell taught me how to drive, brought me to their family gatherings, and looked after me as if I was their own daughter. I could not have asked for a more loving home away from home. Finally, I would like to dedicate my work to my mom, KyungSoon Lee and my brother, Hoon Choi.

TABLE OF CONTENTS

TABLE OF CONTENTS (Continued)

LIST OF FIGURES

LIST OF FIGURES (Continued)

LIST OF FIGURES (Continued)

LIST OF FIGURES (Continued)

LIST OF FIGURES (Continued)

LIST OF FIGURES (Continued)

LIST OF FIGURES (Continued)

LIST OF TABLES

LIST OF APPENDIX FIGURES

LIST OF APPENDIX TABLES

Chapter 1: Introduction

A sewer geyser is a series of ejecting air-water mixture eruptions through vertical shafts of drainage systems. In field observed geyser incidents, manhole covers were blown into the air and they were followed by ejecting air-water mixture columns that lasted for several seconds at a time (Figure 1.1). Trapped air in sewer systems during the transition between open channel flow to pressurized flow and its release process are known to play an important role in causing sewer geysers (Guo and Song, 1991; Wright, Lewis, and Vasconcelos, 2010; Lewis, 2011; Vasconcelos and Wright, 2011; Shao and Yost, 2013).

Previously reported physical experiments were able to demonstrate that entrapped air in sewer systems lead to pressure transients and abrupt overflows (Holley, 1969; Hamam and McCorquodale, 1982; Zhou, Hicks, and Steffler, 2002a). However, a sufficiently large scale experiment that was able to produce erupting sewer geysers as observed in the field, have not been carried out till 2015. In addition, conducted numerical simulations lack in numerical complexity and covered extent of the computational domain (Zhou, Liu, and Ou, 2011a; Shao and Yost, 2013; Muller, Wang, and Vasconcelos, 2017). This is because high fidelity simulations are computationally expensive and their accessibility only recently improved so that they could be used for detailed numerical investigations.

In the following sections of this document, a number of steps made to numerically simulate sewer geysers are presented. In Chapter 1, the background of the topic is presented through a list of field observed cases and some key terms are defined. In Chapter 2, past literature studying mechanisms of sewer geyser are discussed, knowledge gap are identified and research questions are stated. In Chapter 3, numerical simulation

Figure 1.1: Snapshots of field observed violent geysers at the interaction of 35th st and I-35W. Both incidents were observed during the month of July, but five years apart. (a) was observed on July 3rd, 1999 and (b) was observed on July 11th, 2004 (StormChasingVideo, 2012). Both incidents involved eruptions exceeding 20-30 ft in height.

methods are validated by reproducing published physical experiments. Qualitative and quantitative characteristics of the numerical simulation were compared with the reported results of the physical experiments. In Chapter 4, a system of numerical simulations are presented. The simulation results were then analyzed to show that the violent geyser eruption evolution can be influenced by the vertical shaft height and/or amount of air initially exist in a system. In Chapter 5, a conclusion of the overall study is drawn and recommendations are made for a direction of the future research.

1.1 Background

Under heavy rainfall conditions, the capacity of combined sewer systems (CSSs) can be exceeded and result in combined sewer overflows (CSOs). Trapped air during the filling of CSSs may lead to violent eruptions through drop shafts. These events are termed as sewer geysers. There are similar natural phenomenon which result in ejecting air-water mixture column, such as geothermal geysers (Figure 1.2) and blowholes at the shores of volcanic islands (e.g. Hawaii, Australia, etc., Figure 1.3). Circumstances that lead to geothermal geysers and blowholes are worth examining as the mechanisms of these natural events can be analogous to those involved in sewer geysers.

The shape and pattern of eruption due to sewer geyser resembles that of the Old Faithful geyser located in Yellowstone National Park, WY (Staff, 2015). Naturally occurring geothermal geysers are known to be induced by geological and hydrothermal conditions (White et al., 1975). Shown in Figure 1.4, during its recovery or recharge stage, hot water fills up the subsurface cavity and cooler water accumulates near the surface. Most volcanic gases reside near the surface in pores. During the preliminary eruption stage, a contraction point along the geyser tube accumulates air in a bubble.

Figure 1.2: A picture of an Old Faithful geyser eruption, Yellowstone National Park, WY (Staff, 2015).

Figure 1.3: A picture of Hãlona Blowhole an Oahu, HI (Gopackup, 2017).

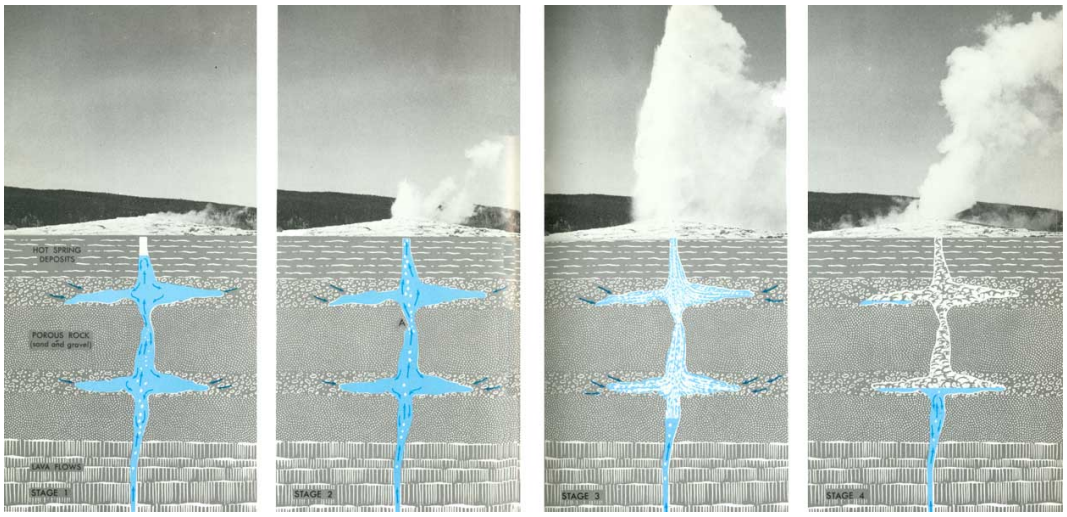

Figure 1.4: A diagram outlining the four stages of a geothermal geyser occurrence; (1) recovery or recharge stage, (2) preliminary eruption stage, (3) full eruption stage and (4) steam stage (USGS, 2007)

The accumulated air bubbles abruptly exit the tube and some water bursts out of the outlet at the top. During the full eruption stage, the decreased hydrostatic pressure causes a rapid vaporization of the fluid (i.e. flash steam). This directly results in the great expansion of the mixture volume in the cavity and tall eruptions of gas-liquid mixture take place. Depending on the size and characteristics of the particular geothermal geyser, the eruption height and frequency can vary. Once the stored gas, liquid and their mixture are exhausted, the ejecting eruption subsides and the subsurface tube and chambers recharges. Then, the eruptive cycle of a geothermal geyser repeats.

While blowholes are caused by mechanisms that do not involve vaporization, they also include multiphase flow interaction and similar eruption formation of the geothermal and sewer geysers. During high tides, a large wave surge striking the rocky shore maybe followed by an erupting air-water mixture through an outlet located at a higher elevation.

For the blowhole eruption to develop, the rocky shore must develop a characteristic blowhole cave geometry through slow erosion over time. Impinging wave surges can fill the entire cross section of the cave entrance and this pressurizes the blowbole cave. The combination of transient pressure oscillation caused by the impact force of the incoming wave and bubbly flow caused by the breaking wave results in accelerating overflow through the outlet.

Sewer geyser occurs in man-made structures such as combined or separated sewer systems. The mechanisms leading to geysering are relatively unknown, even though geysering in sewer systems have been studied for over 30 years. With the increase of rain fall intensity, a result of climate change in some cases, and a growing urban population, the manifestation of sewer geysers are on the rise. Sewer geysers have been observed in cities such as Hamilton, Ontario; Chicago, Illinois; Edmonton, Alberta; Minneapolis, Minnesota, etc. (Hamam and McCorquodale, 1982; Guo and Song, 1991; Zhou et al., 2002a). Perhaps the most well known example occurred in Minneapolis, MN, where a video security footage of sewer geyser demonstrates that intense sewer geysers have sufficient force to blow manhole covers into the air and eject high air-water mixture columns (Figure 1.1). A notable characteristic of these sewer geysers is that the second or third eruptions typically achieve the maximum height than the initial eruption. The maximum eruption is followed by smaller subsequent eruptions until the stored air and water are exhausted.

Additional field sewer geysers videos can be found on the internet using search terms such as sewer geyser, sewer overflow, manhole cover launch, etc. Among the accessible videos online, two distinctive patterns of overflow are observed. Regardless of the amount of overflow, ejecting intensity or the size of the shaft, one group of overflows appeared to be entirely due to exceeded system capacity (Figure 1.5). The overflowing liquid

Figure 1.5: An example of liquid volume displacement sewer overflow from the Canon Ave storm sewer system (JS4IV, 2013).

appeared to be entirely comprised of liquid with some sedimentation, judging by the color of the overflow. In these cases, no significant mixing between air and water was observed and the ejecting column maintained a steady height until the excess water was exhausted. The other group of overflows involved ejecting air-water mixture columns spraying out of manholes (Figure 1.6). A series of upward impulses can be observed.

In Tacoma, WA, two adjunct manholes experienced geyser events during a single rain storm (annotated as boxes A and B in Figure 1.7). In the beginning, both of the manholes experienced sewer geysers simultaneously. Later, each manhole alternated the eruption incidents. As evident in the video, geyser eruptions can occur in individual drop shafts as well as in one or more neighboring drop shafts.

Figure 1.6: An example of ejecting air-water mixture overflow observed in downtown Houston, TX (NYCYankinTexas, 2012).

In contrast to previous speculations by Wright et al. (2010); Vasconcelos and Wright (2011), arguing that a system must be significantly larger for high intensity geysers to occur, violent geysers have occurred in small systems with pipe diameters under 12". In the case of the sewer geyser observed in Tualatin, OR, the vertical shaft experiencing intense geyser eruption is smaller than 10 inches in diameter (Figure 1.8).

As previously presented examples of sewer geyser confirm, the magnitude of observed incidents range from rattling manhole covers with spewing mist to ejecting air-water mixture columns exceeding 30 m above ground level. Violent sewer geysers often result in costly pipe failures and fractures due to its destructive nature and should be avoided for public safety and the fundamental integrity of the country's infrastructure (Landers, 2006).

Some attributed severe infrastructure damage, such as fracturing of water mains,

Figure 1.7: Sewer geyser observed at the intersection of Pacific Ave and S Tacoma Way, Tacoma, WA (screenflot, 2013).

Figure 1.8: A sewer geyser event observed in Tualatin, OR. The video begins with the vertical shaft cover rattling and the cover eventually becomes displaced during the on set of the ejecting overflow. Based on the surrounding objects, the cover appears to be no larger than 12 inches in diameter (Harms J, 2013).

to high pressure transients associated with these flow phenomena (City of Edmonton, 1995). The pressure transients in sewer systems are believed to be caused by entrapped air pockets (Hamam and McCorquodale, 1982; City of Edmonton, 1995; Zhou, Hicks, and Steffler, 2002a; Vasconcelos and Wright, 2011). Entrapped air pockets can be formed in horizontal pipes for various reasons; a sudden boundary condition change, instabilities at the air-water interface and uneven filling of horizontal pipes.

Lewis (2011) stated that geysers are poorly understood and no fundamental study on constituting mechanisms of the flow has been performed. Only recently, a set of successful physical experiments were carried out by Elayeb (2016). Intense sewer geysers were captured under a controlled laboratory setting. The sewer geyser eruption height exceeded 30 m in some experiment trials. The observed flow interactions were highly unsteady and vigorous mixing between air and water occurred in the vertical shaft.

According to Leon (2018), mechanisms that lead to violent sewer geyser are partly originated from instabilities present in the connected horizontal pipes. Gravity drives the flow in the horizontal pipe until an entrapped pocket reaches a vertical pipe. In the vertical pipe, mostly buoyancy drives the rise of air. During the air pocket rise, some water from the liquid column above falls around the periphery and accumulate at the tail end of the air pocket. Vigorous mixing between the falling water and the rising air occurs. As the air pocket reaches to the top of the vertical pipe, the remaining water above the air pocket overflows. The reduced mass of water above the rising air increases the pressure gradient between the vertical and the horizontal pipes and accelerates the air flow into the vertical pipe. In the meantime, at the air-water interface in the horizontal pipe, growth of wakes due to the Kelvin-Helmholtz instability result in formation of slugs. The slugs rapidly propel into the vertical pipe and violently erupt.

The overall objective of this study was to perform numerical simulations to capture

violent geyser eruptions and qualitatively analyzing the affect of two system variables, initially available volume of water in the vertical pipe and air in the system, on the sewer geyser occurrence.

Chapter 2: Motivation

2.1 Introduction

Previously, an introduction to the sewer geyser phenomenon was laid out by examining video records of actual sewer geyser events. Qualitative observations of various forms of sewer geysers were discussed. The current section will serve as the motivation to numerically investigate further into the mechanisms of sewer geysers. Technical terms used throughout the study are defined and contributing mechanisms of sewer geyser are listed using academic literature. The knowledge gap in the existing literature are identified and research questions are put forth.

2.2 Survey of previous research

Preceding observations and experimental investigations hypothesized and confirmed a number of physical processes involved in sewer geysers. Although the investigations did not necessarily result in production of sewer geyser eruptions, relevant processes included the presence of entrapped air volume as a result of the drainage system filling processes (Hamam and McCorquodale, 1982; Wright, Lewis, and Vasconcelos, 2010), the entrapped air migration and surging in horizontal pipes (Holley, 1969; Zhou, Hicks, and Steffler, 2002b), and air-water release through vertical shafts (Vasconcelos and Wright, 2011). In the case of numerical investigations, a few approached the problem using the one dimensional momentum equation (Guo and Song, 1991; Zhou, Hicks, and Steffler,

2004a) and some considered the two way interaction between the entrapped air and water (Vasconcelos and Wright, 2011; Li and McCorquodale, 1999). Computational fluid dynamics modeling of the multiphase flow interaction has only been attempted recently and is still in its infancy (Shao and Yost, 2013; Choi, Leon, and Apte, 2014).

Experimental investigations on geysers

Sewer systems generally operate under free-surface flow conditions. In some situations, e.g., large storm events, rapid filling, flow obstruction due to debris, etc., the flow regime in a sewer system can transition from free-surface flow to pressurized flow. The air entrapment and flow regime transition due to rapid system filling were studied by Wright, Vasconcelos, Creech, and Lewis (2008); Wright, Lewis, and Vasconcelos (2010); Lewis (2011). The unpredictable nature of the drainage system filling process caused by rainfall and runoff timing, natural and artificial terrain variety, and varying infiltration conditions within a region, can lead to change in boundary conditions. This is followed by transition of flow regime from open channel to pressurized flow. During the transition, air can be entrapped in parts of a sewer system. In the experiment of Hamam and McCorquodale (1982), the instability at the air-water interface caused air entrapment and notable pressure fluctuations throughout the system.

Further investigations led to a conclusion that the entrapped air can influence the pressure oscillations and the maximum observed pressure peaks. Albertson and Andrews (1971) numerically and experimentally studied pressure transients caused by air release from pipelines. The physical experiment configuration experienced air leakage through an orifice at the top of a vertical pipe. The air leakage was followed by oscillating pressure waves caused by a surge front impinging on the orifice plate. The observed maximum pressure transient was fifteen times the initial static pressure in the system.

Holley (1969) experimentally observed the release of entrapped air through a vertical pipe. The air release created a temporary unsteadiness in the system. This unsteadiness was reflected in the measured pressure throughout the system. The magnitude of the oscillations was proportional to the amount of air entrapped, but not proportional to the liquid flow rate in the pipe system. The study concluded that under pressurized flow condition, entrapped air in sewer systems can amplify pressure transients. Zhou et al. (2002a) conducted experiments using a rapidly filling horizontal pipe containing entrapped air and its leakage through an orifice. The experiment revealed that the observed peak pressure in the system was a function of an optimal orifice size that allowed effective air release while providing a sufficient surface area to act as an obstruction to pressure waves. The findings resulted in a numerical model also.

Despite the previous attempts, the experiment of Elayeb (2016) was the first time violent geysers resembling those recorded in actual stormwater and combined sewer systems were created in an experimental setting. In the experiment, the vertical pipe length was varied and the longer vertical pipes achieved higher geyser heights as long as the air supply was not limited. Leon (2018) experimentally demonstrated the process of violent geyser eruption in six distinctive steps; (i) air is entrapped in a horizontal pipe and the air expands towards the vertical pipe looking for an alleviation, (ii) the entrapped air begins to flow into the vertical pipe and rises through the vertical pipe in a Taylor bubble-like form that fills the bulk of the vertical pipe cross-section, (iii) water spills over the vertical pipe outlet. This reduces the pressure above the rising air and results in an accelerated air flow into the vertical pipe. With the increased air velocity, Kelvin-Helmholts instability is found at the air-water interface in the horizontal pipe, (iv) wakes in the air-water interface grows and slugs are formed in the horizontal pipe. The slugs enter the vertical pipe in an accelerated manner as the air-water mixture continues to unloads at the top

of the vertical pipe. At this point, violently erupting geysers are observed, (v) as the acceleration of slugs in the horizontal pipe continues, subsequent eruptions , often with higher velocity, are observed, and (vi) finally, after several eruptions, the system becomes depressurized and no more eruptions are observed.

Although a relatively smaller scale, Cong et al. (2017) was able to produce able to produce a spring-type overflow which lacks spraying eruptions of a violent geyser. The experiment found that given the same vertical shaft length, a smaller pipe diameter is more likely to result in geyser overflows. While the resulting geyser eruption forms were significantly different between Elayeb (2016), Leon (2018) or Cong et al. (2017), one may conclude that, smaller diameter or "slender" vertical shafts are generally more susceptible to geyser eruptions assuming the supply of air in the system is not limited. Previously discussed experimental studies hypothesized that to achieve high pressure peaks in a conduit system, a number of conditions must be met. Those conditions include sufficient supply of entrapped air, air-water interface instability in the horizontal pipe, a convoluted outlet condition that allows venting and flow obstruction at the same time, and a particular diameter of the vertical shaft.

Numerical representation of spring-type eruption in sewer systems

Guo and Song (1991) showed using a mathematical model, that the water level in a vertical pipe can rise above the ground surface exclusively due to pressure oscillations in the connected horizontal pipes. However, one can argue that if there had been entrapped air in their system, the flow condition would have become more dynamic. For example, Lewis (2011) analyzed field collected pressure measurements and concluded that if the violent geyser was induced by the impact force of water only, the pressure and velocity in the horizontal pipe should have been significantly higher than what was actually

observed.

According to available literature, the presence of an entrapped air pocket and its release mechanism play important roles when numerically simulating pressure oscillations in pipe systems. A number of efforts have been made to numerically simulate this process. Vasconcelos and Wright (2011) performed experiments studying entrapped air release through a vertical pipe. Given a conduit system consisted of horizontal pipe and a vertical pipe and filled with standing water, a limited amount of pressurized air was released from a side of the horizontal pipe. The initially pressurized air expanded, accumulated at the pipe crown and released through the connected vertical pipe. The pressure oscillation in the horizontal pipe and the rising trajectory of the air pocket were analyzed.

The study proposed a numerical model that simulated the pressurized air release through the vertical pipe. The numerical model assumed that the falling volume of water around the periphery of the large air pocket was directly proportional to the amount of air displacement in the vertical pipe. The upward motion of the water column due to the rising air expansion was disregarded and water was assumed to be incompressible. Hence the oscillation of the free surface level in the vertical pipe during the air pocket rise was not captured. In addition, the pressure gradient change due to the overflow was not accounted in the numerical model. The magnitude of the initial pressure peak appears to be a direct result of the initial pressure differential between the hydrostatic pressure in the horizontal pipe and the pressurized air; considering the largest pressure peak is observed immediately after the introduction of the pressurized air to the standing water. The pressure oscillation amplitude subsided with time. Several flow parameters were found to influence the air release process including the diameter of the vertical pipe, the initial pressure of the air entrapped and initial water level in the vertical pipe.

Zhou et al. (2004a), as continuation of Zhou et al. (2002a), proposed a numerical model based on the rigid water column approach. The model was found to sufficiently predict observed pressure oscillation patterns and maximum observed pressure. Similarly, Zhou et al. (2011b) investigated the effect of the entrapped air pocket on flow transients during the rapid horizontal pipe filling. Contrary to the findings of Zhou et al. (2002a), a higher maximum pressure was observed with a larger initially entrapped air pocket. The discrepancy in the conclusions must be attributed to differences in the two studies. While the study of Zhou et al. (2002a) experienced air leakage through an orifice, the study of Zhou et al. (2011b) did not. The void content in the pipe, the relative initial amount of air compared to the initial amount of water available in a pipe system, tested in Zhou et al. (2011b) was significantly less than that of Zhou et al. (2002a).

Previously, there have been several efforts made to simulate transient air-water interaction within pipe networks using more sophisticated modeling methods than a simple one-dimensional approach. Among the few, Zhou et al. (2011a) simulated flow transients in a water filling pipe that contained an entrapped air pocket using a two-dimensional Volume of Fluids (VOF) method. The model was able to capture the movement of the air pocket and transient pressure oscillations. The numerical simulation performance suggested that the VOF interface tracking method is an applicable numerical model for simulating transient air-water interactions in pipe networks. Similarly, Shao and Yost (2013) investigated the air release process through a vertical pipe. A two-dimensional Navier-Stokes equation based, finite volume model was developed. The proposed model was capable of simulating the air-water interaction in a vertical pipe as well as the breaking of the free surface level due to the expansion and rise of the air. However, the interaction captured lasted only briefly because the initially available air to water ratio was near one causing the system to depressurize early on.

Additionally, the recent 3D-CFD simulations showed that it is possible to simulate the migration and release of entrapped air in pipe systems given the appropriate numerical models, initial conditions and boundary conditions (Choi et al., 2014, 2016). The detailed flow field data generated from the 3D-CFD simulations can be used to identify flow characteristics involved in sewer geysers. Chan et al. (2016) was also able to simulate pressure oscillations observed in an air pocket release experiment of Cong et al. (2017). However, the numerical simulation was insufficient to capture the pressure peak at the time of geyser overflow found in the physical experiment. *There is a lack of detailed 3D simulation of the violent geyser phenomena using techniques that can capture the two-phase interactions and dynamic nature of the pressure within the system. The present study attempts to fill this gap.*

Dimensional analysis

Numerical and experimental studies on multiphase flow in conduit systems variables are normalized using a dimensional analysis. The normalized variable will allow different geometries, large or small, to be compared to the same unit of measure and allow qualitative comparison of different simulations. The following dimensional analysis has adapted variables from the dimensional analysis of Leon (2018). Of many listed, two variables were selected to investigate their influence on the geyser formation, the current study does not include the complete analysis of the all variables listed. The relevance of the listed variables must be recognized, a complete study requires further experimental and numerical investigations in the future.

Observable manifestations of a violent geyser occurrence include, but are not limited to, maximum eruption height (h_g), maximum velocity in the vertical shaft (w_v), and total number of eruptions (m). For the purpose of the following discussion, ψ denotes

h_g, w_g or m. ψ is dominated by physical attributions of the system; length of the vertical pipe, L_v, length of the horizontal pipe, L_h, the diameter of the vertical pipe, D_v, the diameter of the horizontal pipe, D_h, volume of water in the vertical pipe, V_{water}, volume of air, V_{air}, velocity in the horizontal pipe, u_h and gravity, g (Figure 2.1). In addition, properties of fluids, density of water, ρ_{water}, density of air, ρ_{air}, dynamic viscosity of water, μ_{water}, dynamic viscosity of air, μ_{air} and surface tension between air and water, σ may influence ψ.

$$\psi = f\left(D_v, D_h, L_v, L_h, V_{water}, V_{air}, u_h, \rho_{water}, \rho_{air}, \mu_{water}, \mu_{air}, \sigma, g\right) \tag{2.1}$$

Non-dimensionalized number groups were formed using three chosen repeating variables (D_v, ρ_{water}, and g). The following combination of dimensionless number groups applies to any of the previously listed geyser properties symbolized as ψ (h_g, w_g, m).

$$\begin{aligned}\psi^* = \phi\Bigg(&\frac{D_h}{D_v}, \frac{L_v}{D_v}, \frac{L_h}{D_v}, \frac{V_{water}}{D_v^3}, \frac{V_{air}}{D_v^3}, \frac{u_h}{\sqrt{gD_v}}, \frac{\rho_{air}}{\rho_{water}}, \\ &\frac{\mu_{water}}{D_v\rho_{water}\sqrt{gD_v}}, \frac{\mu_{air}}{D_v\rho_{water}\sqrt{gD_v}}, \frac{\sigma}{\rho_{water}\sqrt{gD_v}^2 D_v}\Bigg)\end{aligned} \tag{2.2}$$

1. D_h/D_v is the diameter ratio between horizontal and vertical pipe.
2. L_v/D_v is the slenderness of the vertical pipe ($D_h = D_v$).
3. L_h/D_v is the slenderness of the horizontal pipe.
4. V_{water}/D_v^3 is the non-dimensionalized initial volume of water in the vertical pipe.
5. V_{air}/D_v^3 is the non-dimensionalized initial volume of air in the system.

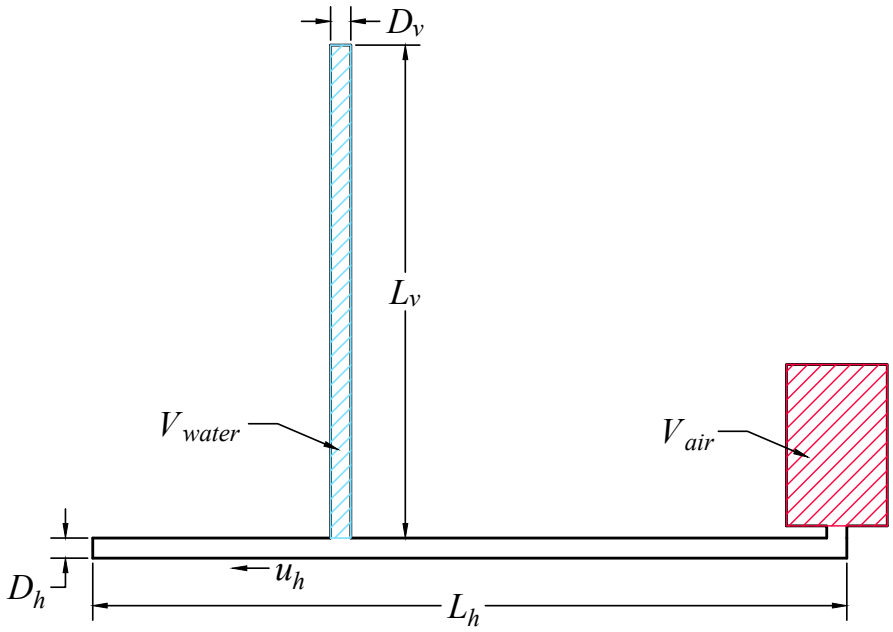

Figure 2.1: A simplified and generalized schematic of a geometry used to numerically study sewer geysers.

6. $u_h/\sqrt{gD_v}$ is the non-dimensionalized velocity in the horizontal pipe.

7. ρ_{air}/ρ_{water} is the density ratio between air and water.

8. $\mu_{water}/D_v\rho_{water}\sqrt{gD_v}$ is inverse of the Reynolds number (Re) when $\sqrt{gD_v}$ represents the characteristic velocity of the system.

9. $\mu_{air}/D_v\rho_{water}\sqrt{gD_v}$ is inverse of Re, when $\sqrt{gD_v}$ represents the characteristic velocity of the system.

10. $\sigma/\rho_{water}\sqrt{gD_v}^2D_v$ is inverse of the Weber number, We, when $\sqrt{gD_v}$ represents the characteristic velocity of the system.

Elayeb (2016) and Leon (2018) suggested that geyser eruption height is directly proportional to the air mass flowrate entering the vertical pipe for systems $D_h/D_v < 1/2$ due to so-called "bottleneck effect". The bottleneck effect is caused by a narrow vertical pipe congesting the air flow from the horizontal pipe. According to the study, the geyser eruption height was not influenced if $D_h/D_v > 1/2$ as the system became free of the bottleneck effect. While the overall effect of D_h/D_v on the geyser formation should not be neglected, the air-water interaction in the horizontal pipe must remain independent if the goal of the study is to numerically simulate air-water interactions in the horizontal pipe. Herein, D_h/D_v was fixed to one throughout the study.

The sixth dimensionless number represents the normalized velocity in the horizontal pipe by the characteristic velocity ($\sqrt{gD_v}$). In a similar manner as the pipe diameter ratio, D_h/D_v, the velocity in the horizontal pipe will influence the air-water interaction in the horizontal pipe by transporting or working against the air flow in the horizontal pipe. Herein, u_h was kept zero to isolate the transporting effect of the flow in the horizontal pipe to the air-water interaction.

All listed variables must be thoroughly studied to gain a complete mechanistic understanding of sewer geyser. However, such endeavor would be outside of the scope of the current work. The current work is limited to identifying and validating a complete 3D simulation method to capture sewer geysers and studying the influence of two chosen variables (L_v and V_{air}) on the violent geyser occurrence. The simulation method was validated by numerically reproducing physical experiments.

2.3 Identified knowledge gap

Based on the review of previous studies, the following list of knowledge gaps was identified.

- Only a few numerical models exist that attempted to simulate entrapped air release through vertical pipes (Vasconcelos and Wright, 2011; Shao and Yost, 2013). A fully three-dimensional multiphase flow simulations of sewer geysers is a less charted territory of computational fluid dynamics that only became an accessible option in the recent years due to its complexity and computationally expensive nature. Conducting high fidelity simulations of sewer geysers come with a number of challenges; the flow is inherently unsteady, three dimensional, and multiphase. One must apply appropriate numerical models in a refined three-dimensional space to capture such complex flow phenomena. For instance, the physical experiment of Elayeb (2016), which experimentally captured violent sewer geysers, used vertical shafts that ranged from 3 m to 12 m and 0.15 m in diameter. Each experimental run lasted up to 150 seconds. A numerical replication of such experiment with an acceptable resolution would require several million cells and thousands of time steps.

- While the presence of entrapped air in pipe systems are found to be influential to the pressure oscillation patterns and magnitude of the observed peak pressure, the release process of the entrapped air through the vertical pipes has not been sufficiently numerically simulated. Besides the pressure measurements at various locations in vertical and horizontal pipes, additional flow parameters, such as the rising speed of the releasing air and its internal pressure have not been numerically modeled previously. In addition, flow processes in the horizontal pipe while the system goes under a violent geyser eruption, such as slug formation in the horizontal pipe, have not been numerically studied in the context of violent geysers.

- The intensity of sewer geysers has not been systemically evaluated using appropriate numerical methods and dimensionless number groups. For example, the ratio between the initially available volume of water in the vertical pipe and air in the system must be investigated further.

2.4 Research questions

Numerical and experiment approaches were used to answer the following research questions;

1. Can a fully three-dimensional, multiphase, Reynolds Averaged Navier-Stokes equations based, turbulence model capture the main features of violent sewer geyser observed in experimental studies? What model parameters are necessary to obtain both qualitative and quantitative match?

2. How do the two parameters varied in the numerical studies, viz. volume of initially available water in the vertical shaft and air in the system, influence the occurrence

and characteristics of the sewer geyser?

Chapter 3 discusses the numerical simulation method used and its validation cases. Three physical experiments, two cases on spring-type geysers and one case on the violent geyser, were numerically reproduced. Processes and features captured in the numerical simulations were compared to what was observed in corresponding physical experiments. Overall, the numerical reproduction of the physical experiments was able to capture spring-type geyser eruptions with a close proximity. On the other hand, the numerical simulation was able to capture only global mean characteristics of the violent geyser. In Chapter 4, the previously validated numerical simulation approach was adopted and a numerical experiment was performed. In this numerical experiment, two system variables, the volume of initially available water and air in the system, were varied. Finally, chapter 5 summarizes the overall contributions of the study.

Chapter 3: Validation studies

The purpose of this chapter is to introduce and validate the 3D-CFD simulation method to be used. In the following sections, the simulation method is presented and validated by numerically reproducing three physical experiments. Pressure measurements made during the physical experiments were compared with the computed pressure resulting from the numerical simulations. The validated simulation method was used to study sewer geyser eruptions. In the following sections of this chapter, details of the simulation method and its validation results are presented. First, the governing equations and mesh construction details are discussed. Secondly, a description of the physical experiment to be numerically reproduced is provided. Finally, a comparison between the physical experiment and the numerical simulation is made.

3.1 Governing equations

A commercial finite volume computational fluid dynamics model which provided tools to construct mesh, establish simulation physics and solver algorithms (STARCCM+ V10 and 11). Further details on the numerical modeling method can be found in the user's manual (Star-CCM+ V10 User Guide, 2015) and the referenced studies. The flow was assumed to be governed by Reynolds-Averaged Navier-Stokes (RANS) model Launder

et al. (1975). The momentum equation is;

$$\begin{aligned}&\frac{\partial}{\partial t}\int_V \rho\mathbf{v}\,dV + \oint_A \rho\mathbf{v}\otimes(\mathbf{v}-\mathbf{v_g})\cdot d\mathbf{a}\\&= -\oint_A p\mathbf{I}\cdot d\mathbf{a} + \oint_A \mathbf{T}\cdot d\mathbf{a} + \int_V (\mathbf{f_r}+\mathbf{f}_g+\mathbf{f_p}+\mathbf{f_u}+\mathbf{f}_\omega+\mathbf{f}_L)\,dV\end{aligned} \tag{3.1}$$

where p is pressure, $\mathbf{I}$ is identity matrix, $\mathbf{T}$ is viscous stress tensor, $\mathbf{f_r}$ is body force due to rotation, $\mathbf{f_g}$ is body force due to gravity, $\mathbf{f_p}$ is porous media body force, $\mathbf{f_u}$ is user-defined body force, $\mathbf{f}_\omega$ is vorticity confinement specific force and $\mathbf{f_L}$ is Lorentz force or Laplace force. The continuity equation is;

$$\frac{\partial}{\partial t}\int_V \rho dV + \oint_A \rho(\mathbf{v}-\mathbf{v_g})\cdot d\mathbf{a} = \mathbf{0} \tag{3.2}$$

where ρ is density, $\mathbf{v}$ is velocity and $\mathbf{v_g}$ is grid velocity.

The simulated flow was turbulent. Hence the stress tensor, $\mathbf{T}$, is defined as the summation of laminar stress tensor, $\mathbf{T_l}$, and turbulent stress tensor, $\mathbf{T_t}$;

$$\mathbf{T} = \mathbf{T_l} + \mathbf{T_t} \tag{3.3}$$

where $\mathbf{T_l} = \mu_{eff}\left[\nabla\mathbf{v} + \nabla\mathbf{v}^\mathbf{T} - \frac{\mathbf{2}}{\mathbf{3}}(\nabla\cdot\mathbf{v})\mathbf{I}\right]$ and $\mu_{eff} = \mu + \mu_t$. Finite volume discretization was used for viscous flux and the governing equations. Energy transport equation is;

$$\begin{aligned}&\frac{\partial}{\partial t}\int_V \rho E dV + \oint_A [\rho H(\mathbf{v}-\mathbf{v}_g) + \mathbf{v}_g p]\cdot d\mathbf{a}\\&= -\oint_A \dot{\mathbf{q}}''\cdot d\mathbf{a} + \oint_A \mathbf{T}\cdot\mathbf{v}\,d\mathbf{a} + \int_V \mathbf{f}\cdot\mathbf{v}\,dV + \int_V s_u\,dV\end{aligned} \tag{3.4}$$

where E is total energy, H is the total enthalpy, $\dot{\mathbf{q}}''$ is the heat flux vector, $\mathbf{v}$ is the

velocity vector and $\mathbf{v_g}$ is the grid velocity factor. $\mathbf{f}$ is the body force vector representing the combined body forces of rotation($\mathbf{f_r}$) and gravity ($\mathbf{f_g}$). Total energy, E, is related to the total enthalpy, H, by;

$$E = H - p/\rho \tag{3.5}$$

$$H = h + |\mathbf{v}|^2/2 \tag{3.6}$$

where h is enthalpy and $h = C_pT$. The equation of state for air is;

$$P_{abs} = \rho RT \tag{3.7}$$

where P_{abs} is absolute pressure, R is the specific gas constant of air and T is temperature of air.

The density-pressure relation was used when compressibility of water was accounted (Equation 3.8). By doing so, if triggered, compressibility of both air and water were modeled.

$$\rho_{water} = \rho_0 + \frac{P}{c^2} \tag{3.8}$$

where ρ_0 is reference density (1000 m^3/s), ρ_{water} is density of water, c is speed of sound (a function of pipe material) and P is pressure.

3.1.1 Turbulence closure model

Realizable two-layer $k-\varepsilon$ turbulence closure model was used. Other commonly used eddy viscosity models, $k-\omega$ (Wilcox, 1988) or Spalar-Allmaras (Spalart and Allmaras, 1992), were also considered. However, Spalart-Allmaras model is known to be not suitable for

flows involving body forces, such as buoyancy. In addition, $k-\omega$ models are better suited for boundary layer prolems and low Reynolds number flows (Wilcox, 1991; Spalart, 2000; Star-CCM+ V10 User Guide, 2015). Despite its known limitations, $k-\varepsilon$ was chosen due to its robustness within the chosen program (StarCCM+v10 and v11).

The model combines the realizable $k-\varepsilon$ turbulence model as formulated by Shih et al. (1994) with the two-layer approach formulation suggested by Rodi (1991). Transport equation of k is;

$$\begin{aligned}&\frac{d}{dt}\int_V \rho k dV + \int_A \rho k\left(\mathbf{v}-\mathbf{v}_g\right)\cdot d\mathbf{a} \\ &= \int_A \left(\mu + \frac{\mu_t}{\sigma_k}\right)\nabla k \cdot d\mathbf{a} + \int_V \left[f_c G_k + G_b - \rho\left((\varepsilon-\varepsilon_0) + \Upsilon_M + S_k\right)\right] dV\end{aligned} \tag{3.9}$$

Transport equation of ε is;

$$\begin{aligned}&\frac{d}{dt}\int_V \rho\varepsilon dV + \int_A \rho\varepsilon\left(\mathbf{v}-\mathbf{v}_g\right)\cdot d\mathbf{a} \\ &= \int_A \left(\mu + \frac{\mu_t}{\sigma_\varepsilon}\right)\nabla\varepsilon \cdot d\mathbf{a} \\ &+ \int_V \left[f_c C_{\varepsilon_1} S\varepsilon + \frac{\varepsilon}{k}\left(C_{\varepsilon_1} C_{\varepsilon_3} G_b\right) - \frac{\varepsilon}{k+\sqrt{\nu\varepsilon}} C_{\varepsilon_2}\rho\left(\varepsilon-\varepsilon_0\right) + S_\varepsilon\right] dV\end{aligned} \tag{3.10}$$

where S_k and S_ε are user-specified source terms, which was not specified in the following simulations; ε_0 is the ambient turbulence value in the source terms that counteracts turbulence decay, which was not activated in the following simulations; curvature correction factor, f_c, was not applied in the following simulations; and ν is kinematic viscosity. The turbulent production, G_k, is;

$$G_k = \mu_t S^2 - \frac{2}{3}\rho k\nabla\cdot\mathbf{v} - \frac{\mathbf{2}}{\mathbf{3}}\mu_{\mathbf{t}}\left(\nabla\cdot\mathbf{v}\right)^{\mathbf{2}} \tag{3.11}$$

where $\bigtriangledown \cdot \mathbf{v}$ is the velocity divergence and S is the modulus of the mean strain rate tensor defined as the following;

$$S = |\mathbf{S}| = \sqrt{2S : S^T} = \sqrt{2S : S} \tag{3.12}$$

where $\mathbf{S}$ is the strain rate tensor and defined as the following;

$$\mathbf{S} = \frac{\mathbf{1}}{\mathbf{2}} \left(\nabla \mathbf{v} + \nabla \mathbf{v}^{\mathbf{T}} \right) \tag{3.13}$$

The buoyancy production, G_b, is defined as;

$$G_b = \beta \frac{\mu_t}{\sigma_t} \left(\nabla T \cdot \mathrm{g} \right) \tag{3.14}$$

where β is the coefficient of thermal expansion, g is the gravitational vector, ∇T is the temperature gradient vector, and σ_t is the turbulent Prandtl number. For ideal gases, the following relation is used to estimate, coefficient of thermal expansion, β;

$$\beta = -\frac{1}{\rho} \frac{\partial \rho}{\partial T} \tag{3.15}$$

The dilatation dissipation, Υ_M, is;

$$\Upsilon_M = \frac{C_M k \varepsilon}{c^2} \tag{3.16}$$

where c is the speed of sound and C_M is 2 (Sarkar and Lakshmanan, 1991). The turbulent viscosity, μ_t, is;

$$\mu_t = \rho C_\mu \frac{k^2}{\varepsilon} \tag{3.17}$$

C_μ is defined as a function of mean flow and turbulent properties;

$$C_\mu = \frac{1}{A_0 + A_s U^{(*)} \frac{k}{\varepsilon}} \tag{3.18}$$

where the coefficient $U^{(*)}$ is defined as;

$$U^{(*)} = \sqrt{\mathbf{S} : \mathbf{S} - \mathbf{W} : \mathbf{W}} \tag{3.19}$$

where rotation rate tensor, $\mathbf{W}$, is;

$$\mathbf{W} = \frac{\mathbf{1}}{\mathbf{2}} \left(\nabla \mathbf{v} - \nabla \mathbf{v}^{\mathbf{T}} \right) \tag{3.20}$$

Further coefficients included;

$$A_s = \sqrt{6} cos\phi \tag{3.21}$$

$$\phi = \frac{1}{3} acos \left(\sqrt{6}\, W \right) \tag{3.22}$$

$$W = \frac{S_{ij} S_{jk} S_{ki}}{\sqrt{S_{ij} S_{ij}}^3} \tag{3.23}$$

$$C_{\varepsilon 1} = max \left(0.43, \frac{\eta}{5\eta} \right) \tag{3.24}$$

$$\eta = \frac{Sk}{\varepsilon} \tag{3.25}$$

Default model constants were used; $A_0 = 4.0$, $C_{\epsilon 2} = 1.9$, $\sigma_k = 1.0$ and $\sigma_\varepsilon = 1.2$.

3.1.2 Wall treatment

The two-layer All y^+ Wall Treatment was used. The reference velocity, u^* is specified using the wall law;

$$u^* = \sqrt{g\nu u/y + (1-g)\, C_\mu^{1/2} k} \tag{3.26}$$

where the blending function, g, is defined in terms of the wall-distance Reynolds number, Re_y;

$$g = exp\left(-\frac{Re_y}{11}\right) \tag{3.27}$$

where $Re_y = \sqrt{k}y/\nu$. The wall-cell production, G_k, is;

$$G_k = g\mu_t S^2 + (1-g)\,\frac{1}{\mu}\left(\rho u^* \frac{u}{u^+}\right)^2 \frac{\partial u^+}{\partial y^+} \tag{3.28}$$

Finally the wall-cell dissipation, ε, is;

$$\varepsilon = \frac{k^{3/2}}{l_\varepsilon} \tag{3.29}$$

$\mu_t|_{k-\varepsilon}$, which was previously defined (Equation 3.17), is blended with the two-layer approach at wall cells (Jongen, 1998);

$$\mu_t = \gamma \mu_t|_{k-\varepsilon} + (1-\gamma)\,\mu \left(\frac{\mu_t}{\mu}_{2layer}\right) \tag{3.30}$$

The wall-proximity indicator γ is;

$$\gamma = \frac{1}{2}\left[1 + tanh\left(\frac{Re_y - Re_y^*}{A}\right)\right] \tag{3.31}$$

where Re_y^* is the limit of applicability of the two-layer formulation and Re_y^* of 60 was

used. The constant "A" determines the width of the wall-proximity indicator and defined as;

$$A = \frac{|\Delta Re_y|}{atanh0.98} \tag{3.32}$$

ΔRe_y of 10 was used. The length scale function, l_ε, is (Wolfshtein, 1969);

$$l_\varepsilon = c_l y \left[1 - exp\left(-\frac{Re_y}{A_\varepsilon}\right)\right] \tag{3.33}$$

where $A_\varepsilon = 2c_l$, $c_l = \kappa C_\mu^{-3/4}$, $C_\mu = 0.09$ and $\kappa = 0.42$. The turbulent viscosity ratio function is;

$$\frac{\mu_t}{\mu} = Re_y C_\mu^{1/4} \kappa \left[1 - exp\left(-\frac{Re_y}{A_\mu}\right)\right] \tag{3.34}$$

where $A_\mu = 70$.

The viscous sublayer and the logarithmic regions were approximately blended at the buffer layer (Reichardt, 1951);

$$u^+ = \frac{1}{\kappa} ln\left(1 + \kappa y^+\right) + C\left[1 - exp\left(\frac{y^+}{D}\right) - \frac{y^+}{D} exp\left(-by^+\right)\right] \tag{3.35}$$

where

$$D = y_m^+ \tag{3.36}$$

$$C = \frac{1}{\kappa} ln\left(\frac{E'}{\kappa}\right) \tag{3.37}$$

$$b = \frac{1}{2}\left(\frac{D_\kappa}{C} + \frac{1}{D}\right) \tag{3.38}$$

y_m^+ is the intersection of the viscous and fully turbulent regions.

The formulation of Kader (1981) was used for the temperature at walls. The formulation was modified to account for the effects of wall roughness;

$$t^+ = exp\left(-\Gamma\right)\left(t^+_{lam} + q^+_{lam}\right) + exp\left(-\frac{1}{\Gamma}\right)\left(t^+_{trb} - q^+_{trb}\right) \tag{3.39}$$

where t^+ is dimensionless temperature, Γ is blending function;

$$\Gamma = \frac{0.01c\left(\sigma y^+\right)^4}{1 + \frac{5}{c}\sigma^3 y^+} \tag{3.40}$$

and

$$c = e^{\left(\frac{1}{f}-1\right)} \tag{3.41}$$

f is the roughness function defined as (Cebeci and Bradshaw, 1977);

$$f = \begin{cases} 1 & R^+ \leq R^+_{smooth} \\ \left[B\left(\frac{R^+ - R^+_{smooth}}{R^+_{rough} - R^+_{smooth}}\right) + CR^+\right]^a & R^+_{smooth} < R^+ < R^+_{rough} \\ B + CR^+ & R^+ > R^+_{rough} \end{cases} \tag{3.42}$$

where

$$a = sin\left[\frac{\pi}{2}\frac{log\left(R^+/R^+_{smooth}\right)}{R^+_{rough}/R^+_{smooth}}\right] \tag{3.43}$$

and coefficients used are; $B = 0$, $C = 0.253$, $R^+_{smooth} = 2.25$, and $R^+_{rough} = 90$ (Cebeci and Bradshaw, 1977). The roughness parameter, R^+ is;

$$R^+ = \frac{ru^*}{\nu} \tag{3.44}$$

where r is the equivalent sand-grain roughness defined in the simulation.

For non-slip walls, the wall roughness was assigned by specifying the equivalent sand-grain roughness height (r). Plastic pipes were used in the physical experiments. r was assumed to be zero. Additional simulations were conducted to test the sensitivity of the simulation result as a function of r (0 or 1.5×10^{-6} m). As long as the pipe walls were considered to be non-slip walls to account for the viscous effect at the wall, the pressure measurement and overflow height were found to be not effected by r. On the other hand, when the pipe walls were assumed to be slip walls, the computed pressure over predicted the measured pressure.

Three different boundaries, slip walls around the overflow region, non-slip walls for the pipe and pressure outlet at the top surface of the overflow region, were commonly used throughout the investigation. For slip walls and non-slip walls, a Neumann boundary conditions were used for the turbulent kinetic energy ($\partial k/\partial n|_w = 0$). At the pressure outlet boundary, the turbulent kinetic energy and turbulent dissipation rate were specified using the turbulence intensity (I) and turbulence viscosity ratio μ_t/μ;

$$k \approx \frac{3}{2}\left(Iv\right)^2\right) \tag{3.45}$$

$$\varepsilon \approx \frac{\rho C_\mu k^2}{\left(\mu_t/\mu\right)\mu} \tag{3.46}$$

where v is the turbulent velocity scale.

The face value of velocity was computed by extrapolating the parallel component of velocity in the adjacent cell using the reconstruction gradients for slip walls. The Hybrid Gauss-Least Squares Method was used for reconstruction gradients (Star-CCM+ V10 User Guide, 2015). The Venkatakrishnan limiter was used as the reconstruction gradient limiting method (Venkatakrishnan, 1995). The tangential velocity was explicitly set to

zero for non-slip walls. Boundary face pressure was extrapolated from the adjacent cell using the reconstruction gradients for all types of walls. The walls were considered to be adiabatic, meaning no heat transfer was present through the walls.

The boundary face velocity was extrapolate from the interior using the reconstruction gradients at pressure outlet. Only the boundary normal component of the velocity was used as the inflow for the solution stability. The boundary pressure, p_f, was specified at atmospheric pressure. No target mass flow rate was assigned. If inflow were to occur, the boundary pressure, p_f, was;

$$p_f = p_{specified} - \frac{1}{2}\rho_f |V_n|^2 \tag{3.47}$$

3.1.3 Multiphase interface tracking model

The air-water interface was simulated using the volume of fluid (VOF) model (Muzaferija and Peric, 1999). The model tracks proportion of the fluids in a given cell and the two fluids are assumed to share velocity, pressure and temperature (Equations 3.48 through 3.51). The model uses the Eulerian specification approach to the flow field.

$$\rho = \sum_i \rho_i \alpha_i \tag{3.48}$$

$$\mu = \sum_i \mu_i \alpha_i \tag{3.49}$$

$$c_p = \sum_i \frac{(c_p)_i \rho_i}{\rho} \alpha_i \tag{3.50}$$

$$\alpha_i = \frac{V_i}{V} \tag{3.51}$$

The transport of the volume fractions, α_i, was;

$$\frac{d}{dt}\int_v \alpha_i dV + \int_s \alpha_i \left(v - v_g\right) dA = \int_V \left(s_{\alpha_i} - \frac{\alpha_i}{\rho_i}\frac{D\rho_i}{Dt}\right) dV \tag{3.52}$$

The High-Resolution Interface Capturing convection discretization scheme was used to solve the convection equation (Muzaferija and Peric, 1999). Sharpening factor, C_α, was not applied to the simulation. Angle factor, C_Θ, in the second order convection discretization scheme was set to 0.05. The lower Courant number limit was 0.5 and the upper limit was 1.

Surface tension effect could influence the contact angle between water and pipe walls and air-water interface formation. The surface tension force was calculated according to the continuum surface force model (Brackbill et al., 1992). A constant surface tension quantity for the primary phase, water, was assigned (σ = 0.074 N/m). If regarded, the surface tension force, f_σ, was assumed to be a force normal to the interface. The curvature of the interface, K, was expressed;

$$K = - \bigtriangledown \cdot \frac{\bigtriangledown \alpha_i}{|\bigtriangledown \alpha_i|} \tag{3.53}$$

Then f_σ can be expressed as;

$$f_\sigma = \sigma \bigtriangledown \cdot \left(\frac{\bigtriangledown \alpha_i}{|\bigtriangledown \alpha_i|}\right) \bigtriangledown \alpha_i \tag{3.54}$$

A sensitivity analysis was carried out for spring-type geysers in Chapter 4 and was found

to be non-influential.

3.1.4 Solver algorithm and iteration scheme

Governing equations of the numerical model was solved through the segregated approach (i.e. uncoupled approach). The momentum equations were linked with the continuity equation with the predictor-corrector approach (Bird, 2002; Ferziger and Peric, 2012; Perić et al., 1988). First order temporal discretization scheme was used. The Hybrid Gauss-Least Square gradient method was used to solve the pressure-velocity coupling. A co-located variable arrangement and a Rhie-and-Chow-type pressure-velocity coupling combined with a SIMPLE-type algorithm was used (Ferziger and Peric, 2012).

Implicit iteration was used with an under-relaxation factor of 0.8 to solve the two turbulence model equations. Using the under-relaxation method each time step carried out its inner iteration and was found to result in a stable solution;

$$\frac{a_p}{\omega}\phi_P^{k+1} + \sum_n a_n \phi_n^{k+1} = b + \frac{a_p}{\omega}\left(1-\omega\right)\phi_P^k \tag{3.55}$$

where the summation is over all the neighbors of n of cell P. b represents the explicit contributions resulting from the iteration k to the discretized equation. The coefficients a_P and a_n were obtained directly from the discretized terms. $k+1$ implies the value after the solution was produced. The segregated solver was used for velocity, pressure, energy and the VOF transport equations. The algebraic multigrid (AMG) solver linear solver with the Gauss-Seidel relaxation scheme was used. Under relaxation factor for velocity, pressure, energy and VOF transport equations were 0.8, 0.2, 0.9 and 0.9. The $k-\varepsilon$ turbulence model equations were solved using the AMC linear solver with Gauss-Seidel

under relaxation factor of 0.8.

Physical experiments presented in Vasconcelos and Wright (2011), Appendix A, and Elayeb (2016) were numerically reproduced using the presented 3D-CFD simulation method. The selected experiments portray spring-type geysers and violent geysers.

3.2 Spring-type air-water eruptions - case I

The physical experimental geometry of Vasconcelos and Wright (2011) was consisted of a vertical pipe and a horizontal pipe (Figure 3.1). A volume of pressurized air was stored at an end section of the horizontal pipe. This air was separated by a butterfly valve from the stagnant water filling the rest of the system. There was no flow in the horizontal pipe. The valve opened and released the entrapped air at the beginning of the experiment. The vertical pipe acted as a release path for the air pocket. Pressure was measured at a location along the horizontal pipe during the air release process.

The computational domain of the numerical simulation was identical to the physical experiment except for the extended region beyond the vertical pipe outlet (Figure 3.1). The extended region was added to simulate the atmosphere. The stagnant water and pressurized air were initially assigned to their appropriate regions. The butterfly valve that separated air and water in the experiment was assumed to open instantaneously at the beginning of the simulation. Polyhedral mesh was used to span the computational domain (Figure 3.2). The mesh size was enlarged in the extended region to achieve computational efficiency.

The numerical simulation captured expansion, migration and rise of the entrapped air pocket. The amplitude of the computed pressure oscillation decreased with time until the air pocket reached to the bottom of the vertical pipe. The end section of

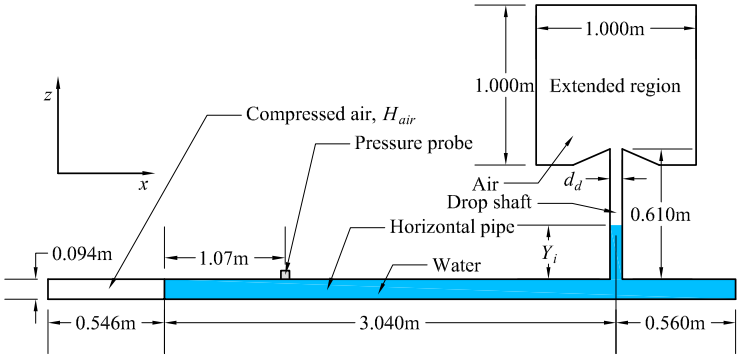

Figure 3.1: The computational geometry included a horizontal pipe and a vertical pipe just as the physical experiment of Vasconcelos and Wright (2011). The extended region was added in the numerical simulation to simulate the atmosphere.

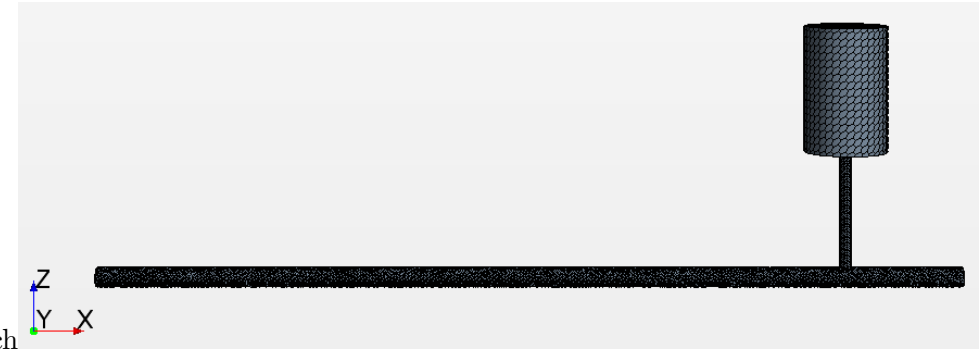

chch

Figure 3.2: Computational domain mesh. Mesh size was coarsened around the extended region.

the horizontal pipe, where the pressurized air was initially stored, becomes occupied by the redistributed water. This leaves the system open to the atmospheric pressure and depressurized (Figures 3.3 and 3.4).

3.2.1 Result

In the physical experiment, a number of initial conditions were performed while varying three independent variables; drop shaft diameter (d_d), the initial air pressure head (H_{air}) and initial water level in drop shaft (Y_i). One representative physical experiment that exhibited most dynamic pressure oscillation in the horizontal pipe was selected and numerically reproduced. The computed pressure at a location in the horizontal pipe was recorded and compared with the experimental data. The location of the data collection is specified as "Pressure probe" in Figure 3.1. The initial conditions of the selected simulation are d_d=0.0576 m, H_{air}=0.305 m and Y_i = 0.254 m.

The pressure measured in the horizontal pipe reflected the air release process. Initially, pressure in the horizontal pipe equaled the hydrostatic pressure resulted by the water level in the the drop shaft (Y_i = 0.254 m). Once the simulation is triggered, the butterfly valve separating air and water was assumed to open instantaneously. Onset of the valve opening, the measured pressure increased as the water level in the vertical shaft increased instantaneously. This increase in the internal pressure was due to the impact of the pressurized air impinging on stagnant water filling the system. This perturbation persisted through the air pocket expansion. The air accumulated along the crown of the horizontal pipe and advanced its front towards the vertical pipe. Once the font of the air pocket arrived at the neck of the vertical pipe, the pressure in the horizontal pipe began to descend as the air pocket made its way up the vertical pipe. There was no

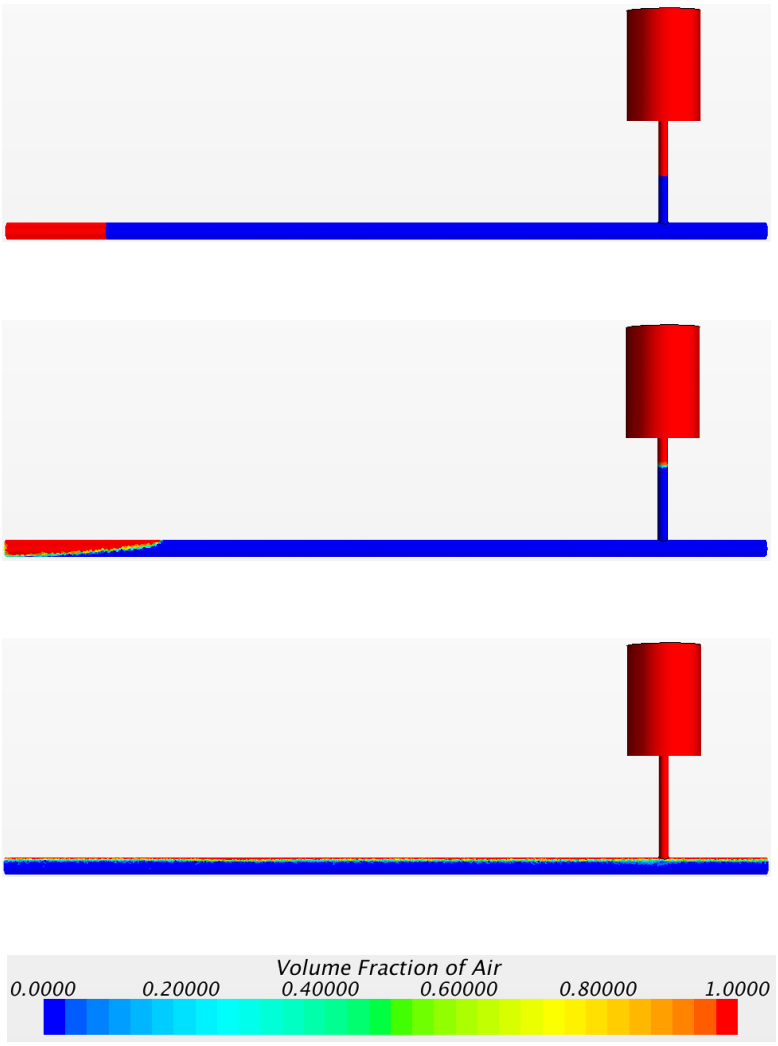

Figure 3.3: Void fraction plot of the numerical simulation at; (a) t=0 s, (b) t=0.5 s, (c) t=5 s. Over time, the entrapped air expanded towards the vertical pipe.

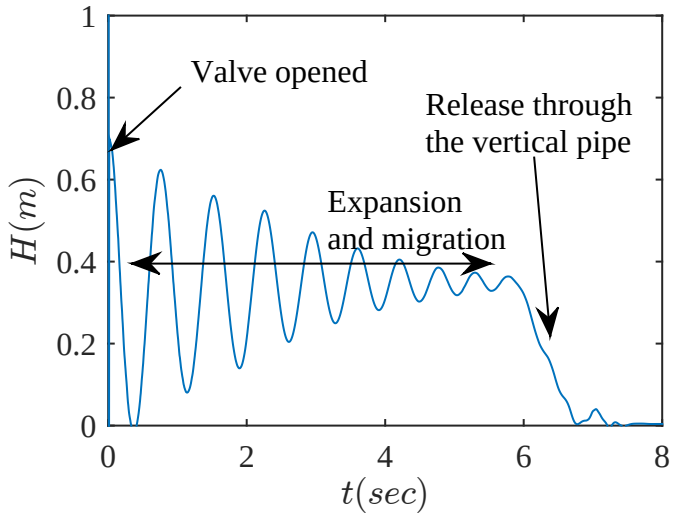

Figure 3.4: Air expansion, migration and release process are noted for a spring-type air-water eruption flow.

overflow in the presented case, however, the free surface level rose with the ascending air pocket. Simultaneously, during this rise, there was a volumetric exchange between the rising air and water in the vertical pipe. A partial volume of the suspended water column fell around the periphery of the ascending air pocket, creating a thin layer of downward flow. While some air-water interactions were captured in the numerical simulation, the pressure profile of spring-type air-water eruption flow greatly differs from a violent geyser (Section 3.4).

The computed and measured pressure in the horizontal pipe were compared (Figure 3.5). Two simulations were conducted according to two possible polytropic assumptions; isothermal and adiabatic process of ideal air. The frequency progression and amplitude decay trend varied between the two polytropic process assumptions (Figures 3.6 and 3.7). Pierrus and De Lange (1997) stated that "for isothermal oscillations of a perfect

gas ... the period of oscillation is a factor $\sqrt{\gamma}$ greater than that of adiabatic process." This results in 18% increase in the oscillation period. The numerical simulations yielded a similar trend (Figures 3.6 and 3.7). Comparing the first six oscillations of the two numerical simulation results, the iso thermal process on averaged had 3% longer oscillation period. The oscillation period difference between two processes was significantly less than what was predicted in the study of Pierrus and De Lange (1997). However, it must be noted that the present simulation involves air and water whereas the referenced study only involved air.

The difference in the amplitude decay can be explained by the polytropic process relation (Equation 3.56). When expanding, the predominant behavior of the air pocket in the experiment, the volume ratio between two time steps ($t = i$ and $i + 1$), V_i/V_{i+1} is less than 1. Given the same initial conditions (P_i,V_i), the isothermal process assumes r of 1 and adiabatic process of a diatomic gas, air, assumes r of 1.4. This difference in the exponent results in smaller P_{i+1} under the adiabatic condition assumption (Equation 3.57). When compared with the physical experiment, adiabatic assumption matched better than the isothermal assumption.

$$P_{i+1} = \left(\frac{V_i}{V_{i+1}}\right)^r P_i \tag{3.56}$$

$$P_i > P_{i+1,isothermal} > P_{i+1,adiabatic} \tag{3.57}$$

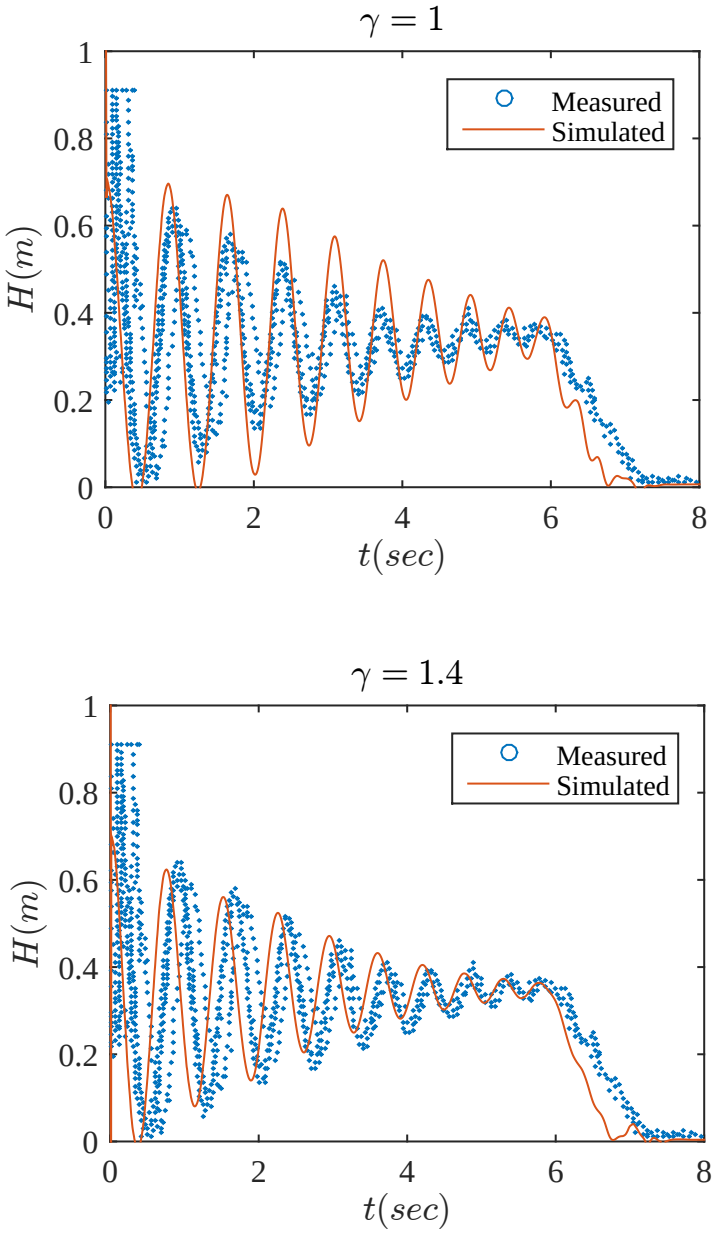

Figure 3.5: Simulated and measured pressure in the horizontal pipe. The measured pressure shows three repetitions carried out during the physical experiment.

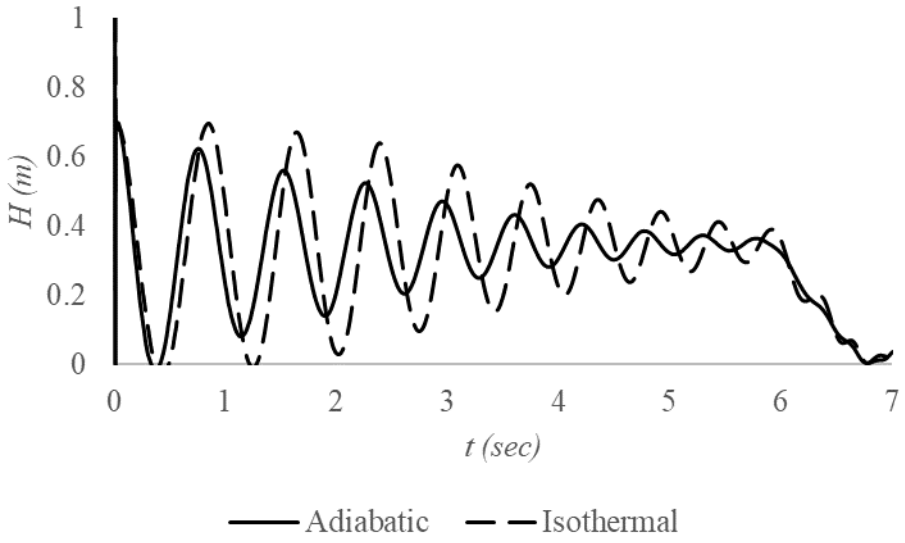

Figure 3.6: Computed pressure traces for adiabatic and isothermal processes are shown.

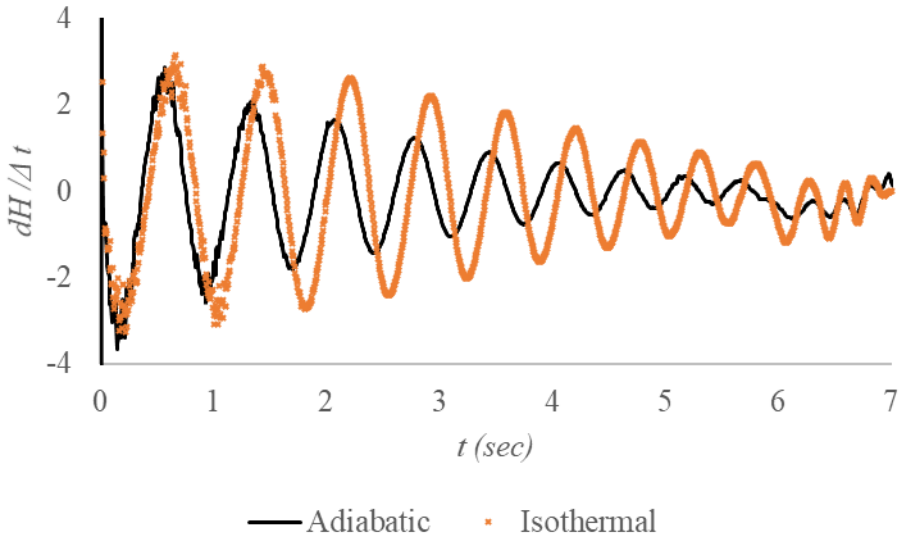

Figure 3.7: Computed rate of change of pressure ($dH/\delta t$) traces for adiabatic and isothermal processes are shown. Central differencing was used.

Table 3.1: Details of the meshes used for the grid convergence study are shown.

	Mesh	Characteristic mesh size (h)	Total cell number
Grid 1	Fine	0.0099 m	60668
Grid 2	Medium	0.0128 m	30991
Grid 3	Coarse	0.0167 m	14342

3.2.2 Grid convergence

The grid convergence of the presented numerical simulations were examined. In the following grid convergence study, the previously presented simulation was carried out three times, while assuming that air goes through an adiabatic process, using three different mesh sizes: fine, medium and coarse (Table 3.1). The computed pressure in the horizontal pipe were compared between the three grid sizes. The grid convergence index (GCI) was computed (Roache, 1997). The global order of accuracy (P) was 6.72 and oscillatory convergence occurred at 10.31 % of the simulation time. The averaged apparent order of accuracy was used to assess the GCI for individual time steps (Figure 3.8). The maximum discretization uncertainty was 0.18 m. This maximum value occurred at the first time step (t = 0.0015 sec). The remaining simulation time resulted in a discretization uncertainty 0.05 m or less.

3.3 Spring-type air-water eruptions - case II

A physical experiment concerning spring-type geyser was numerically simulated using the previously presented simulation method. The computed pressure at various locations computational geometry and air-water interface evolution in the vertical pipe were

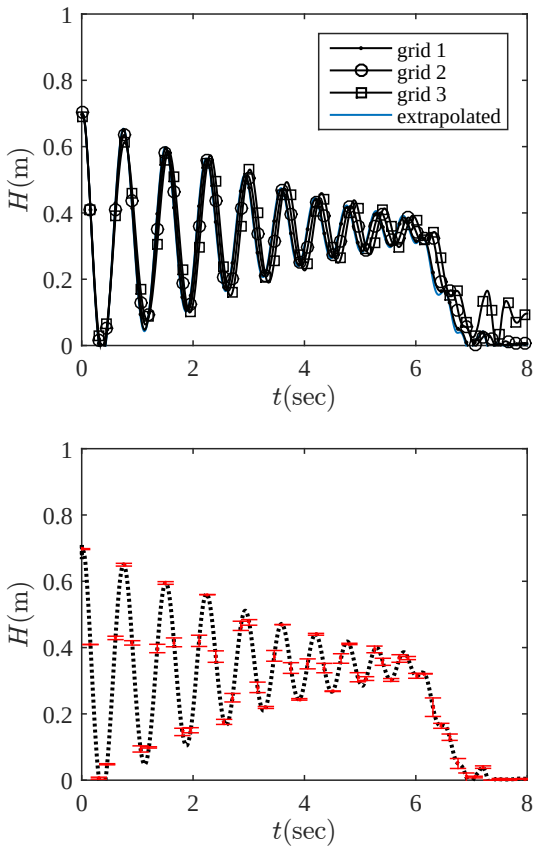

Figure 3.8: Grid convergence result; (a) computed pressure from the three different grid sizes and (b) computed and extrapolated pressure with discretization error bars.

compared to the physical experiment measurements.

The experiment was conducted at the river hydraulics research facility located at Oregon State University, Corvallis, OR. The experimental facility consisted of a vertical and a horizontal pipe. The upstream and downstream of the horizontal pipe were connected to constant pressure tanks to create a constant flow in the horizontal pipe. The available upstream head was 3.65 m and the downstream head was 2.2 m. A finite volume of pressurized air was introduced at a location upstream of the vertical pipe at the beginning of each trial. The entrapped air pocket expanded and advanced towards the downstream with the flow in the horizontal pipe. Once it arrived at the bottom of the vertical pipe, it rose through the existing water column in the vertical pipe while creating vigorous mixing of air and water at its tale end. The flow rate in the horizontal pipe and the initial pressure of the introduced air were varied. Some initial conditions created more dynamic overflows than others. Further detail on the physical experiment including the experiment matrix and the experiment procedure are provided in Appendix A.

Pressure measurements were made at five locations throughout the experimental facility (Figure 3.9). The experiments were conducted under three flow rates and three initial air pressures. Five repetitions were made for each of the experiment. Forty-five trials were conducted in total. High speed images of one initial condition combination were collected. The high speed images were used to study the advancement and release of air in the vertical pipe. A single field view of the high speed camera was not sufficient to capture the entire length of the vertical pipe, hence the examination window was divided into four sections (Figure 3.10). Each section was repeated three times to insure the repeatability of the experiment.

The experiment facility was equipped with a recirculating system with constant head

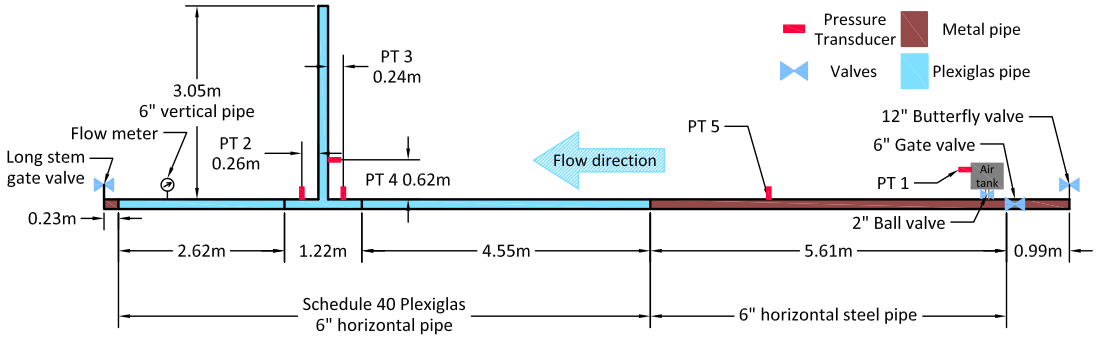

Figure 3.9: A schematic of the pipe system used in the experiment. Constant pressures are maintained at upstream and downstream of the horizontal pipe.

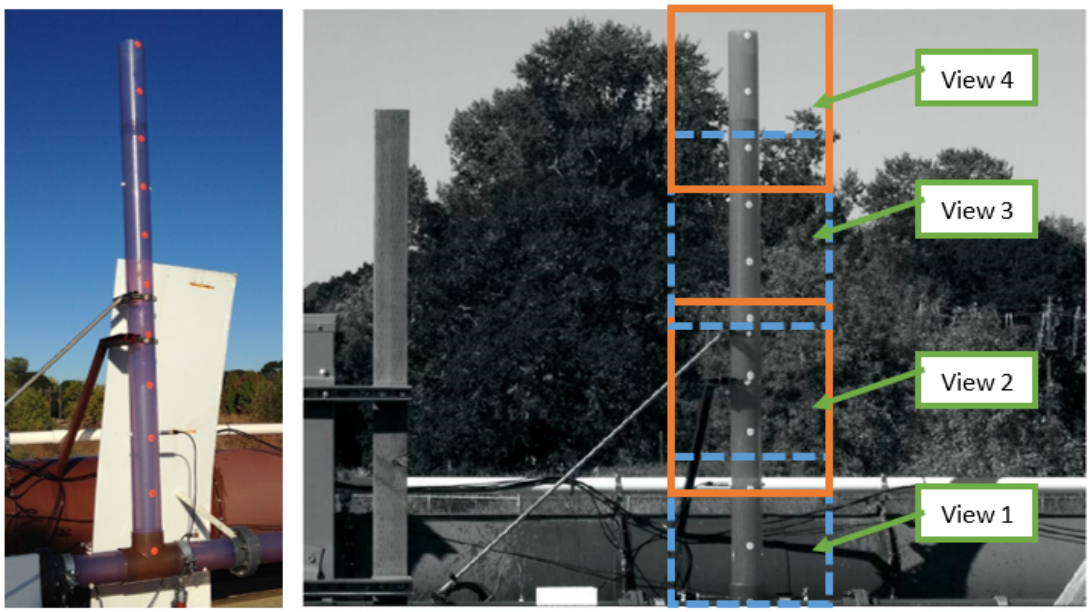

Figure 3.10: Break down of field view segments are shown. From the bottom to the top of the vertical pipe, it was divided into four field view segments.

maintained at the upstream and the downstream of the horizontal pipe. A part of the horizontal pipe was made of six inch galvanized steel and rest of the system was made of six inch schedule 40 Plexiglas pipes (Figure 3.9). Five pressure transducers (PT) with a measurement range of 1.5 to 1000 psia and an accuracy of ±0.04% of full scale were installed throughout the pipe system (Figure 3.9). PT 1 measured pressure in the air tank. PT 3 and PT 2 measured pressure immediately upstream and downstream of the vertical pipe. PT 4 measured the pressure in the vertical pipe. Lastly, PT 5 measured pressure in the metal section of the horizontal pipe. A flow meter was installed downstream of the vertical pipe. The flow in the horizontal pipe was measured using an ultrasonic flow meter with an accuracy ±1% of reading or ±0.01 ft/sec (larger).

The computational geometry of the numerical simulation was identical to the physical experiment (Figure 3.11). The pressure outlet boundary maintained constant atmospheric pressure at the top surfaces of the extended region, upstream head tank and downstream head tank. The side walls of the two head tanks and the outlet region were slip walls and the pipe walls were non-slip walls (Figure 3.12). In the physical experiment, the long stem gate valve regulated the flow rate in the horizontal pipe and the 6 inch gate valve was installed to prevent the pressurized air from escaping the pipe system. The numerical simulation became unstable when the gate valves were incorporated into the computational geometry. Instead, to achieve simulation stability, upstream head (H_{up}) and down stream head (H_{down}) were adjusted to produce desired flow rate. The amount of air escaped towards the head tank was minimal.

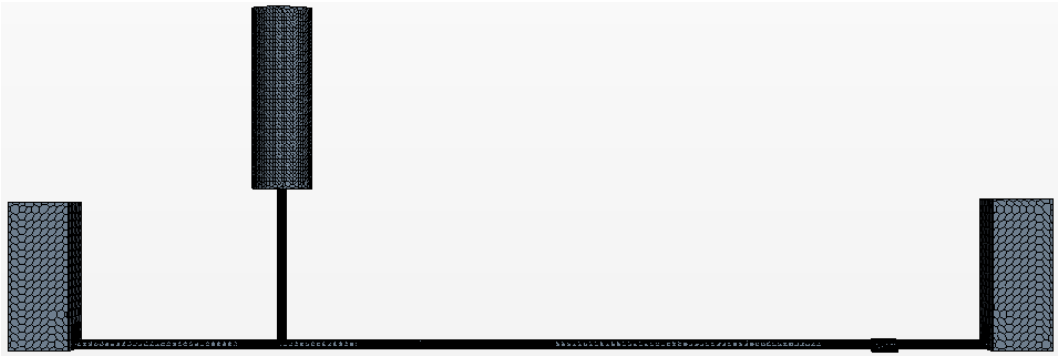

Figure 3.11: Computational domain of the numerical simulation consisted of a vertical pipe and horizontal pipe. The horizontal pipe was connected to an upstream tank and a downstream tank that maintained constant head.

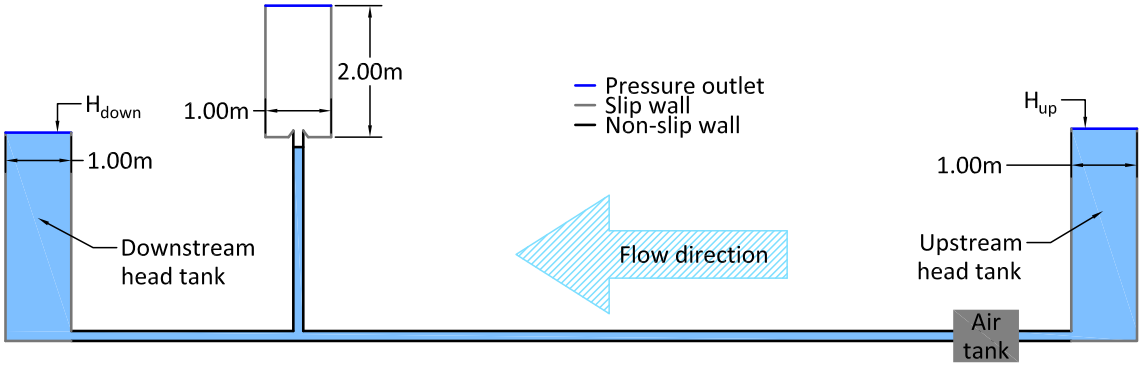

Figure 3.12: Boundary conditions used in the computational domain. The pipe walls were rough walls. The side walls of the upstream head tank, downstream head tank, and overflow region were slip walls. The top surfaces of the upstream head tank, downstream head tank and the overflow region were pressure outlet walls that maintained constant atmospheric pressure.

3.3.1 Result

The physical experiment measurements and computed values are compared for the present spring-type geyser case II. Three distinctive physical interactions were reflected in both measured and computed pressure; (i) a rapid pressure drop in the air tank immediately after the valve opening, (ii) a constant pressure at all locations during the air expansion and migration, and (iii) a brief variation in pressure during the air release through the vertical pipe (Figure A.5). Of the conducted physical simulations, one representative initial condition combination was selected and numerically simulated; $Q =$ 180 gpm and $P_{air} = 60$ psia. This initial condition combination was also used for the high speed image analysis in the physical experiment. The computed pressure of the numerical simulation was compared with the measured pressure of the physical experiment. H_{up} of 2.5 m and H_{down} of 2.45 m measured from the horizontal pipe invert created the correct pressure differential between the upstream head tank and the downstream head tank to produce $Q = 180$ gpm. The initial water level in the drop shaft was 2.47 m, measured from the horizontal pipe invert. This was consistent with the physical experiment.

The five pressure transducer locations were identified in the computational domain and the simulated pressure at these locations were compared with the measured pressure (Figures 3.13, 3.14 and 3.15). While the rapid pressure drop in the air tank was well captured in the numerical simulation, the pressure rise immediately after the valve opening at PT3, PT4 and PT5 were over estimated. The variation in the measured pressure during the entrapped air release through the vertical pipe was captured, through the occurrence was earlier and the magnitude was smaller than the physical experiment.

The air-water interface during the air release process was tracked using the image

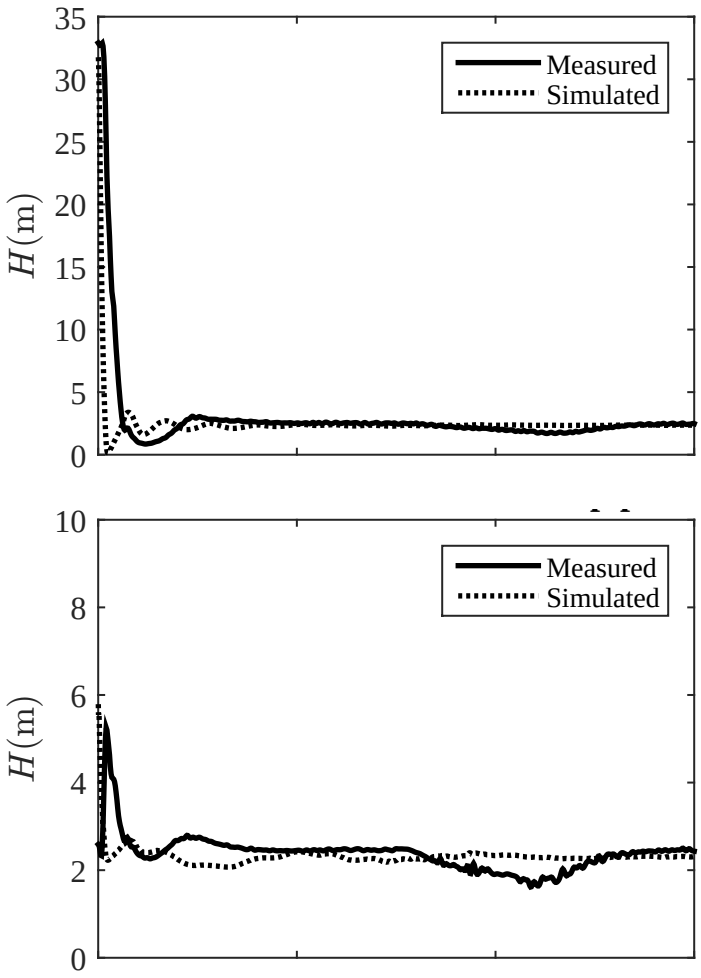

Figure 3.13: Comparison of measured and simulated pressure head at PT1 and PT2. The immediate pressure drop in the air tank and pressure variation at the time of air release were commonly observed.

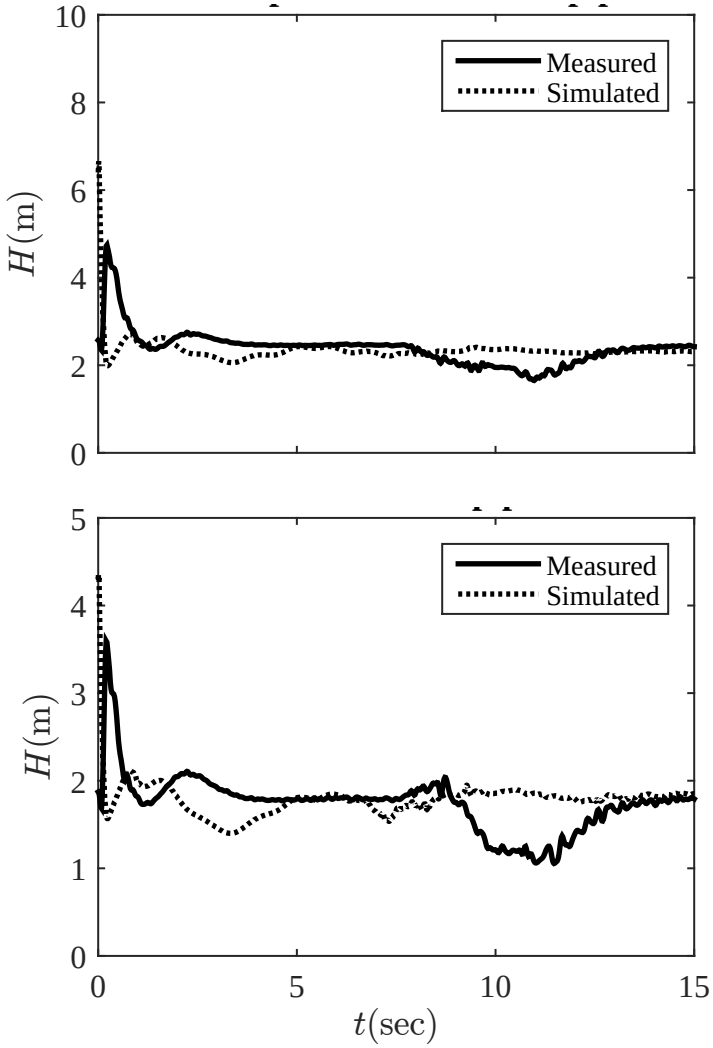

Figure 3.14: Comparison of measured and simulated pressure head at PT3 and PT4. The immediate pressure drop in the air tank and pressure variation at the time of air release were commonly observed. The pressure variation during the air release was most noticeable at PT4 which was located at the bottom of the vertical pipe.

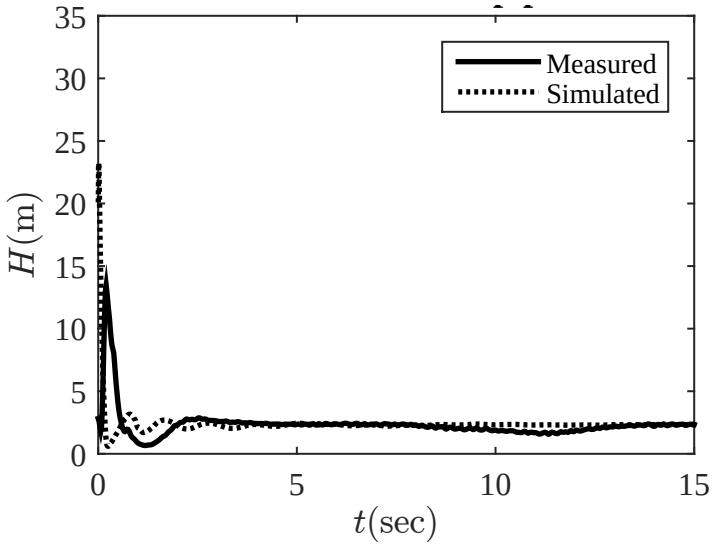

Figure 3.15: Comparison of measured and simulated pressure head at PT5.

analysis process described in Appendix A (Figure 3.16). For the field view section 4, the air-water interface could not be tracked due to the simultaneous rise of the air-water interface and the overflow. Therefore, the air-water interface evolution process was tracked for the field view sections 1 through 3. The identified air-water interface was then compared with the numerical simulation.

Similarly, the air-water interface evolution in the vertical pipe was analyzed for the numerical simulation (Figure 3.17). Then the comparison between the air-water interface location of the physical experiment and numerical simulation were made (Figure 3.18. For each of the three field views, two experimental trials are shown. Observing from view 1 to view 3, the numerical simulation underestimated the air-water interface progression as it rose through the vertical pipe. Initially, the predicted air-water interface evolution followed the experimental result in close proximity. However, around one second into the simulation, the interface progression in the numerical model stagnated. During this

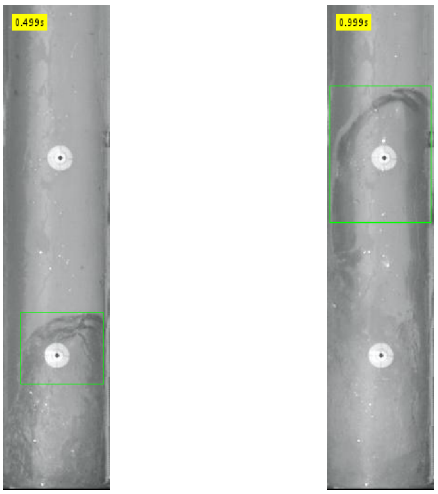

Figure 3.16: Representative snapshots of air-water interface tracking process are shown. Comparing images from one time step to the next, calculating a location where a sharp gradient exists can locate the air-water interface.

time, the air flow rate into the vertical pipe increased and formed a slug that fills the majority of the pipe cross section. After the stagnation, the air pocket continued to ascend in the vertical pipe. While the stagnation around one second resulted in a time lag in the numerical simulation, the slope of the interface evolution was retained.

3.3.2 Grid convergence

The grid convergence of the presented numerical simulation was examined. The numerical reproduction of a spring type geyser experiment was simulated using three mesh sizes: fine, medium, and coarse (Table 3.2). The computed pressures in the air tank (PT1) were compared between the three grid sizes. The grid convergence index (GCI) was computed (Roache, 1997). The global order of accuracy, P, was 8.12 and oscillatory convergence occurred at 87.13% of the simulation time. The averaged apparent order of accuracy was used to access the GCI values for individual time steps, which was plotted in the form of error bars (Figure 3.19). The maximum discretization uncertainty was 0.0693 m and occurred at t=0.873 s. Majority of the simulation time resulted in an oscillatory convergence. However, the magnitude of the discretization uncertainty was less than 0.5% of the initial pressure in the air tank throughout the simulation. The presented spring-type geyser simulation involved a large scale computational geometry containing a highly unsteady multiphase flow. Some of the short comings found in the gird convergence analysis of the presented numerical simulation can be addressed by utilizing higher resolution mesh, advanced computing resource, and improved initial conditions.

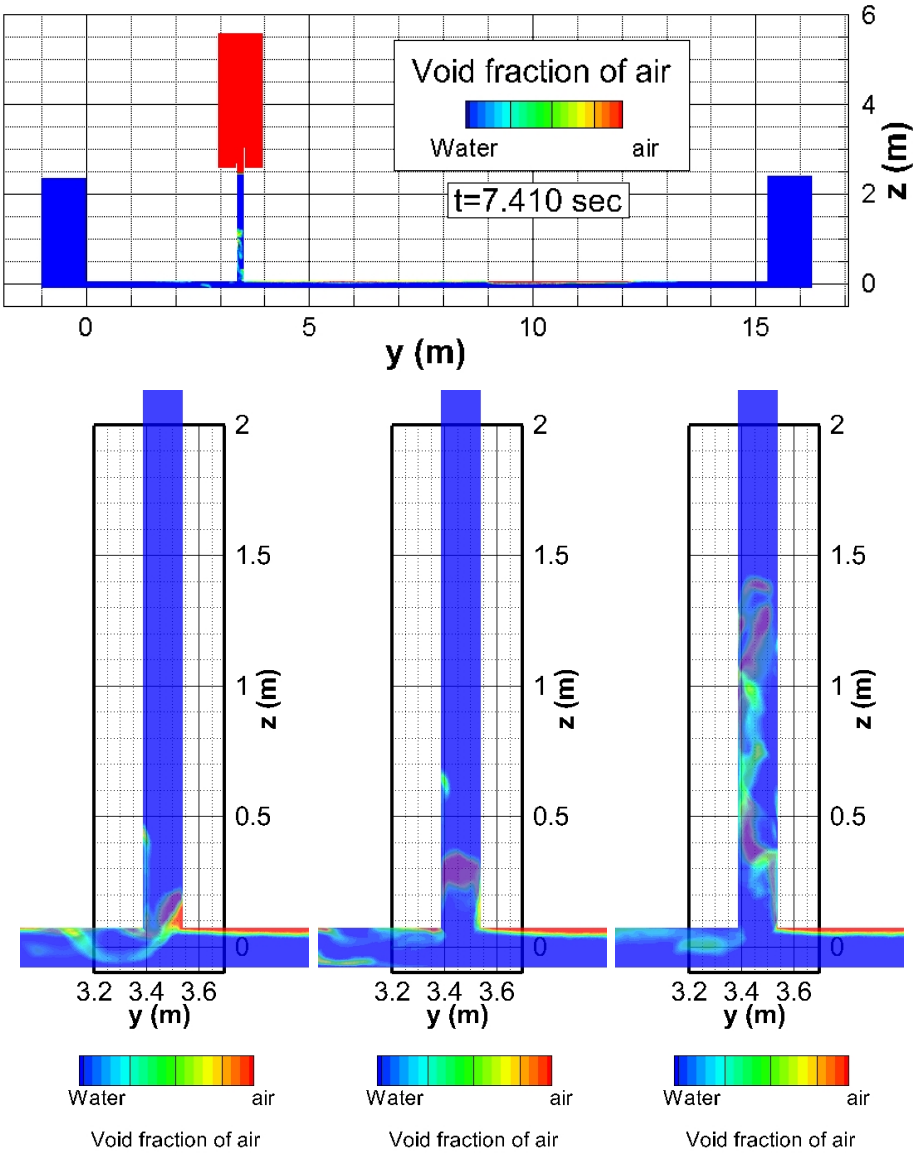

Figure 3.17: Void fraction snapshots of the numerical simulation results are shown. The pressurized air was released to the horizontal pipe at the beginning of the simulation. The air expanded and migrated towards the vertical pipe.

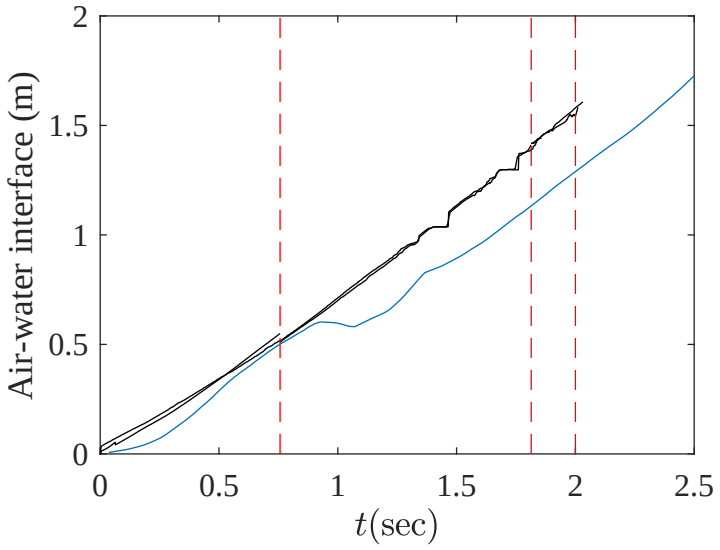

Figure 3.18: An air-water interface progression of the physical experiment (Black) and the numerical simulation (Blue) are shown. The red dotted lines represent the field one, two, and three. The experimental result include two experimental trials, hence two lines. Around one second, the numerical simulation experienced a stagnation while increased rate of air entered the vertical pipe.

Table 3.2: Details of the meshes used for the grid convergence study are shown.

	Mesh	Characteristic mesh size (h)	Total cell number
Grid 1	Fine	0.01185 m	260685
Grid 2	Medium	0.01540 m	131462
Grid 3	Coarse	0.01740 m	99354

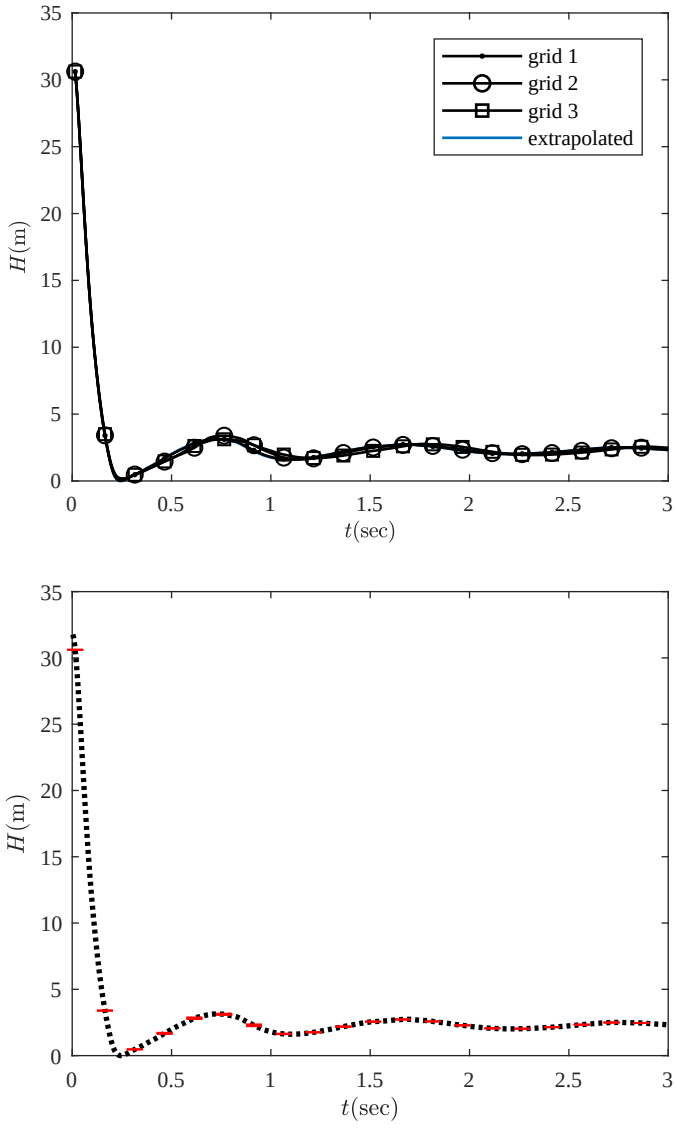

Figure 3.19: Grid convergence results are shown. (a) computed pressure from the three different grid sizes and (b) computed and extrapolated pressure with discretization error bar.

3.4 Violent geyser

A physical experiment which produced violent geysers was numerically reproduced. The physical experiment apparatus of Elayeb (2016) was consisted of a horizontal pipe, a vertical pipe and an air tank (Figure 3.20). There was no flow in the horizontal pipe and the experiment conditions were prescribed that both horizontal and vertical pipes are full of water and the pressure in the air tank corresponds to the hydrostatic pressure from the height of the water column in the vertical pipe. For further description of the experimental setup, the reader is referred to Elayeb (2016). The physical experiment tested four vertical pipe lengths: 3, 6, 9, and 12 m. The 12 m vertical pipe experiment was selected and numerically reproduced. Pressure measurements and geyser overflow heights were compared. The numerical simulation adopted the same geometry as the physical experiment except for the extended region shown in Figure 3.20. This region was given to simulate the atmospheric pressure beyond the outlet of the vertical pipe and capture the ejecting overflow during a geyser event.

Similar boundary conditions as previously presented numerical simulations were used (Figure 3.21). The pipe walls were non-slip walls, the air tank and the side walls of the extended region were slip walls, and the top surface of the extended region was a pressure outlet boundary maintained at a constant atmospheric pressure. The computed and the measured pressure were compared. The locations of the pressure transducers are indicated in Figure 3.20. The initial pressure in the air tank was 117720 Pa (H = 12m).

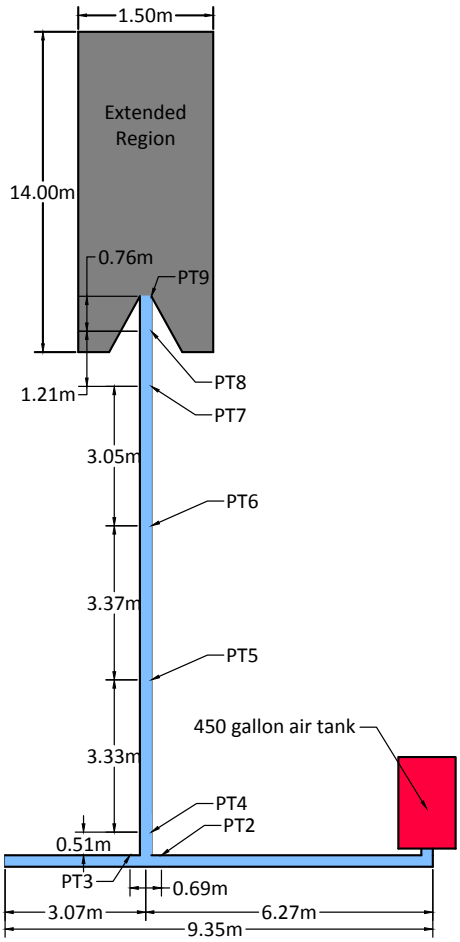

Figure 3.20: A numerical representation of the physical experiment facility, which consisted of a vertical pipe, horizontal pipe and an air tank, is shown. The extended region colored in gray simulated the overflow beyond the vertical pipe.

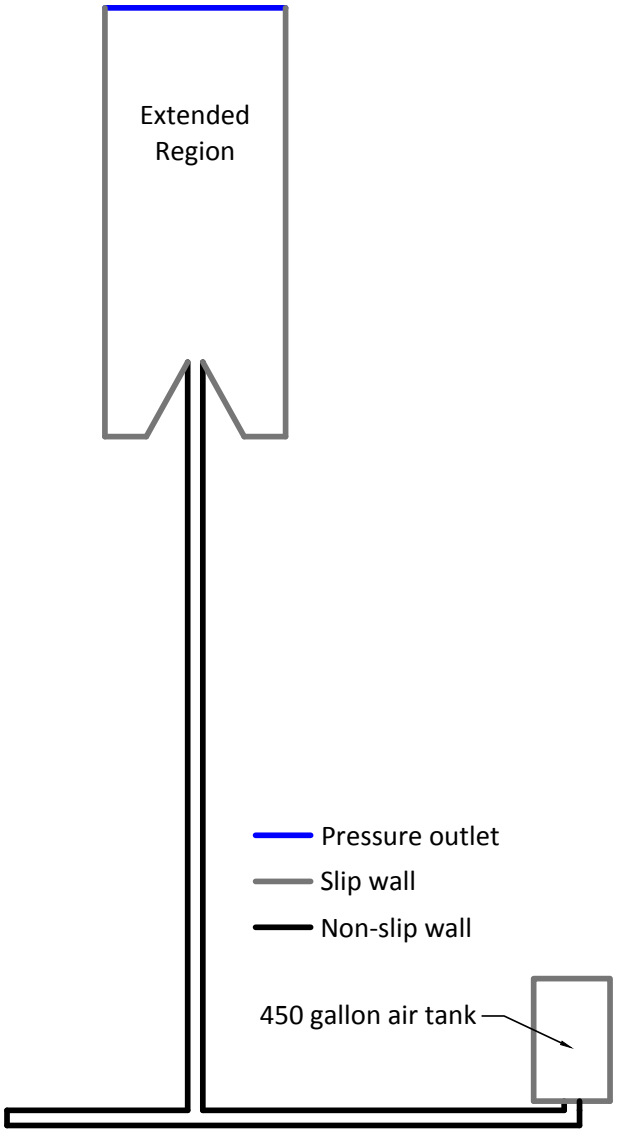

Figure 3.21: Boundary conditions used in the violent geyser numerical simulation. Walls of the overflow region and the air tank were slip walls. The top surface of the overflow region was a pressure outlet boundary maintained at the atmospheric pressure. The walls of the horizontal pipe and the vertical pipe were non-slip walls.

3.4.1 Result

The sharp pressure drop preceding geyser eruptions in the physical experiment cannot be sufficiently captured due to the inherent nature of the adapted numerical models. The finite volume approach averages the flow in space and the implicit time marching scheme used for simulation stability averages the flow in time. This prevents the numerical simulation from capturing extreme events observed in the physical experiments. Thus, comparing the numerical simulation result to the average of multiple experimental trials would be a reasonable indicator of the numerical model performance. Five repeating trials were performed in the physical experiment. A mean of the five experimental trials were calculated and compared with the numerical simulation result. The numerical simulation and the physical experiment showed a reasonable agreement (Figures 3.22 through 3.28). Note that in figures 3.24 through 3.28, the 95% confidence interval of the measured pressure is shown around the mean.

Around 2 seconds into the experiment and the numerical simulation, a small perturbation occurred when the air began to enter the vertical pipe. As the flow developed, a larger oscillation was observed. With increased air flow into the vertical pipe, some water overflow at the top of the vertical pipe and further accelerated the air flow into the vertical pipe (Figures 3.22 and 3.23).

One overflow of water and several air-water mixture ejections were observed (Figures 3.29 to 3.31). The maximum geyser height observed by the numerical simulation was 6.66 m whereas the physical experiment resulted in geyser heights that reached 22 - 30 m with the same initial conditions. The geyser eruption height discrepancy is further discussed in Chapter 4. Despite the discrepancy in the maximum overflow height, some qualitative characteristics of the violent geyser formation were captured. For example,

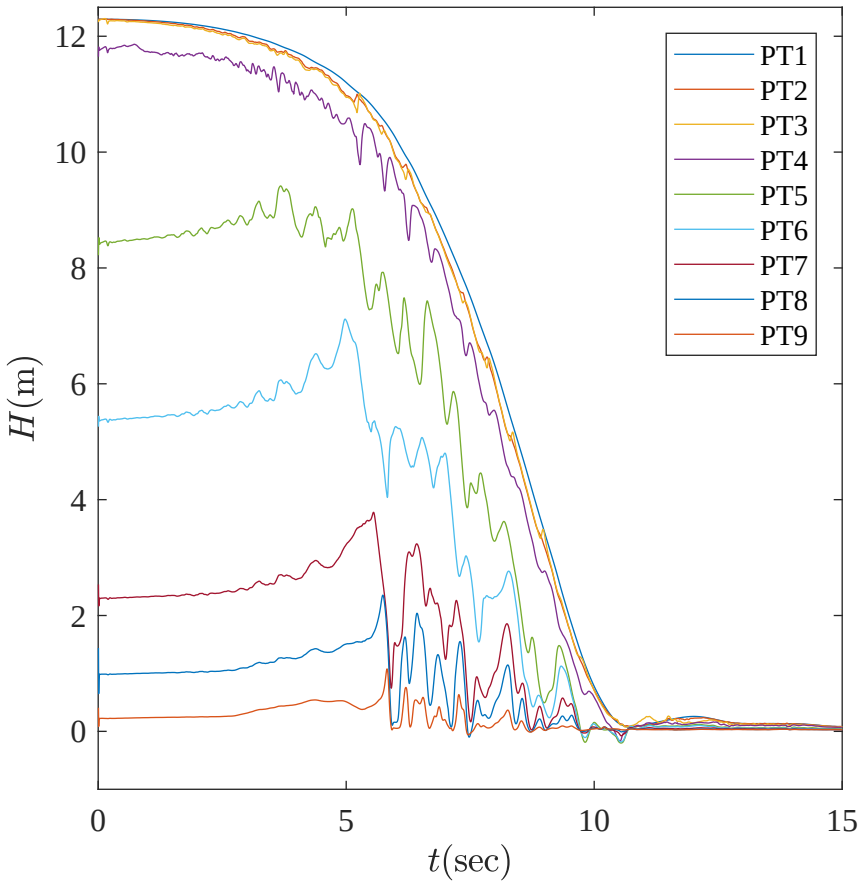

Figure 3.22: Computed pressure head at nine locations of the computational domain are shown. The decreasing trend reflects the depressurizing process of the system. The probe locations are shown in Figure 3.20.

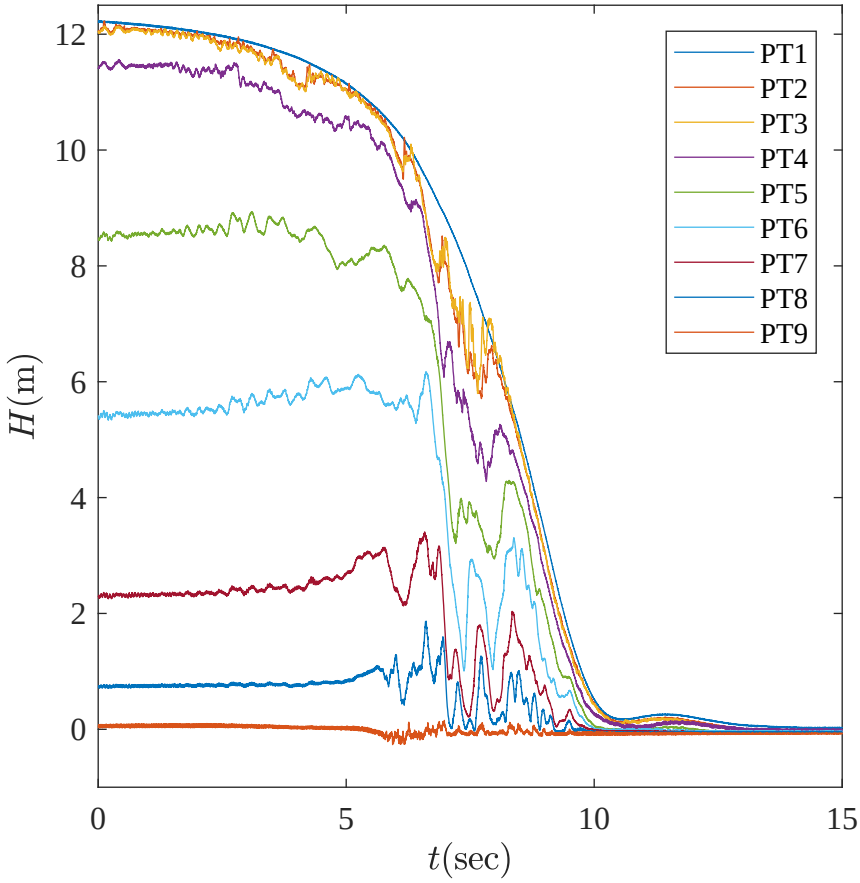

Figure 3.23: Mean pressure head resulted from five experimental trials are shown. The pressure was measured at nine locations of the physical experiment. The decreasing trend reflects the depressurizing process of the system. The probe locations are shown in Figure 3.20.

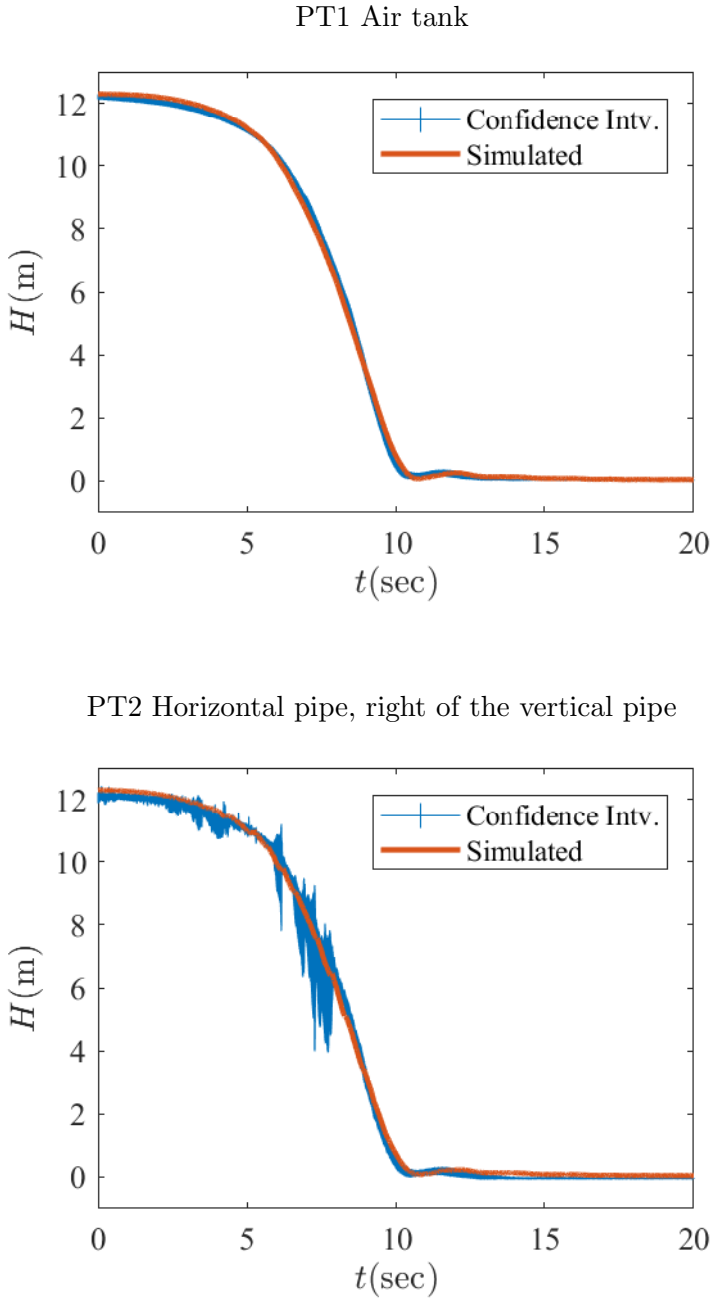

Figure 3.24: Comparison of simulated pressure head from the 3D-CFD simulation and mean measured pressure head from the physical experiment are shown. The 95% confidence interval around the mean is also shown. Whereas the overall trend of the pressure measurement was well captured, the localized pressure peaks were not captured in the numerical model.

PT3 Horizontal pipe, left of the vertical pipe

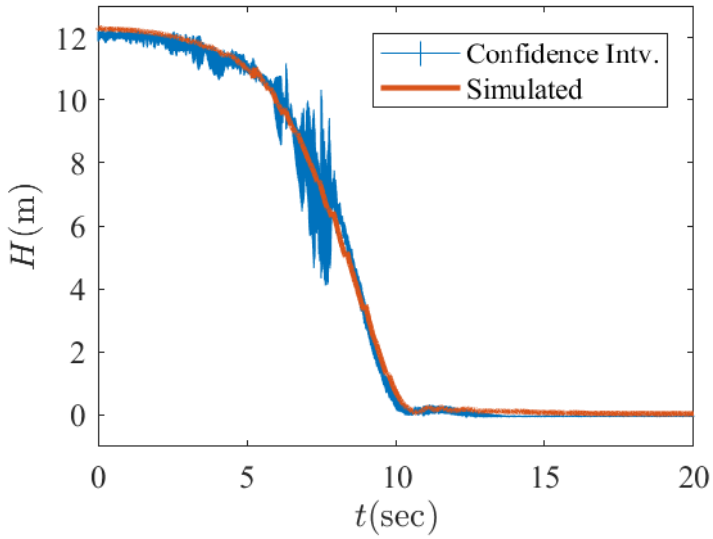

PT4 Vertical pipe, lowest pressure transducer

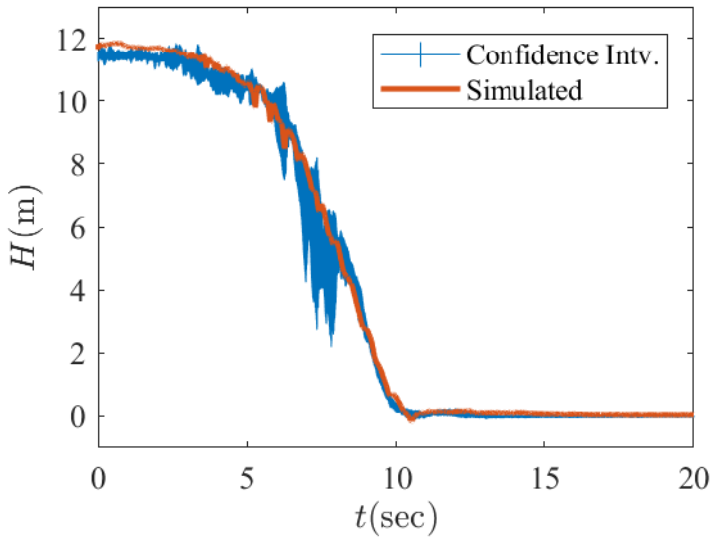

Figure 3.25: (Continued) Comparison of simulated pressure head from the 3D-CFD simulation and measured pressure head from the physical experiment are shown. The 95% confidence interval around the mean is also shown.

PT5 Vertical pipe, second lowest pressure transducer

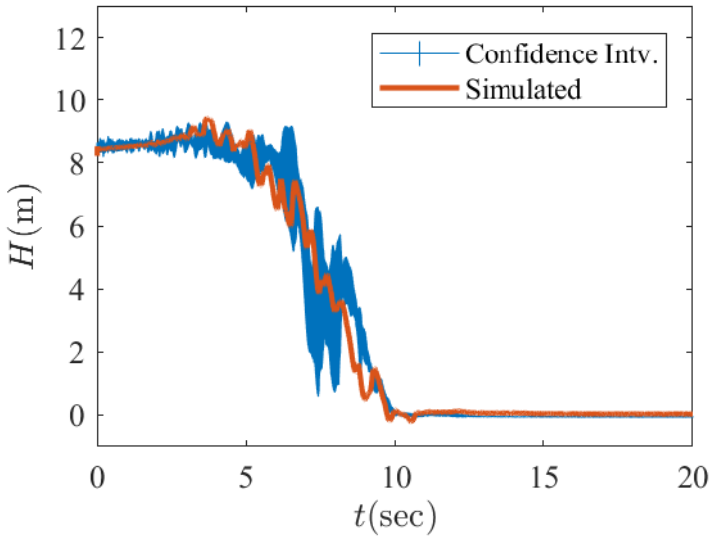

PT6 Vertical pipe, third lowest pressure transducer

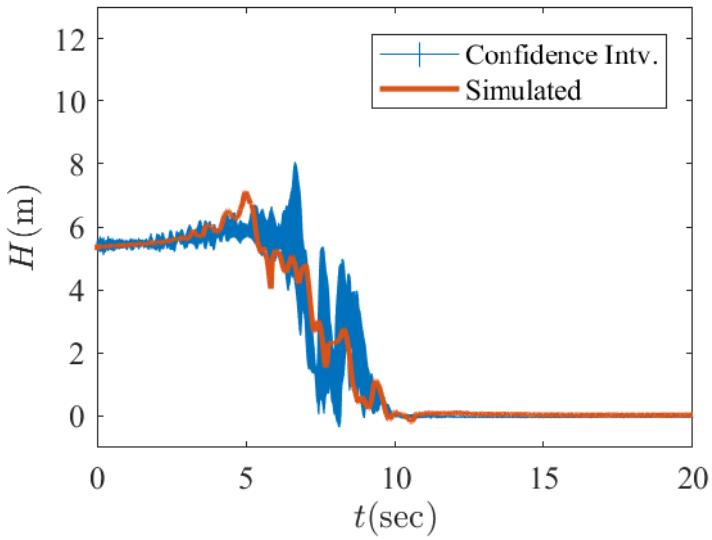

Figure 3.26: (Continued) Comparison of simulated pressure head from the 3D-CFD simulation and measured pressure head from the physical experiment are shown. The 95% confidence interval around the mean is also shown.

PT7 Vertical pipe, third highest pressure transducer

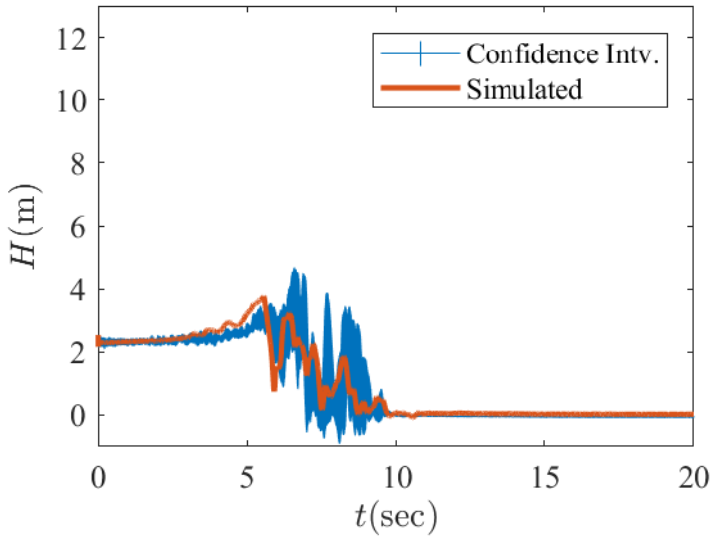

PT8 Vertical pipe, second highest pressure transducer

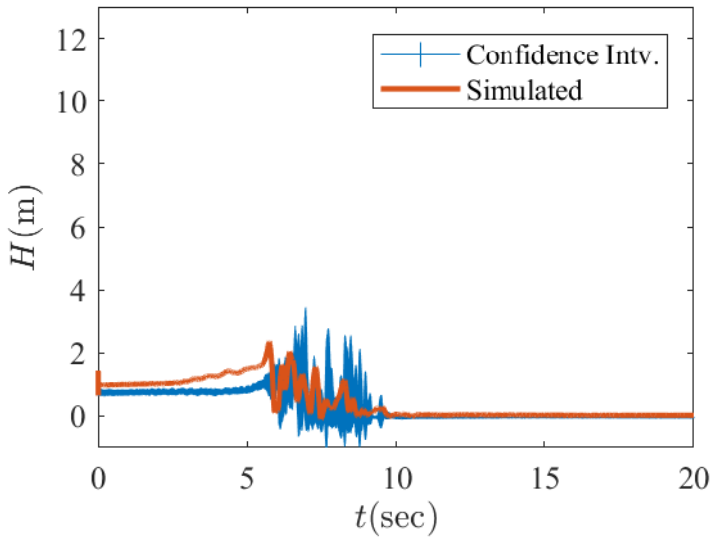

Figure 3.27: (Continued) Comparison of simulated pressure head from the 3D-CFD simulation and measured pressure head from the physical experiment are shown. The 95% confidence interval around the mean is also shown.

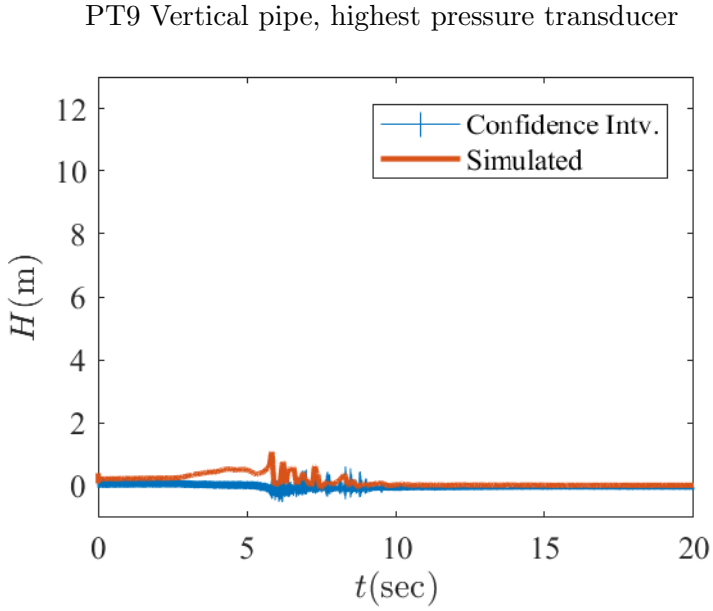

Figure 3.28: (Continued) Comparison of simulated pressure head from the 3D-CFD simulation and measured pressure head from the physical experiment at PT9 are shown. The 95% confidence interval around the mean is also shown.

the initial overflow of water followed by several ejecting air-water mixture, slugs in the horizontal pipe, and pressure oscillations throughout the pipe system can be observed through both the physical experiment as well as the numerical simulation.

Comparing the pressure differential between PT4 and PT6 (dH) immediately before the initial overflow at $t = 5.80$ seconds, the pressure gradient instantaneously decreased. While more significant, but a similar pressure drop pattern was observed in the physical experiment 3.32. This is because a continuous void filled the majority of the vertical pipe length during this time. After the initial overflow, the void content of the liquid in the vertical pipe increased and caused the mixture density to decrease. The remaining air in the horizontal pipe pushed the air-water mixture in the vertical pipe upwards and this motion resulted in an increased air flow into the vertical pipe and subsequent ejecting eruptions. In both numerical simulation as well as the physical experiment, a small perturbation was observed around two seconds into the fluid interaction. This oscillation became amplified with time.

3.5 Grid convergence

The grid convergence of the presented numerical simulation was examined. The numerical reproduction of the violent geyser experiment was simulated using three mesh sizes: fine, medium, and coarse (Table 3.3). The grid convergence index (GCI) was computed (Roache, 1997). The computed pressure in the air tank (PT1) was compared between the three grid sizes. The global order of accuracy, P, was 50.51 and the oscillatory convergence occurred at 33.20 % of the simulation time. The averaged apparent order of accuracy was used to assess the GCI values for the individual time steps, which was plotted in the form of error bars (Figure 3.33). The maximum discretization uncertainty

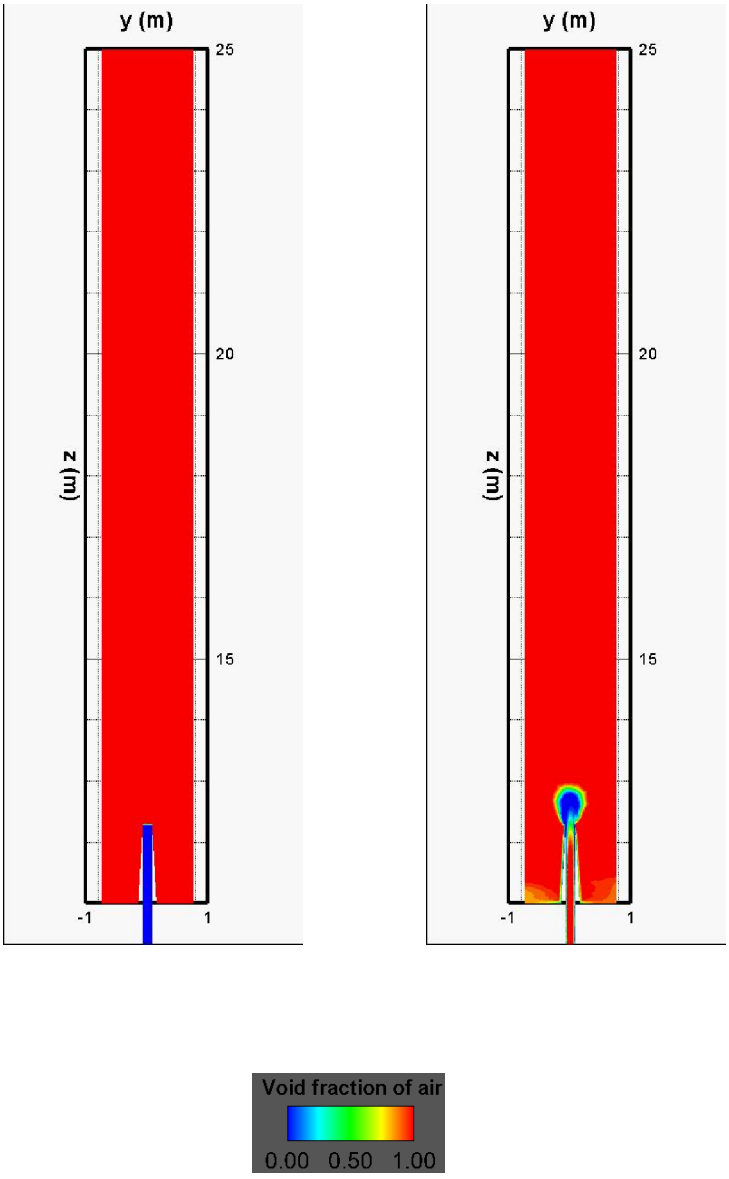

Figure 3.29: Void fraction snapshots during the initial overflow are shown. (a) $t = 0.00$ s and (b) $t = 5.80$ s.

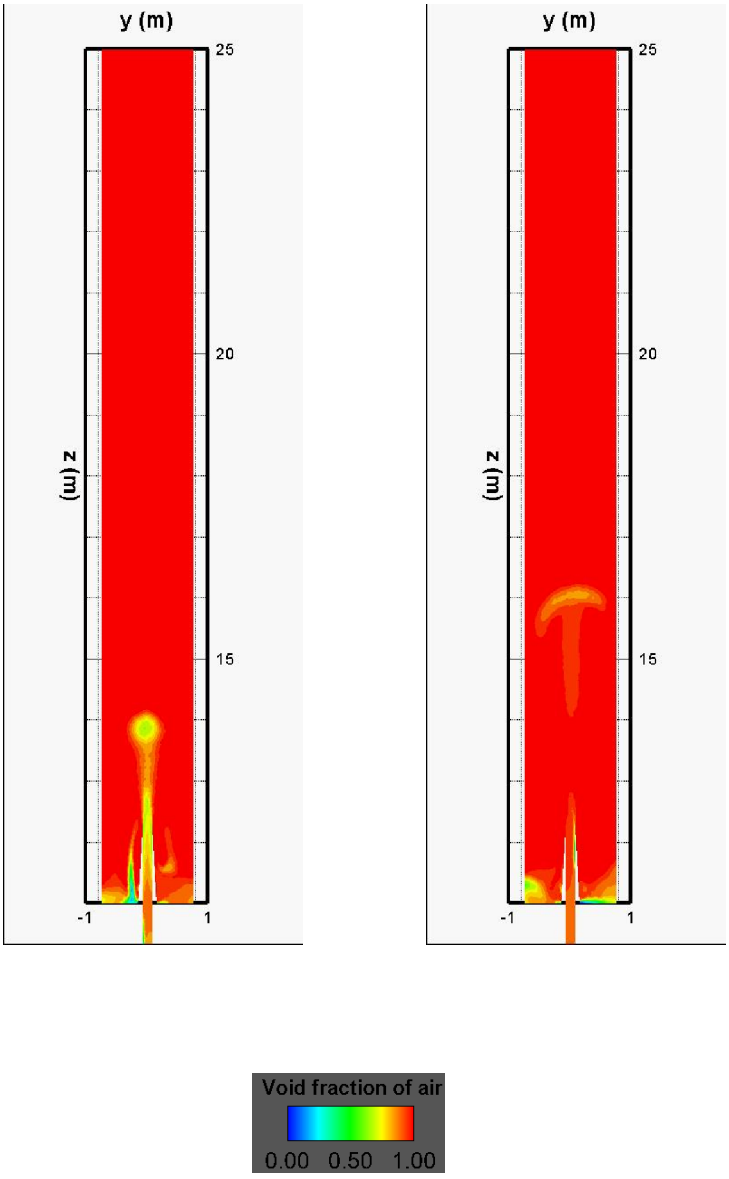

Figure 3.30: Void fraction snapshots during the first geyser eruption are shown. (a) $t = 6.65$ s and (b) $t = 7.25$ s.

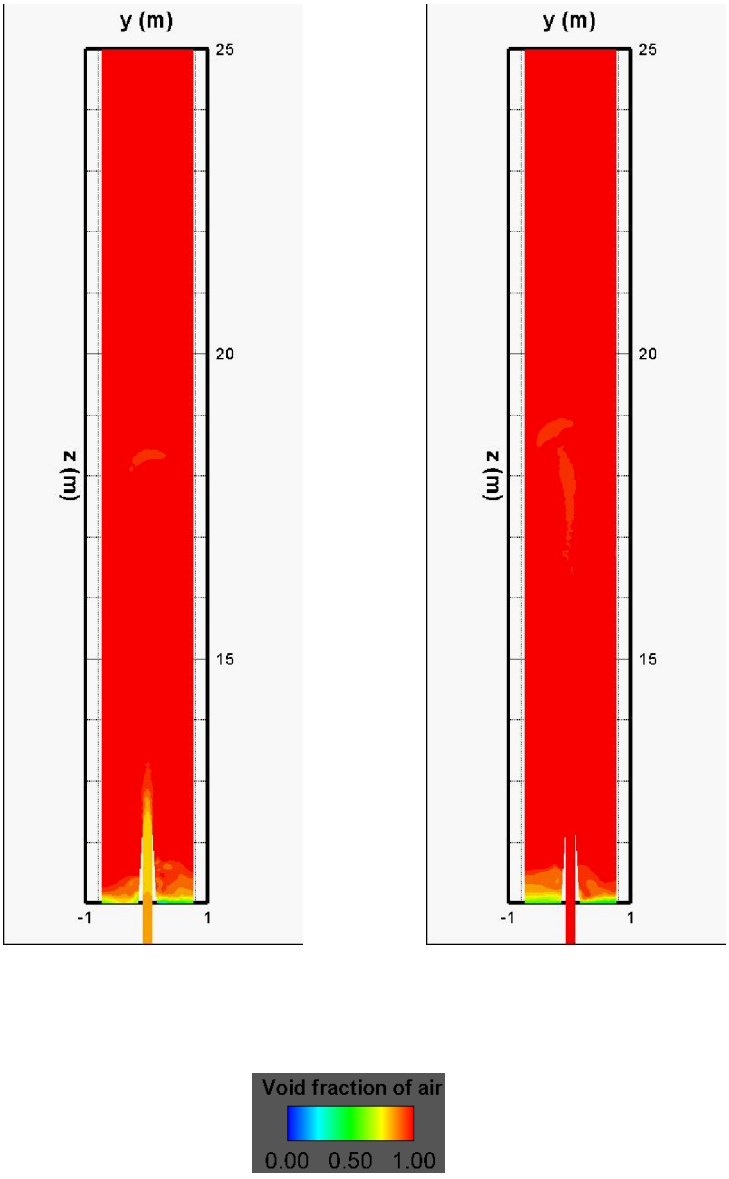

Figure 3.31: Void fraction snapshots during the second geyser eruption are shown.(a) $t = 7.90$ s and (b) $t = 8.95$ s.

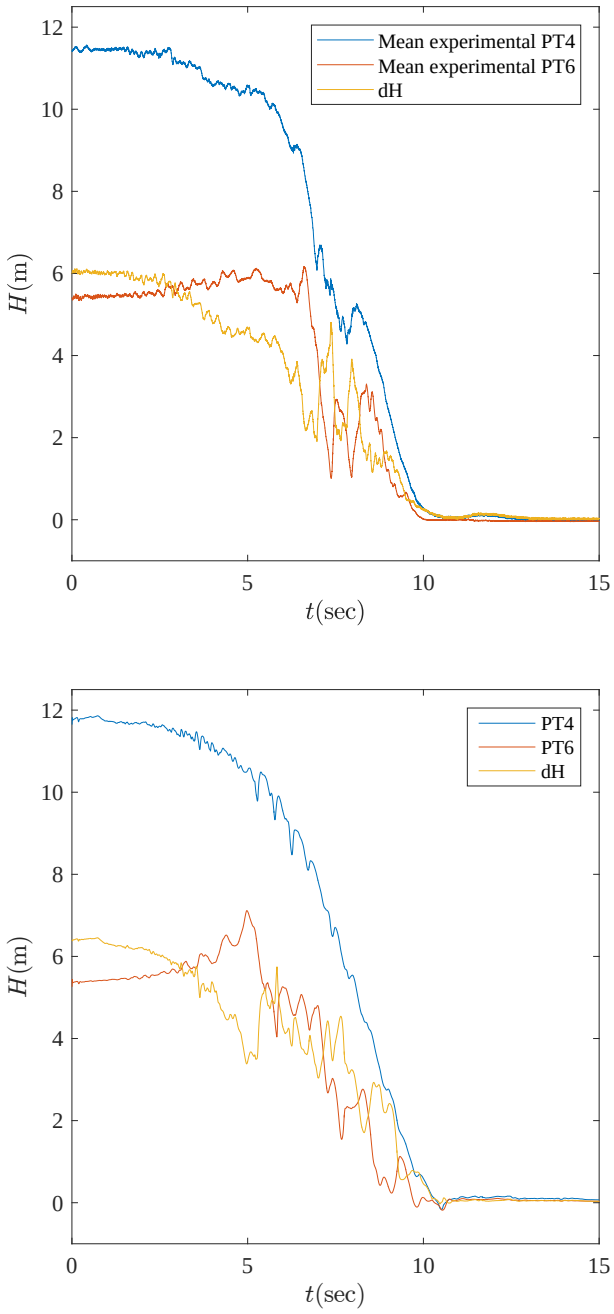

Figure 3.32: The pressure gradient between PT4 and PT6 (dH) is shown for (a) measured and (b) simulated pressure heads.

Table 3.3: Details of the meshes used for the grid convergence study are shown.

	Mesh	Characteristic mesh size (h)	Total cell number
Grid 1	Fine	0.0165 m	264978
Grid 2	Medium	0.0214 m	259507
Grid 3	Coarse	0.0300 m	99032

was 0.028 m and occurred at t=10.52 s.

The comparison between measured and computed pressure in the air tank (PT1) falls within the grid convergence error 3.34. Due to the nature of the adapted numerical approaches, RANS model, turbulence closure model and discretization schemes, the instantaneous instabilities present in the physical experiment, such as the drastic pressure drop preceding geyser eruptions cannot be numerically captured sufficiently. However, its comparison with the mean of the multiple experimental trials and grid convergence error revealed that the chosen numerical approach is capable of capturing physical processes involved in violent geysers.

3.6 Conclusion

Physical experiments studying entrapped air release through a vertical pipe was numerically reproduced. The first numerical simulation computed pressure oscillations in the horizontal pipe during the expansion, migration, and rise of an entrapped air. The second numerical simulation reproduced a physical experiment studying the release process of a pressurized air through a vertical pipe. The rising speed of the air-water interface was compared with the physical experiment. The third numerical simulation reproduced

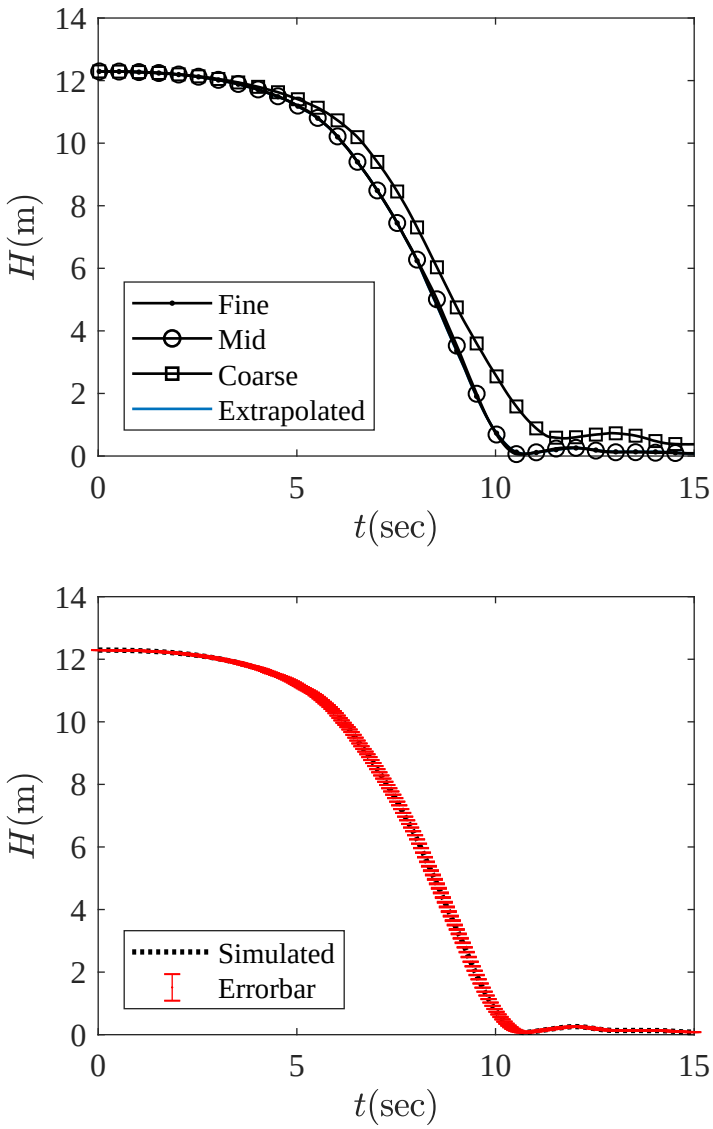

Figure 3.33: Grid convergence of the numerical simulation;(a) computed pressure from the three different grid sizes and (b) final grid solution and error bars are shown.

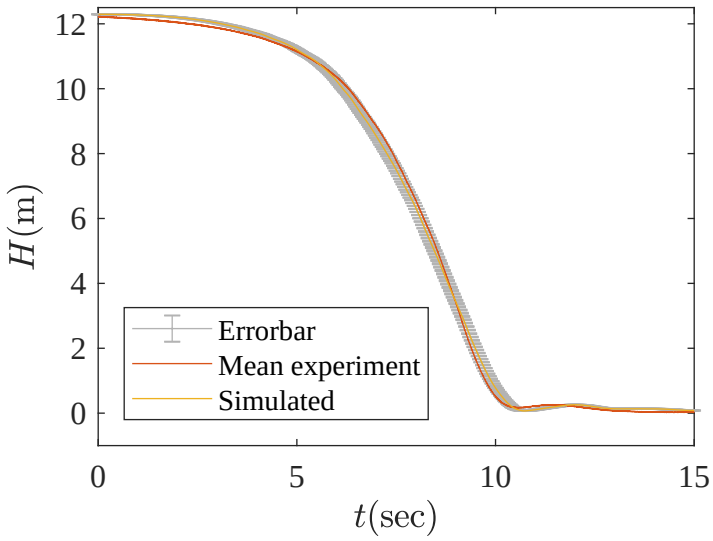

Figure 3.34: For the pressure in the air tank, the fine grid solution, mean measured pressure and GCI error bar are shown. The slight discrepancy between measured and simulated data falls within the envelope of grid convergence error.

the physical experiment of Elayeb (2016). The measured and computed pressure at several points of the pipe system were compared. The rising trajectory of the entrapped air pocket in the numerical simulation was further analyzed in relation to the pressure gradient in the vertical pipe.

In the first numerical simulation case, the amplitude of the computed pressure oscillation decreased with time until the air pocket was released to the atmosphere. Grid convergence of the numerical simulation was evaluated. Overall, the presented numerical simulation method was able to capture the amplitude and frequency of the pressure oscillation in the horizontal pipe. The pressure oscillation amplitude decay was better captured with the adiabatic process assumption compared to the isothermal assumption.

In the second simulation case, just as the physical experiment, a specified volume of pressurized air was introduced to a horizontal pipe with a constant flow. The comparison

of the experiment and simulated data showed that the simulation method used was able to capture physical processes observed in the laboratory. For example, a pressure spike throughout the system immediately following the air tank valve opening was also captured in the numerical simulation. Additionally, the variation in the hydrostatic pressure in the horizontal pipe when the air pocket rose through the vertical pipe was emulated in the numerical simulation. Furthermore, the comparison of rising air trajectory between the physical experiment and the numerical simulation revealed that the numerical simulation method is capable of capturing a single air pocket release process that involves overflow.

In the third simulation case, a physical experiment of Elayeb (2016) was reproduced. On the contrary to the two previous cases, the final simulation was able to produce multiple ejecting overflows through the vertical pipe just as the physical experiment. The simulation result revealed that instantaneous pressure gradient variation in the vertical pipe proceeds with the initial overflow occurrence. While the numerical simulation did not achieved the observed maximum height in the physical experiment, the simulated mean pressure compared well with the measured pressure. Elayeb (2016) states that the erupting geyser derive from pressure transients. The discrepancy in the geyser eruption height can be attributed to the fact that the numerical simulation failed to capture these pressure transients. In Chapter 4, further comparison with a physical experiment have been made to understand the integrity of the numerical simulation result.

One can conclude that the proposed simulation method was able to closely approximate air-water interactions and pressure oscillations in pipe systems under varying geyser scenarios. The three presented case studies show that the simulation method closely predicted the mean pressure trends while the shortcomings exist in capturing instantaneous pressure peaks. The validated numerical simulation method was used in Chapter 4 in

the numerical experiment.

Chapter 4: Qualitative analysis of geyser features

The physical experiment of Leon (2018), which was a furtherance of the experiment presented in Elayeb (2016) and an in-depth visualization study, was numerically reproduced to address some of the short comings of the previously used numerical simulation method when attempting to simulate violent geysers. A grid refinement study was performed to resolve the discrepancy found in slug formations in the horizontal pipe between the numerical simulation and the physical experiment. Based on the dimensional analysis discussion in Chapter 2, a numerical experiment was performed to identify the effect of two selected variables, initially available volume of water in the vertical pipe and air in the system, on the violent geyser height, eruption velocity and number of eruptions.

4.1 Flow feature visualization

Leon (2018) carried out a detailed visualization experiment on violent sewer geysers. In the study, the author laid out six distinctive stages that lead to violent geyser eruptions (Figures 4.1 through 4.3). This work is one of the most recent and extensive study on fluid interactions found in a horizontal pipe when the system is undergoing a violent geyser eruption. Thus comparing the numerical reproduction of this experiment can provide a guidance to determine the credibility of the numerical experiment to follow. Of the simulations to be performed in the numerical experiment, which are listed in Table 4.2, Simulation B3 had the identical system variables, L_v and V_{air}, as the physical experiment presented in Leon (2018). A qualitative analysis of the numerical simulation

was made through a comparison with the physical experiment.

According to Leon (2018), there are six stages that lead to geyser eruptions in sewer systems. *First, a large air pocket becomes entrapped in a horizontal pipe of a sewer system (Figure 4.1.a).* This can be caused due to an uneven drainage filling process, derbies, and a system geometry susceptible to a such condition. Once entrapped, the air pocket expands and migrates within the sewer system looking for an opportunity to relieve. This was captured in the numerical model as shown in Figures 4.4 and 4.5. The slow expansion of the entrapped air, initially driven by the density current instability, arrives at the bottom of the vertical pipe. At this stage, in the numerical simulation, the expanding front of the entrapped air began to flow into the vertical pipe. As the expanding front rose through the water in the vertical pipe, the exchange between ascending air and falling water occurred. This exchange liquid rate was not strictly one-to-one as the air flow rate in to the vertical pipe increased with time. Any time a sufficient amount of water was pushed upwards, water overflew at the top of the vertical pipe. In addition, the void content of the liquid in the vertical pipe increased as small voids of ascending air accumulated at the top. As a result, the pressure differential between the vertical pipe and the entrapped air in the vertical pipe increased with time further contributing towards the accelerated air flow in to the vertical pipe.

Second, a large air pocket, which resembles the Taylor bubble, enters the vertical pipe (Figure 4.1.b). As the bubble rises, a vigorous mixing between air and water can is observed at the tail end of the rising air pocket (Figure 4.6). Similar to the physical experiment, the numerical simulation result showed a cavity of air pocket in the vertical pipe followed by the air-water mixture. This interaction corresponds to the pressure oscillations observed in Figures 3.22 and 3.23. As the cavity of air ascended in the vertical pipe, the contraction and expansion of the rising air resulted in the pressure

Figure 5: Geyser Processes (a) air pocket approaching dropshaft

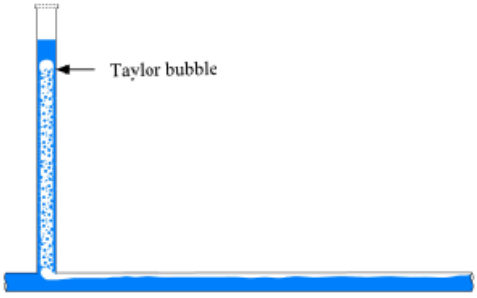

(b) Rising of Taylor-like bubble

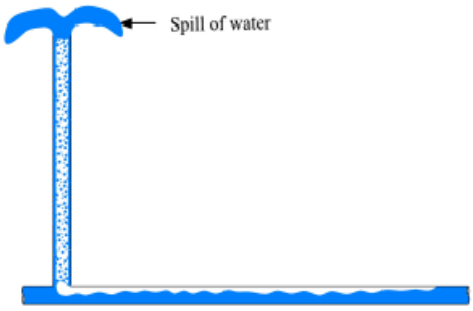

(c) Water spill and acceleration of air pocket in horizontal pipe

Figure 4.1: Schematics describing the six step process of violent geyser eruption are shown. These figures were sourced from the physical experiment of Leon (2018). Steps (a) through (c) are shown.

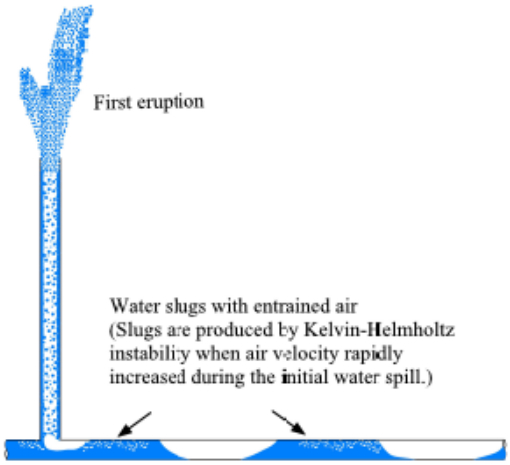

(d) First eruption and formation of liquid slugs

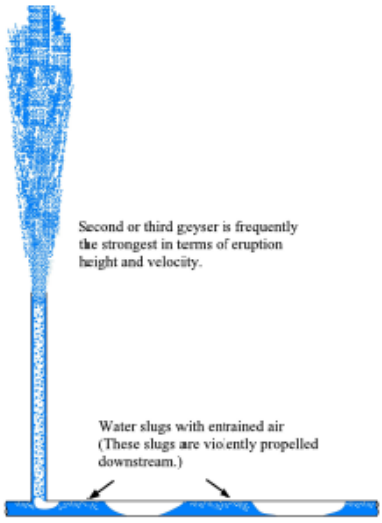

(e) Successive eruptions as a result of blowout of slugs

Figure 4.2: Schematics describing the six step process of violent geyser eruption are shown. These figures were sourced from the physical experiment of Leon (2018). Steps (d) through (f) are shown.

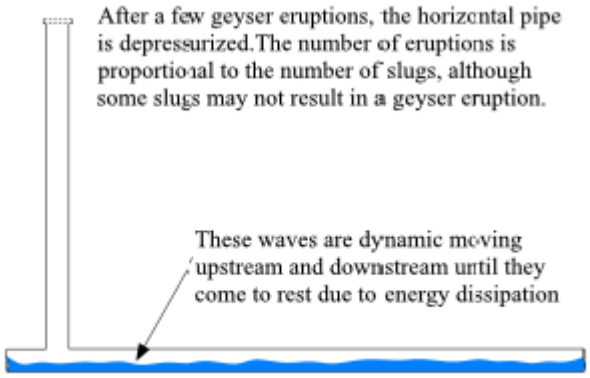

(f) Depressurization and propagation of waves in the horizontal pipe

Figure 4.3: Schematics describing the six step process of violent geyser eruption are shown. These figures were sourced from the physical experiment of Leon (2018). Step (g) is shown.

oscillation observed throughout the system.

Third, after the initial air pocket exits the vertical pipe, the water above the air pocket spills over (Figure 4.1.c). Both in the physical experiment as well as the numerical simulation, once the air pocket have exited the vertical pipe, the liquid in the vertical pipe was left with homogeneously mixed air-water mixture (Figure 4.7). At this time, hydrostatic pressure in the vertical pipe dropped suddenly due to the increased void content in the vertical pipe and unloading of the water at the top of the vertical pipe. This further contributed towards the increased air flow into the vertical pipe (Figure 4.8). t = 40 - 45 s encompasses the window where the initial air pocket have exited the vertical pipe and the remaining air have began to accelerate into the vertical pipe.

Fourth, the increased air velocity in the horizontal pipe results in the development of Kelvin-Helmholtz instability (Figure 4.1.d). This instability drove the transition from initial stratified flow to wavy and slug flows in the horizontal pipe in the physical exper-

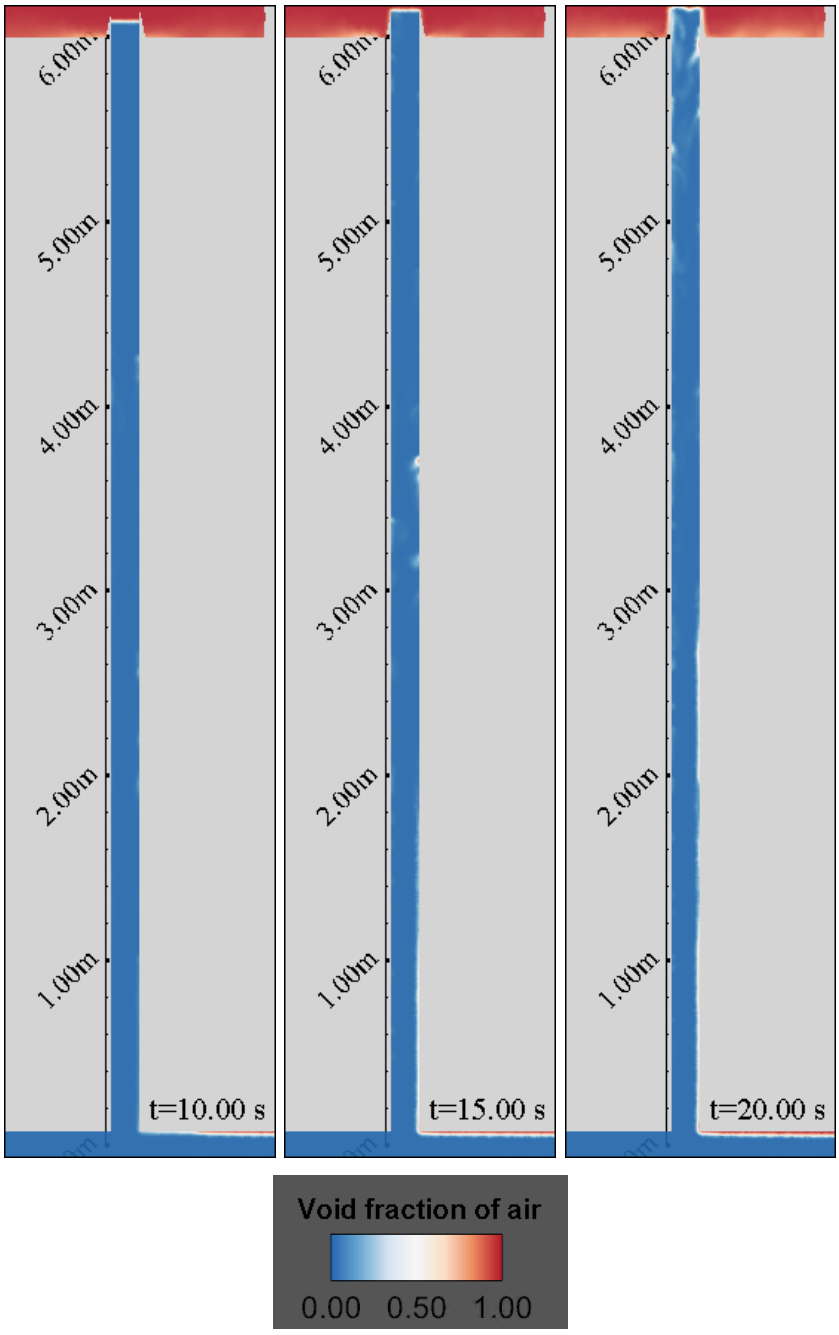

Figure 4.4: Snapshots of void fraction of air in the vertical pipe are shown for Simulation B3, $t = 10$, 15, and 20 s are shown. Shown on the right bottom of each snapshot, the expanding air in the horizontal pipe began to enter the vertical pipe.

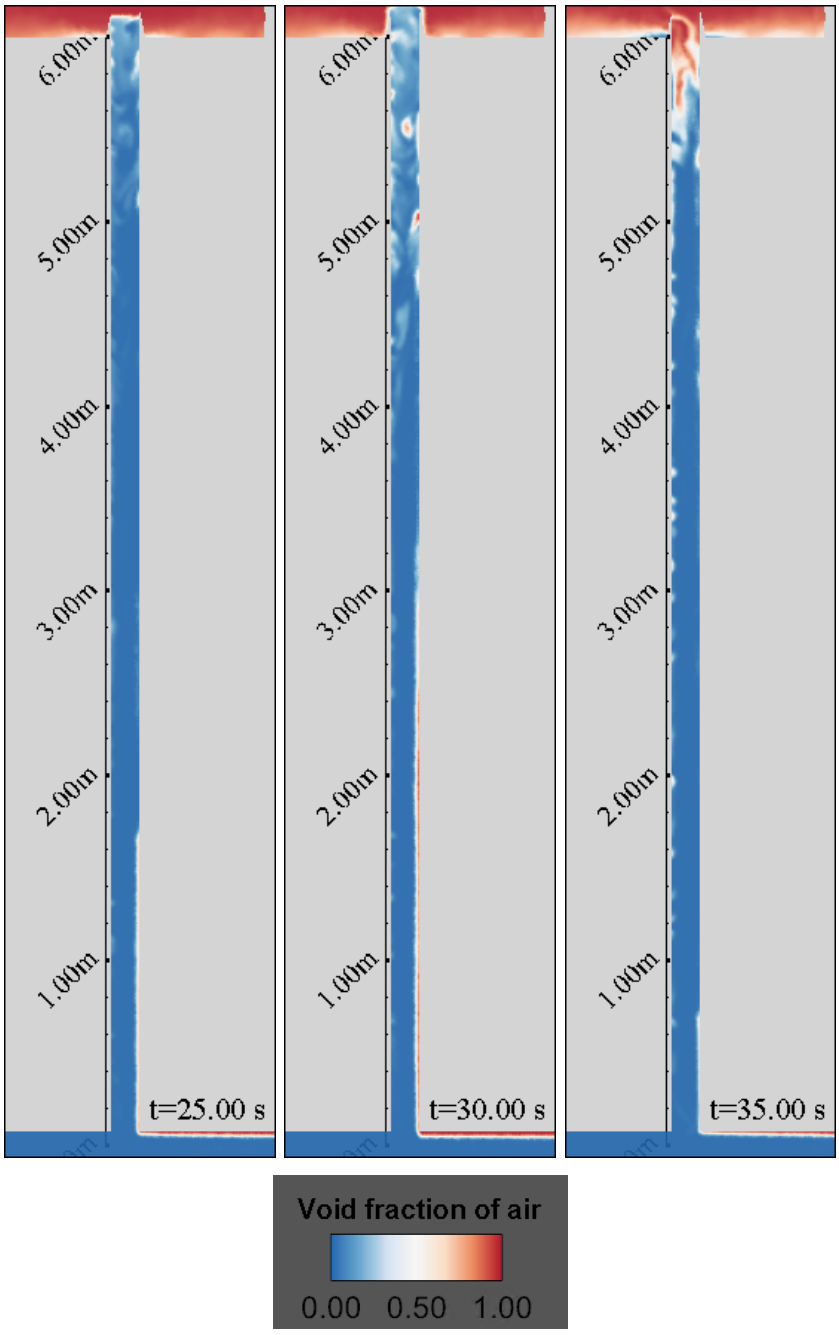

Figure 4.5: Snapshots of void fraction of air in the vertical pipe are shown for Simulation B3, $t = 25$, 30, and 35 s are shown. As time progress, air continued to enter the vertical pipe from the horizontal pipe and the void content in the vertical pipe increased.

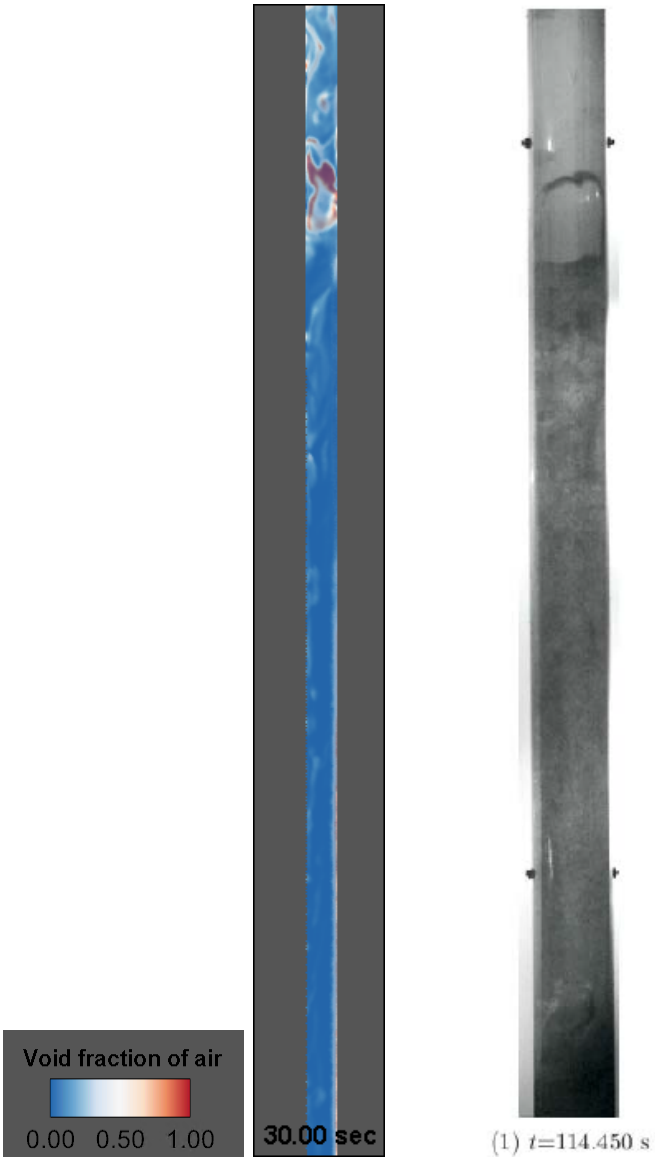

Figure 4.6: Simulation B3, L_v=6m and V_{air}=1.703 m^3, flow snapshots in the vertical pipe at t =30.05 s (numerical simulation) and t =114.450 s (physical experiment of Leon (2018) under the same system conditions).

Figure 4.7: Simulation B3, L_v=6m and V_{air}=1.703 m^3, flow snapshots in the vertical pipe at t =36.05 s (numerical simulation) and t =120.500 s (physical experiment of Leon (2018) under the same system conditions).

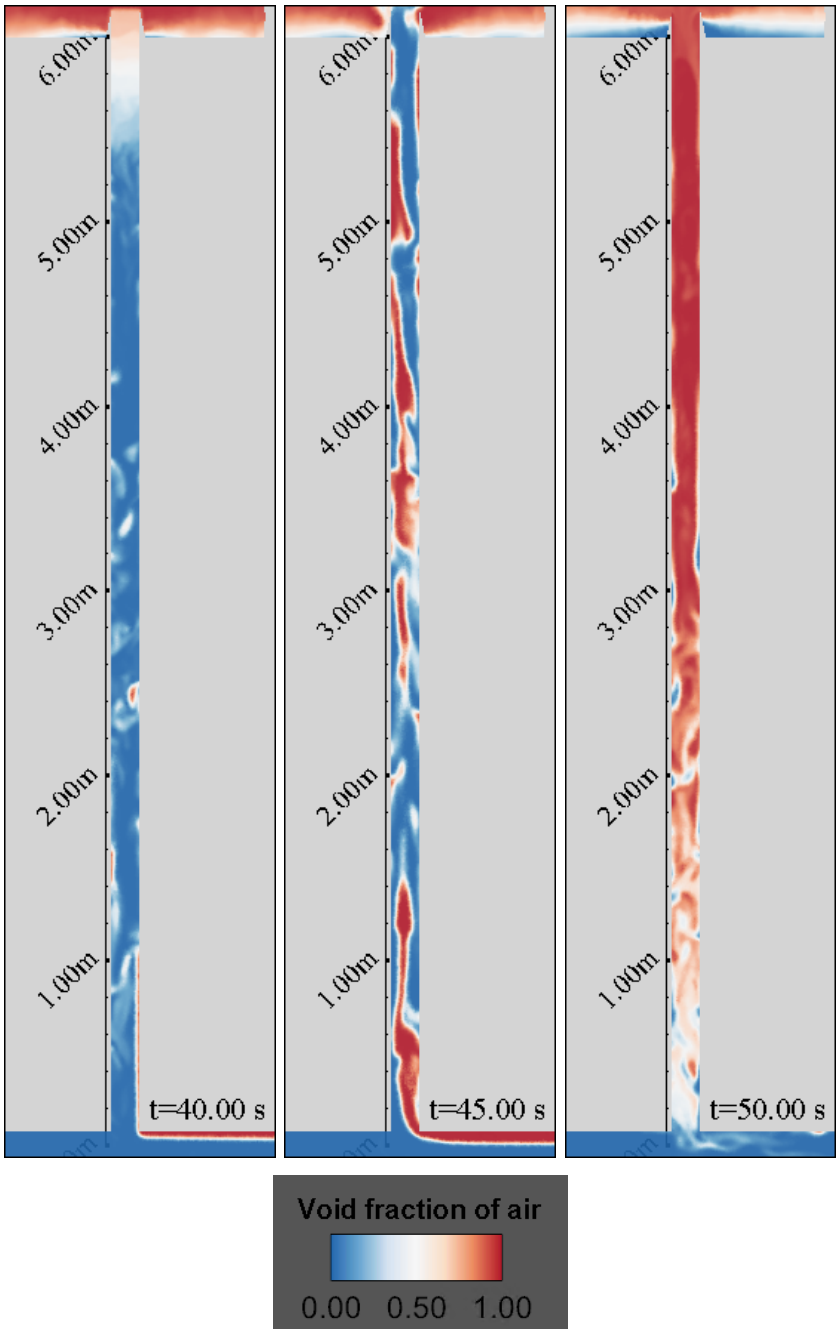

Figure 4.8: Snapshots of void fraction of air in the vertical pipe are shown for Simulation B3, t = 40, 45, and 50 s are shown. Between 40 to 45 s, a surge from the horizontal pipe reaches to the vertical pipe and air flow into the vertical pipe becomes temporarily accelerated. After the dynamic overflow at the top, by t =50 s, the water level in the vertical pipe significantly dropped.

iment (Figures 4.9 and 4.10). On the other hand, in the numerical simulation, waves or slugs were not captured. This discrepancy is discussed further in Section 4.1.1. In the numerical simulation, the air-water interface in the horizontal pipe maintained a smooth interface which was developed during the initial density current instability driven entrapped air expansion, until the initial air pocket exited the vertical pipe. Once the initial overflow and the increased void fraction in the vertical pipe have created a pressure gradient in the vertical pipe, the remaining air in the horizontal pipe began to flow into the vertical pipe in an accelerated manner. Between 30 to 36.05s, a perturbation created a surge which traveled towards the air tank. At $t = 41.35$ s, the surge reflected and traveled back to the vertical shaft (Figure 4.12). The travel direction of the reflecting surge coincides with the direction of the air flow. As a result, the surge propagation speed increased during 41.35 - 44.35 s compared to 34 - 40.25 s. The first surge took 5.75 s whereas the reflection surge took 3.00 s to complete the same distance in the horizontal pipe.

Fifth, once the slugs are formed in the horizontal pipe and the first eruption have created a pressure gradient in the vertical pipe. The slugs begin to flow into the vertical pipe in an accelerated manner and geyser eruptions are observed (Figure 4.1.e). In the numerical simulation, this process encouraged further development of slugs and eruptions. The first overflow did not achieve the highest geyser eruption height, h_g, because the first overflow occurred prior to the slug formation. The following eruptions, second or third, achieved higher eruption heights. While the surge due to the interface instability was as distinctively captured in the numerical model compared to the physical experiment result (Figure 4.12), a slug was captured from 43.35 to 44.10 s. After the slug entered the vertical pipe, the air velocity in the horizontal pipe increased (Figure 4.13). Total three great and several fading amplitudes of eruptions were captured in the

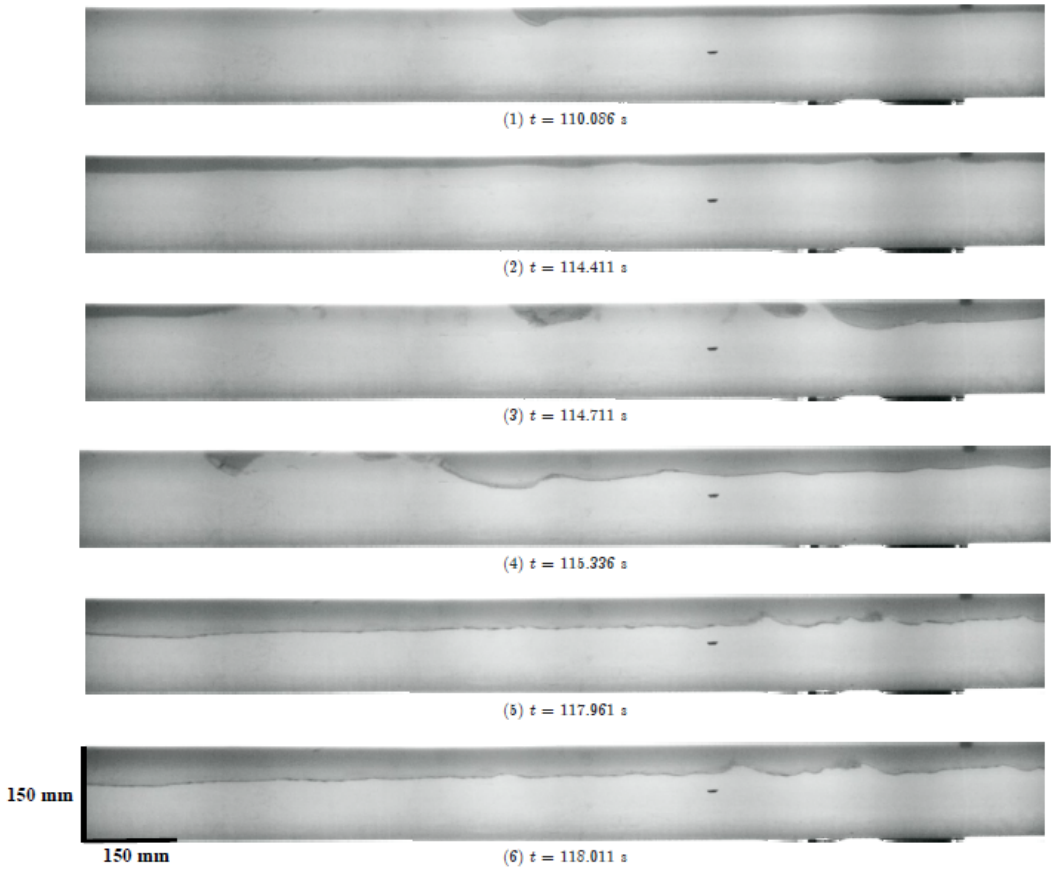

Figure 4.9: Flow snapshots in the horizontal pipe sourced from the physical experiment of Leon (2018) is shown. The experiment conditions corresponded to Simulation B3. The shown snapshots encompass the initial development of the wavy flow in the horizontal pipe at the air-water interface.

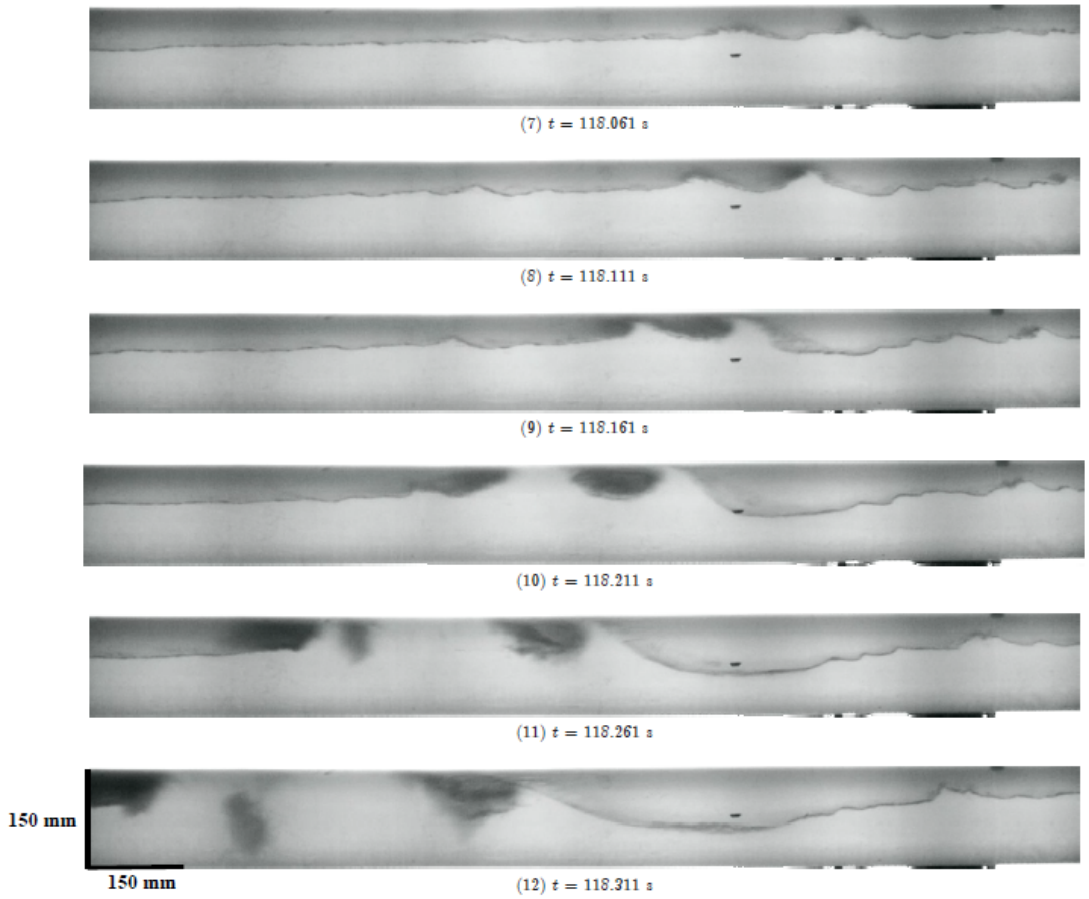

Figure 4.10: Continuation of Figure 4.9 is shown. This figure is also sourced fromLeon (2018). The presented snapshots show the transition between the wavy flow to slug flow in the horizontal pipe.

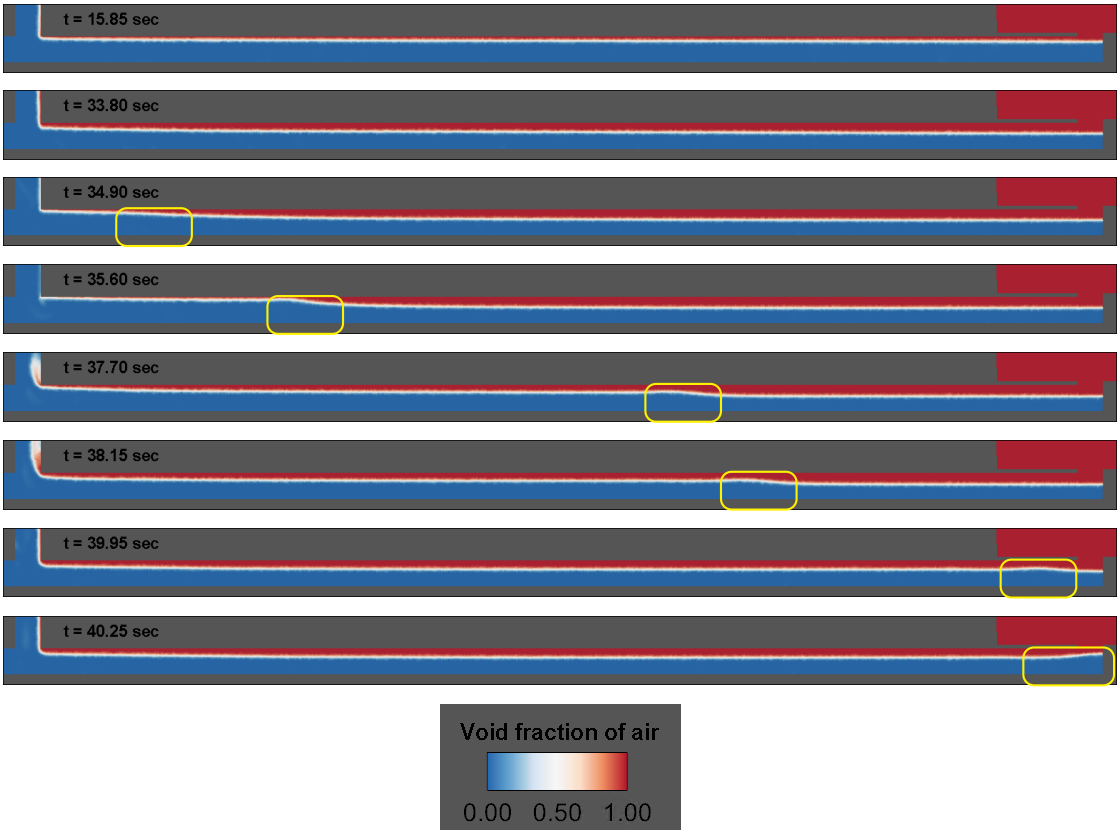

Figure 4.11: Snap shots of the void fraction of air plot are shown for Simulation B3

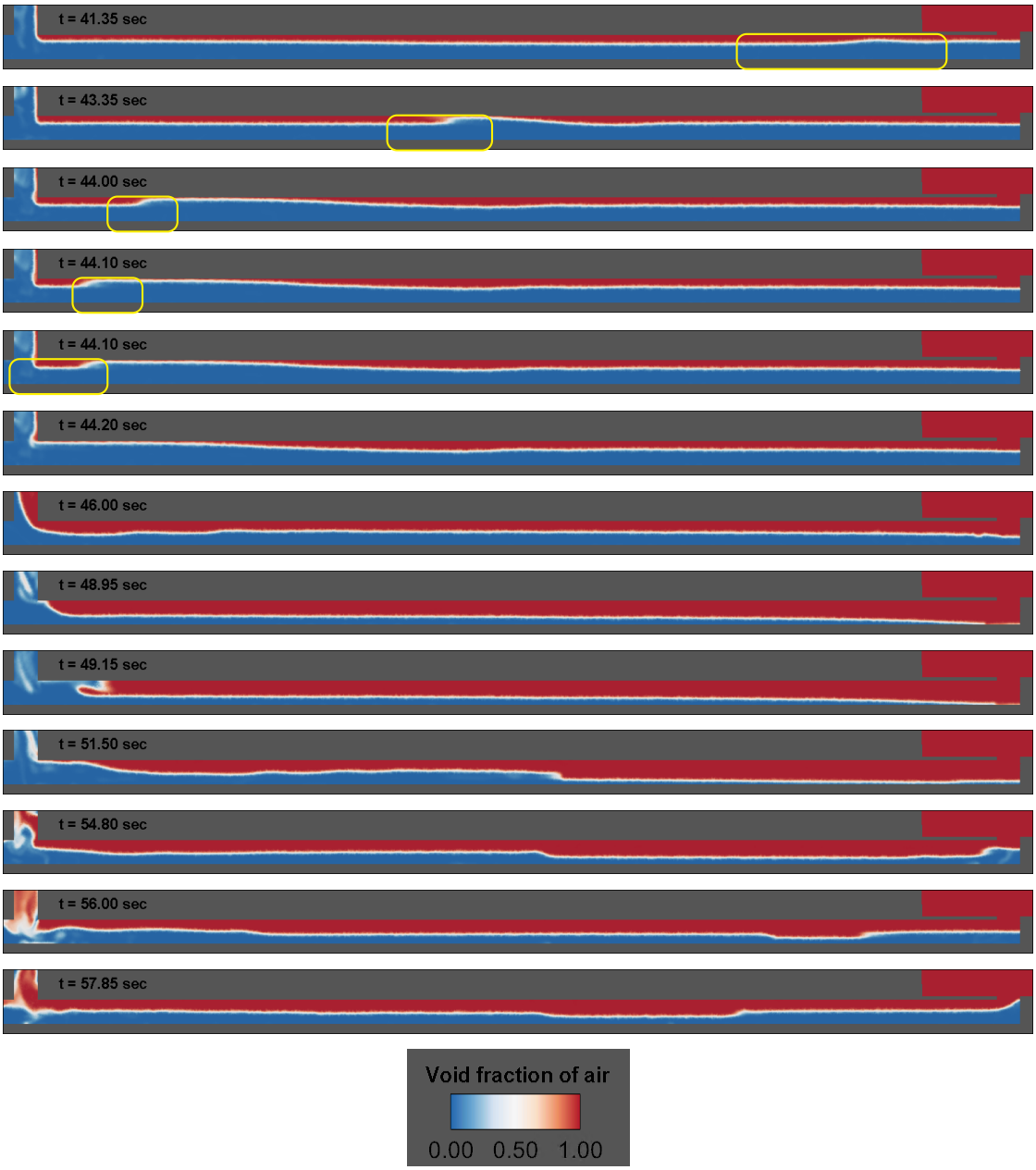

Figure 4.12: Snap shots of the void fraction of air plot are shown for Simulation B3

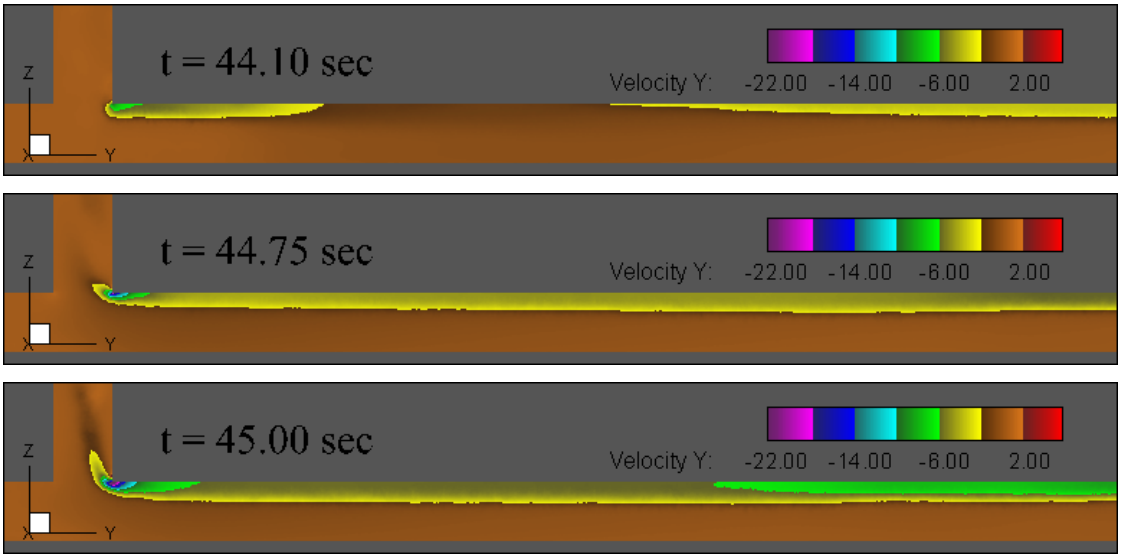

Figure 4.13: Snapshots of horizontal velocity component in the horizontal pipe is shown. At 44.10 s, a slug of water entered the vertical pipe at approximately 5 m/s. Shortly after, the air velocity in the horizontal pipe increased to 8 m/s or higher.

numerical simulation. First eruption resulted from the slug captured from 43.35 - 44.10 s. With the increased horizontal air velocity, second eruption was the highest of the five measured (Figure 4.14).

Lastly, the system becomes depressurized from loss of water (Figure 4.1.e). The experimental study reported three to eight eruptions in a time frame of two to ten seconds. As previously mentioned, total three clear and several fading amplitudes of eruptions were simulated in the numerical model. Overflows began around $t = 44$ s and all interactions were completed by $t = 50$ s.

Overall, the numerical simulation was able to capture majority of the flow features found in the physical experiment of Leon (2018). The initial entrapped air expansion, the Taylor bubble-like air rise leading to the first overflow, increased air velocity in

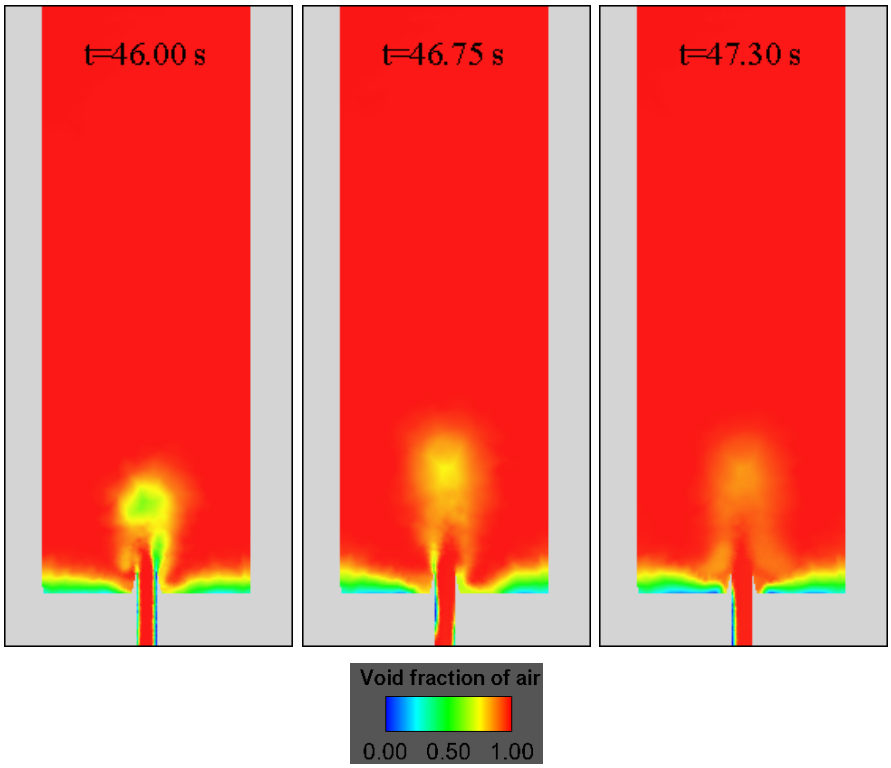

Figure 4.14: Snapshots of the first, second and third eruptions are shown. After the third eruption, the intensity and height of the overflows faded as the horizontal pipe became depressurized.

the horizontal pipe, and geyser eruptions were commonly observed in the numerical simulation and the corresponding physical experiment. However, short comings exist in the resolution of the air-water interface instability that leads to wavy and slug flows in the horizontal pipe. To verify the credibility of the numerical simulation result through a grid refinement study, this discrepancy is further discussed in the following section.

4.1.1 Grid refinement study

Comparing this result with the physical experiment of Leon (2018), the numerical simulation was not successful in capturing all of the air-water interface instabilities. The goal of the grid refinement study was to improve the grid resolution in the horizontal pipe to better capture the air-water interface instability. Simulations with improved mesh resolution were carried out to understand the cause of the discrepancy. While the available computing resource is limited at this time, the presented qualitative analysis on violent geyser eruption can nevertheless be a coherent qualitative contribution if the grid refinement can indeed improve the numerical simulation's ability to better capture important geyser flow features, such as slug formation due to instability. The characteristic mesh size in the horizontal pipe was refined from 0.01524 m to 0.00762 m and 0.00609 m while preserving the mesh resolution in the rest of the computational domain (Table 4.1).

While the three mesh sizes resulted in a consistent decompression pattern, however, the onset of the surge development in the horizontal pipe were greatly different. For the coarse grid simulation, which failed to capture the wave development early in the simulation, the first surge development in the horizontal pipe took 30 s (Figures 4.11 and 4.12). For the medium grid simulation, growth of a small surge near the bottom of the vertical pipe was captured at $t = 12.65$ s (Figures 4.16 to 4.16). As a result, the

Table 4.1: Mesh details of the meshes used in an attempt to better capture the air-water interface instability.

	Mesh	Characteristic mesh size (h)	Number of cells
Grid 1	Fine	0.00609 m	889,117
Grid 2	Medium	0.00762 m	502,081
Grid 3	Coarse	0.01524 m	152,884

(i) 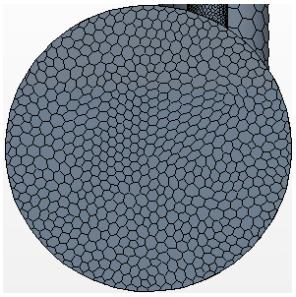 (ii) 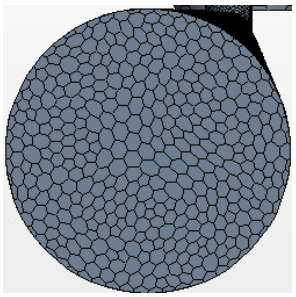 (iii) 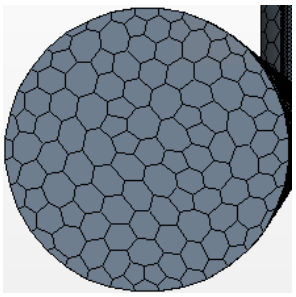

Figure 4.15: Three varying resolutions of meshes used in the grid refinement study are shown: (i) fine, (ii) medium, and (iii) coarse. For the interest of the interface instability development in the horizontal pipe, the grid size in the horizontal pipe was locally refined.

first geyser eruption was observed around $t = 13$ s. For the fine grid simulation, the growth of the initial surge was captured at $t = 11.25$ s. In addition, more number of surges continued to develop. As a result, the first geyser eruption was observed around $t = 11.45$ s. For all three simulations, the time in which the first surge arrives at the vertical pipe determined the beginning of geyser eruption.

The simulation method presented in Chapter 3 may be sufficient to capture qualitative characteristics of a violent geyser. However, if detailed mechanisms of violent geyser, such as slug formation in the horizontal pipe, must be simulated, the grid resolution must be greatly improved. The horizontal pipe diameter (D_h) in the simulations was 0.15m. For the three grid sizes used in the grid refinement study, the ratio between D_h to the mesh characteristic size (h) ranged from 10, 20, and 25. The result suggests that with an improved computing resource, the simulation approach would be able to capture critical flow features only found in the corresponding physical experiment at this time. If the grid size was refined throughout the computational domain in addition to the horizontal pipe, the discrepancy in the eruption height can also may improve.

4.2 Numerical experiment

The influence of identified system variables were studied by varying the initial air volume in the system (V_{air}) and the vertical pipe length (L_v) (Table 4.2). The vertical pipe was initially filled with water to the top, thus the change in initial volume of water in the vertical pipe, V_{water}, was directly proportional to the change in L_w. The simulation method and boundary conditions presented in Chapter 3 were applied. As determined in the previous section on the grid refinement study, the following simulations are only credible for their mean characteristics, such as the initial air pocket release, depression trend in

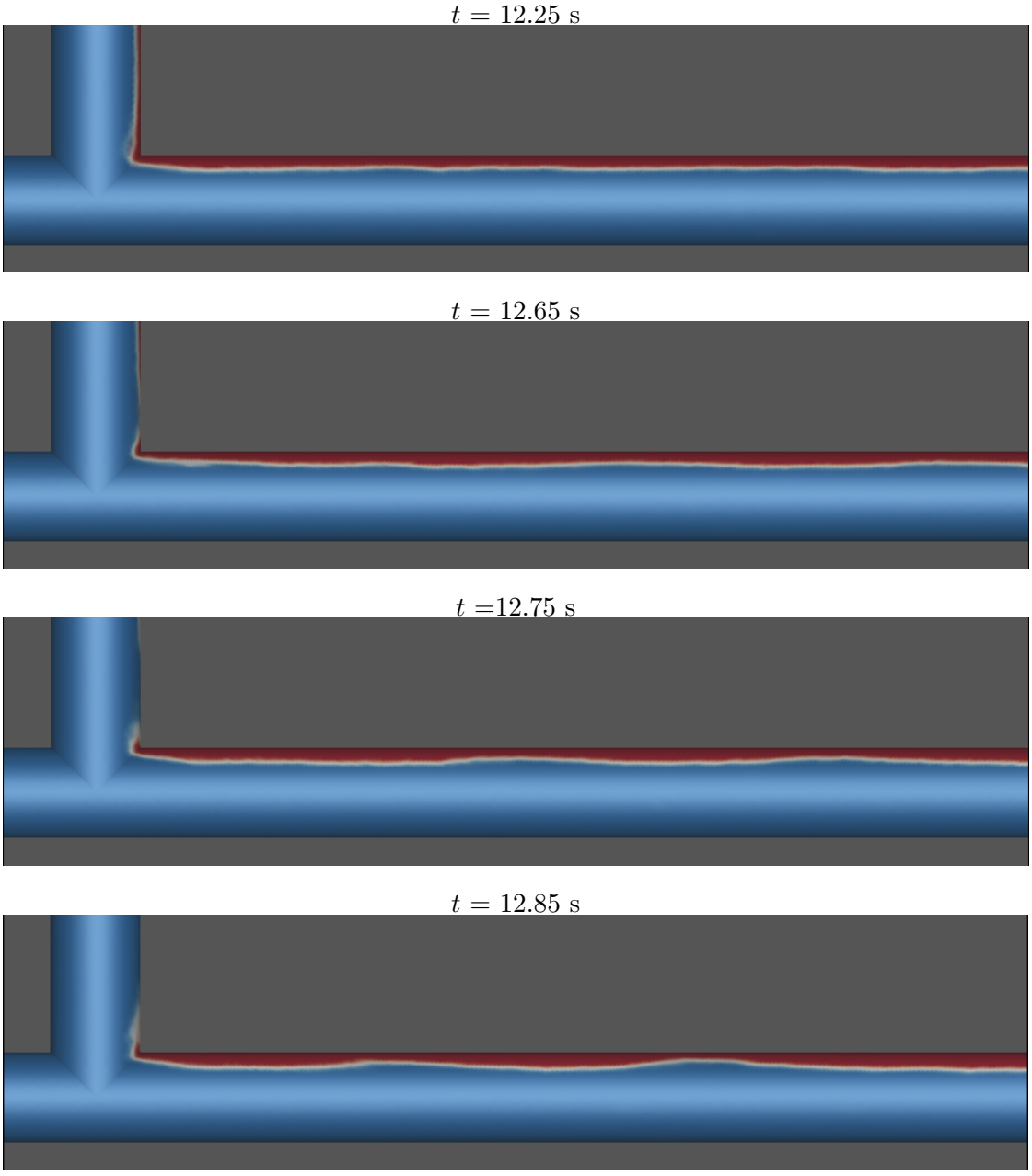

Figure 4.16: Snapshots from the medium size grid are shown.

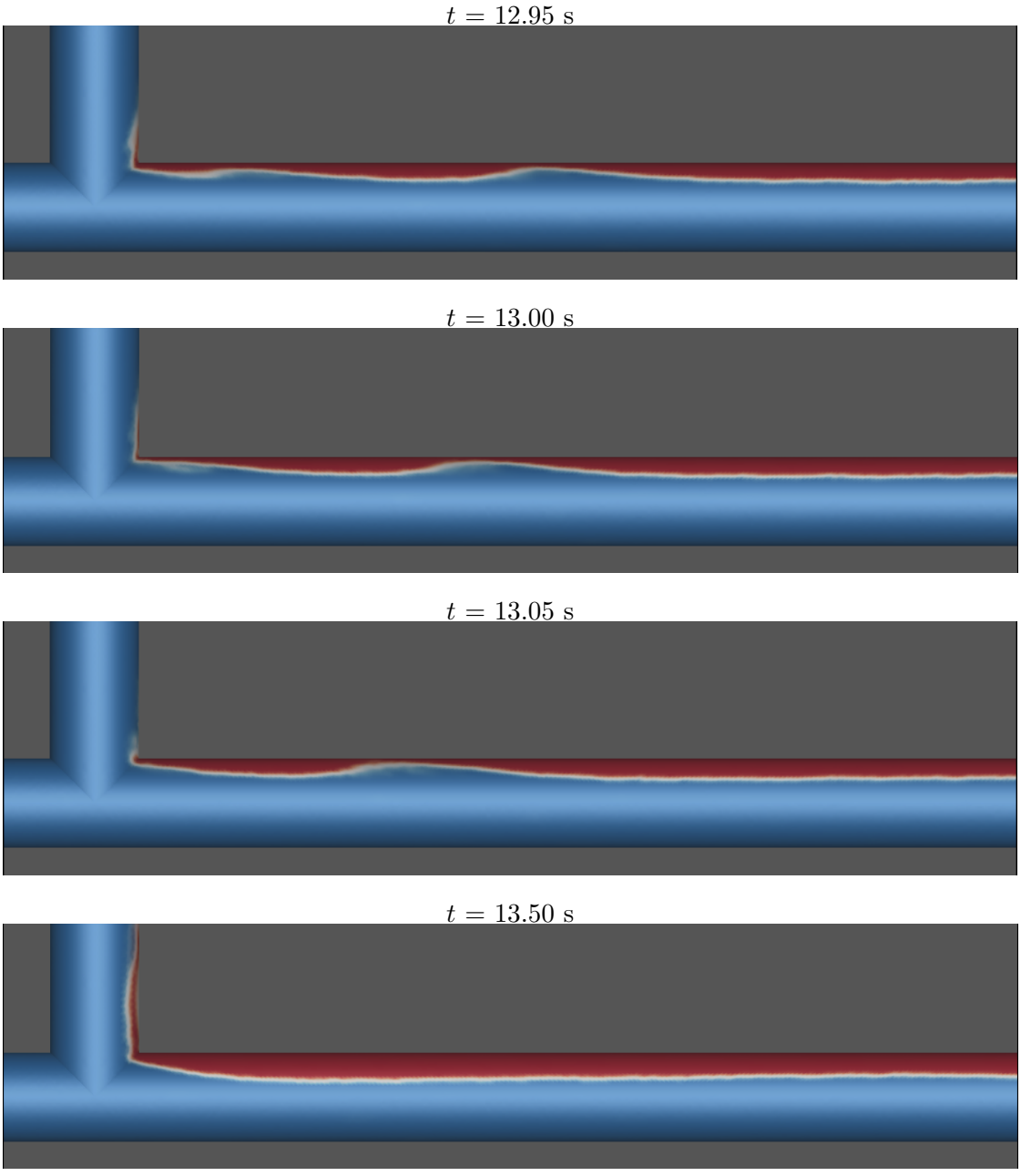

Figure 4.17: Snapshots from the medium size grid are shown.

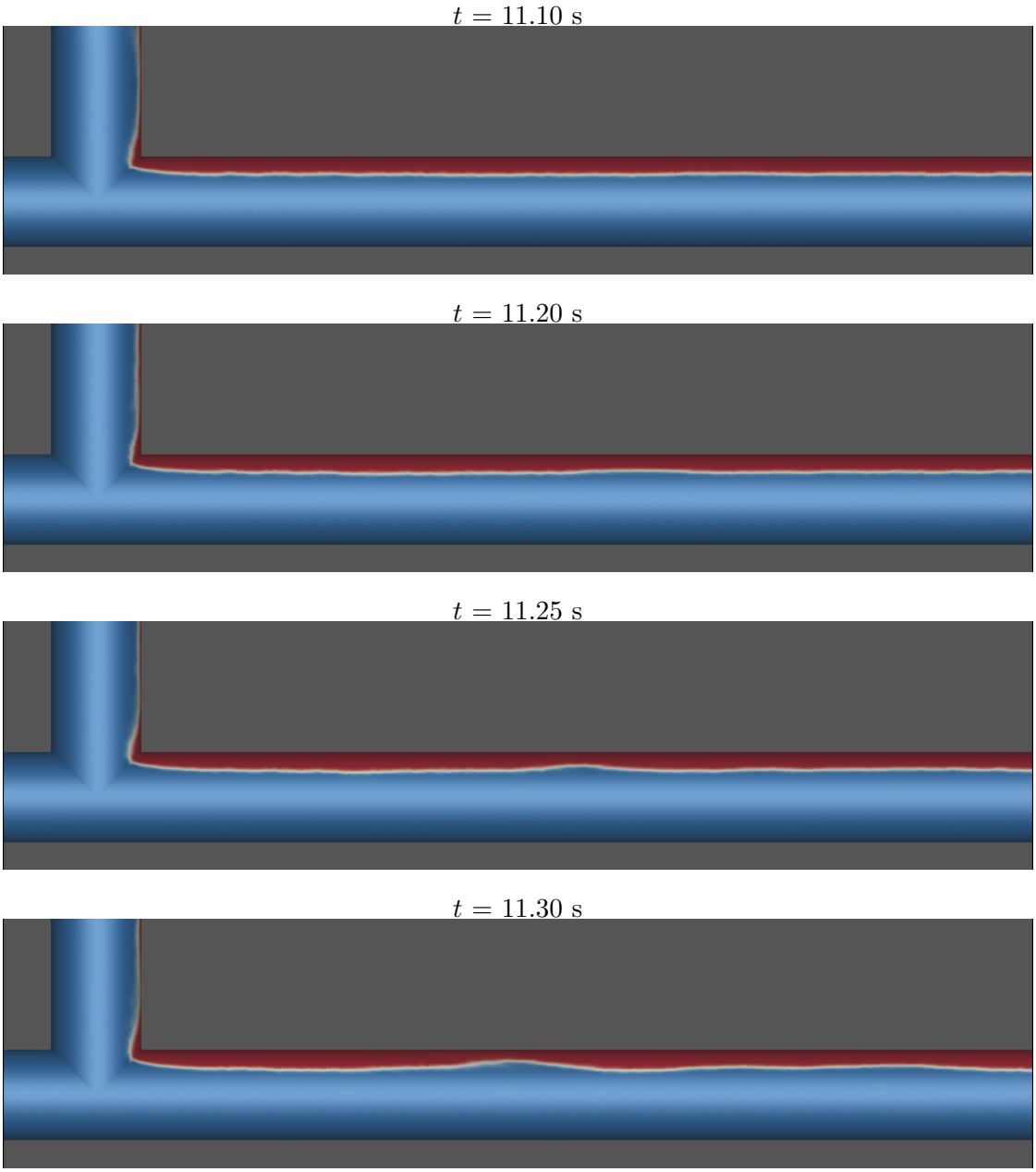

Figure 4.18: (Continued) Snapshots from the fine size grid are shown.

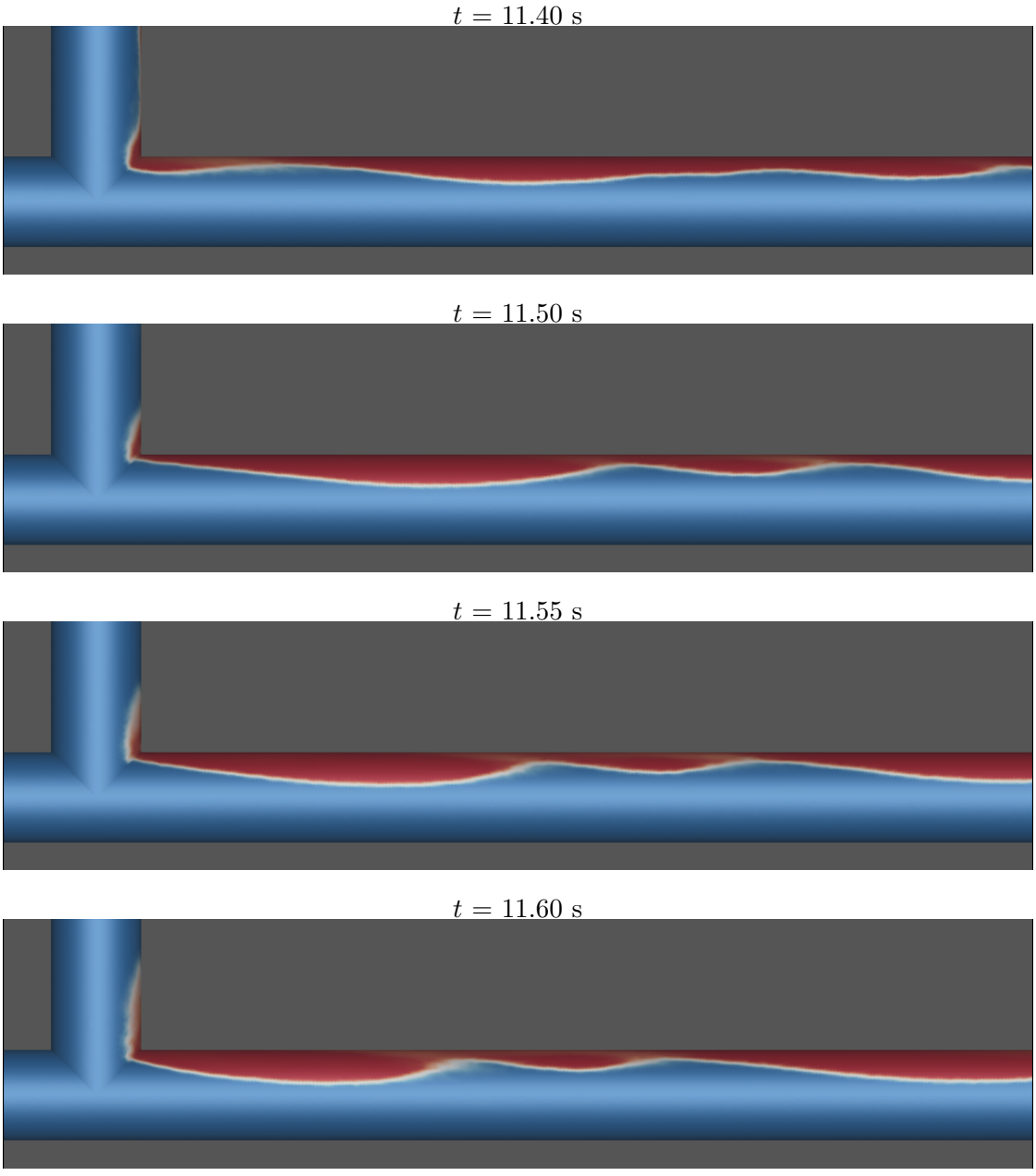

Figure 4.19: Snapshots from the fine size grid are shown.

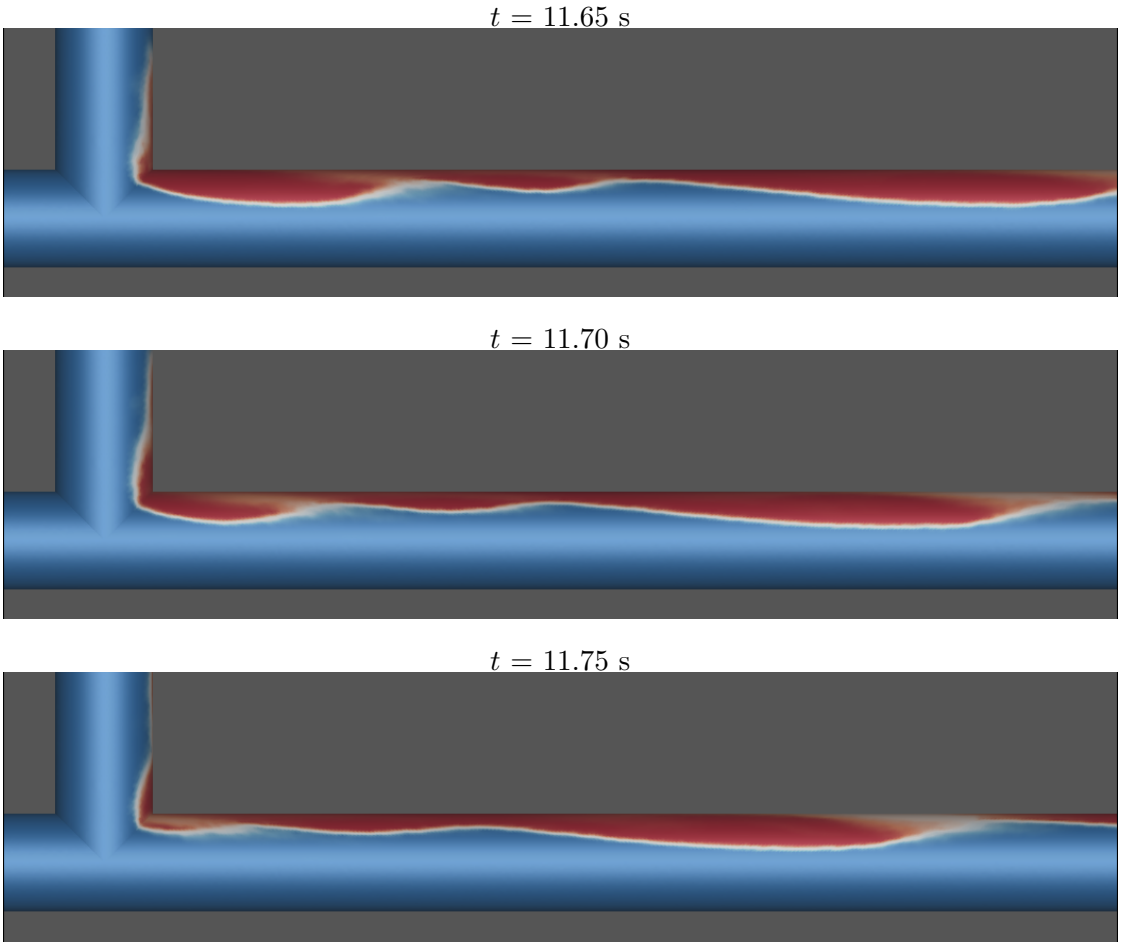

Figure 4.20: (Continued) Snapshots from the fine size grid are shown.

Table 4.2: Conducted simulations and its conditions are shown.

Simulation ID	L_v (m)	V_{air} (m^3)
A1	12	1.703
A2	12	1.278
A3	12	0.851
A4	12	0.426
B1	12	1.703
B2	9	1.703
B3	6	1.703
B4	3	1.703

the horizontal pipe, and presence or absence of violent eruptions. This is because more refined analysis would require a considerably more computationally expensive resource. In Table 4.2, initial conditions are shown for the each simulation performed. Both horizontal and vertical pipes were set to be six-inch plastic pipes and the pipe diameters were kept constant throughout the numerical experiment.

Shown in Table 4.4, L_v/D_v represents the slenderness of the vertical pipe. A larger number represents more slender pipe and the change in pipe slenderness applies to the simulation group B. $V^*_{air}V^*_{water}$ represents the product of the initially available air in the air tank and water in the vertical pipe. By reducing the air tank size in the simulation group A, the amount of initially available water proportionally ascended from A1 to A4. The reverse change resulted when the shaft height was reduced in simulation group B. The amount of initially available water proportionally descended from B1 to B4. Overall, the product of the initially available volume of air to water in the vertical pipe varied from 7134 to 28537.

Table 4.3: Conducted simulations and its conditions are shown in dimensionless forms.

Simulation ID	L_v/D_v	V_{air}/D_v^3	V_{water}/D_v^3	$V^*_{air}V^*_{water}$
	L^*_v	V^*_{air}	V^*_{water}	
A1	78	466	61	28537
A2	78	350	61	21402
A3	78	233	61	14268
A4	78	117	61	7134
B1	78	466	61	28537
B2	58	466	46	21402
B3	39	466	31	14268
B4	19	466	15	7134

4.3 Result

As previously mentioned, the numerical simulation method was not able to capture the localized pressure peaks and instabilities found in the physical experiments accurately. However, the global mean characteristics of the system pressure and some violent geyser features were reproduced using the validated simulation method.

Of the simulations performed, not all resulted in a violent geyser eruption (Table 4.4). The results are also shown graphically in Figures 4.21 through 4.24. Of the simulations resulted in violent geyser eruptions, the maximum geyser eruption height (h_g) occurred during third or fourth overflow. Also commonly found that five or more eruptions occurred in a simulation if a violent geyser was present. The eruption intensity faded away after fourth or fifth eruption as the entrapped air in the system have been exhausted and much of the available water in the vertical pipe have also exited the system. In general,

Table 4.4: The resulting h_g^* and w_v^* are shown for each conducted simulations.

Simulation ID	h_g/D_v	$w_v/\sqrt{D_v g}$	maximum eruption
	h_g^*	w_v^*	/ number of eruptions
A1	24.3	43.5	3 / 5 or more
A2	13.1	26.9	4 / 5 or more
A3	0	2.14	no geyser
A4	0	1.82	no geyser
B1	24.3	43.5	3 / 5 or more
B2	19.7	34.1	3 / 5 or more
B3	11.2	29.6	2 / 5 or more
B4	0	14.4	no geyser

higher L_v and larger V_{air} achieved h_g^* and maximum velocity in the vertical pipe (w_v^*).

In Figures 4.21 and 4.22, the changes in h_g^* and w_g^* as a function of changing independent variables are plotted. As previously discussed, the resulting h_g^* and w_g^* showed tendencies to increase as the initially available water and air in the system increased.

In Figures 4.23 and 4.24, the changes in h_g^* and w_g^* as a function of changing product of V_{air}^* and V_{water}^*. The resulting h_g^* and w_g^* showed tendencies to increase as the product of initially available water and air in the system increased.

4.4 Conclusion

As an effort to better capture violent geyser eruptions numerically, a numerical simulation was compared to the physical experiment of Leon (2018). While the numerical simulation was able to capture the global mean pressure trend and multiple geyser over-

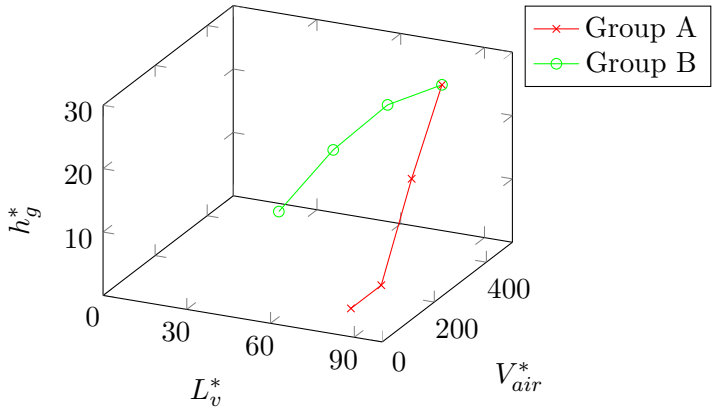

Figure 4.21: The change in h_g^* as a function of varying L_v^* and V_{air}^* is shown. For group A, the maximum height of geyser eruption grew proportionally to the initial volume of air. For group B, the maximum height of geyser eruption grew proportionally to the vertical pipe length. In some cases, geyser eruption did not occur.

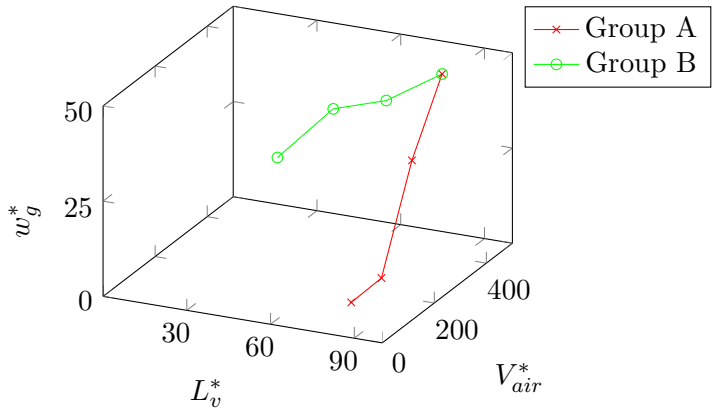

Figure 4.22: The change in w_g^* as a function of varying L_v^* and V_{air}^* is shown. For group A, the maximum vertical velocity in the vertical pipe increased as the initial volume of air increased. For group B, the maximum height of geyser eruption grew proportionally to the vertical pipe length. F

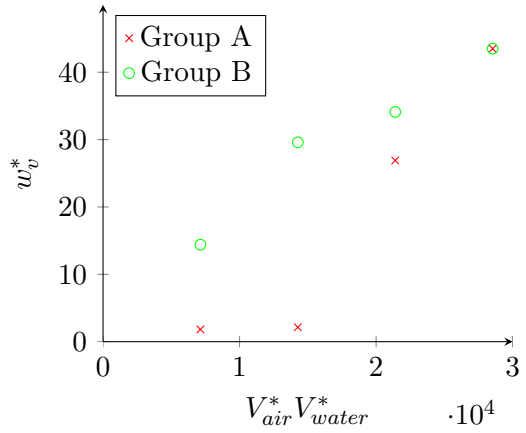

Figure 4.23: The change in w_v^* as a function of varying $V_{air}^* V_{water}^*$ is shown. For both group A and B, the maximum vertical velocity in the vertical pipe increased as the product of volume of air and water increased.

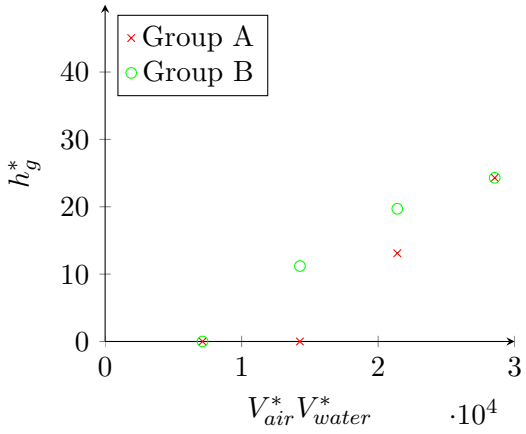

Figure 4.24: The change in h_g^* as a function of varying $V_{air}^* V_{water}^*$ is shown. For both group A and B, the maximum eruption height increased as the product of volume of air and water increased.

flows, the important geyser mechanisms such as the wavy to slug flow transition and slug formation in the horizontal pipe were not clearly simulated. The simulated geyser height was significantly lower, <10%, than the corresponding physical experiment. A grid refinement study was performed to resolve the discrepancy found in the eruption height and flow features in the horizontal pipe. The grid size in the horizontal pipe was locally refined from D_h/h=10 to 20 and 25. With the improved grid resolution, the numerical simulations were able to capture instabilities that exist in the horizontal pipe early in the simulation. As a result, in the medium and fine grid simulations, the first geyser eruption occurred approximately 30 s earlier than the coarse grid simulation. The simulations demonstrated that the occurrence of violent geyser must be preceded by one or more slugs formed in the horizontal pipe. In addition, in order to numerically capture the time in which the first geyser eruption occurs correctly, the grid resolution must be finer than $D_h/h = 20$.

The effect of two independent variables on the maximum violent geyser height, the number of eruptions and the maximum velocity in the vertical pipe were studied through a numerical experiment. With a taller vertical pipe and a larger amount of air initially available in the system, greater maximum geyser height and velocity in the vertical pipe were achieved. The numerical experiment demonstrated that of the simulations that produced geyser eruptions, the maximum geyser height was achieved not during the first eruption but second, third our fourth eruptions. Of the simulations that generated geyser eruptions, five or more eruptions were observed regardless of the initial condition. More numerical simulations must be performed to determine limiting and threshold conditions of violent geyser eruptions. For example, two simulations in the simulation group A and one simulation in the simulation group B did not result in a geyser eruption. If the two independent variables of the numerical experiment were varied at a smaller increment,

a limiting condition may have been determined.

Chapter 5: Conclusion

In this chapter, a summary of the current work is made. Answers to the previously listed research questions are provided. Finally, recommendations for future research are made.

5.1 Summary

A sewer geyser is a series of ejecting air-water mixture eruptions through vertical shafts of drainage systems. In field observed geyser incidents, manhole covers were blown into the air and they were followed by ejecting air-water mixture columns that lasted for several seconds at a time. Trapped air in sewer systems during the transition between open channel flow to pressurized flow and its release process are known to play an important role in causing sewer geysers.

The background of the topic was presented through a list of field observed cases and some key terms were defined in Chapter 1. Two naturally occurring phenomena, geothermal geysers and blow holes, provided a clue that sewer geysers must likely result from multiphase interactions in pressurized systems. Various field reported geyser incidents were discussed. Regardless of the size of the system, the amount of rain or location of the manhole, violent geyser eruptions were observed. This brief survey of the field reported geysers suggested that more extensive numerical and experimental studies must be performed to achieve further understanding of sewer geysers.

In Chapter 2, past literature studying mechanisms of sewer geyser were discussed, knowledge gap were identified and research questions were put forth. Discussed observa-

tions and experimental investigations hypothesized and confirmed a number of physical processes involved in sewer geysers. The survey of previous literature suggests that a detailed 3D simulation of the violent geyser phenomena is needed. A group of variables was assembled into dimensionless forms. This dimensional analysis was used to identify the influence of two selected variables on the geyser formation.

Numerical simulation methods were validated by reproducing published physical experiments in Chapter 3. Qualitative and quantitative characteristics of the numerical simulations were compared with the reported results of the corresponding physical experiments. The simulation method was presented in detail with referenced studies of the adapted numerical models. Two physical experiments on spring-type geysers and one physical experiment on violent geysers were reproduced. Pressure measurements made during the three physical experiments were compared with the corresponding simulation results. The adapted simulation method was found to be capable of producing spring-type geysers and mean pressure profile of violent geysers in a close proximity. The violent geyser eruption height was underestimated, likely due to grid resolution and limitation of the adapted numerical models. This discrepancy was further discussed in Chapter 4.

In Chapter 4, violent geyser simulation visualization data was compared to the physical experiment of Leon (2018). A grid refinement study was carried out to resolve the discrepancy found in the slug formation in the horizontal pipe. The effect of the two selected variables, the initially available volume of water in the vertical pipe and air in the system, on the maximum violent geyser height (h_g^*), maximum vertical velocity in the vertical pipe (w_v^*) and a number of eruptions (n) were studied through a numerical experiment. It was found that with larger volume of air in the system and taller vertical pipe, h_g^* and w_v^* increased. In the case of eruption patterns, if violent eruptions were present, the total number of eruptions were not effected by the initial condition.

Consistently, the h_g^* was achieved at the third or fourth eruption of the several.

Earlier in Chapter 1, geothermal geysers and blow holes were discussed. As speculated, a parallel can be drawn between sewer geysers and those naturally occurring geysers. Regardless of the air entrapment mechanism, geysers observed in naturally occurring geographic formations and man-maid structures, all require complex multiphase interactions between air and water. In one way or another, the system geometry and circumstances must lead to an unsteady condition (e.g., decreased hydrostatic pressure and rapid vaporization, surge formation due to incoming waves, and decreased hydrostatic pressure and surge formation at the air-water interface). For all three examples, the eruption subsided if the system became depressurized. The current study encompasses simulation methods and validation processes to numerically reproduce sewer geysers. A geyser flow is inherently unsteady and turbulent. Sophisticated and validated numerical models and simulation methods can help to advance the current understanding of sewer geysers.

5.2 Research questions

In Chapter 2, two research questions were put forth and the subsequent chapters attempted to answer them. The findings of the study can be summarized as follows;

- Can a fully three-dimensional, multiphase, Reynolds Averaged Navier-Stokes equations based, turbulence model capture the main features of violent sewer geyser observed in experimental studies? What model parameters are necessary to obtain both qualitative and quantitative match?

The presented numerical modeling approach was able to capture qualitative characteris-

tics of spring-type and violent geysers, such as an entrapped air migration in a horizontal pipe, release through a vertical pipe and internal pressure variation. In the cases of spring-type geysers, the suggested numerical simulation method was able to achieve reasonable agreements with the physical experiments in the pressure oscillation frequency and amplitude. Assuming adiabatic walls instead of an isothermal system was found to better capture the pressure amplitude decay. In the case of violent geyser simulations, the initially used characteristic mesh size (h), $1/10^{th}$ of the horizontal pipe diameter, was able to capture the mean pressure trend. However, the simulation failed to capture the slug formation in the horizontal pipe, which is one of the most important features of violent geyser eruptions. As a result, the geyser eruption height was significantly underestimated and the time took to trigger the first eruption was also delayed. It was found through the grid refinement study, the grid resolution must be finer than $D_h/h > 20$ in order to capture air-water instability in horizontal pipes which leads to multiple slug formations and potentially higher eruption heights.

- How do the two parameters varied in the numerical studies, viz. volume of initially available water in the vertical shaft (V_{water}) and air in the system (V_{air}), influence the occurrence and characteristics of the sewer geyser?

The effect of two independent variables on the maximum violent geyser height, the number of eruptions and the maximum velocity in the vertical pipe were studied. With a taller vertical pipe and a larger amount of air initially available in the system, greater maximum geyser height and velocity in the vertical pipe were achieved. As long as the geyser triggering conditions were met, the total number of eruptions were not influenced by L_v or V_{air}. Of the simulations that generated geyser eruptions, five or more eruptions were observed regardless of the initial condition. Finally, the simulations that generated

geyser eruptions consistently produced maximum eruption height during the third or fourth eruptions.

5.3 Recommendations

Presented simulations were carried out under a limited computing resource availability. With improved grid resolution and improved model parameters, the sewer geyser mechanisms will be better captured. The following list suggests ways to improve numerical modeling approaches as well as further the current understanding of violent geyser eruptions;

- As the grid refinement study suggested, the mesh refinement will result in an improved slug formation in the horizontal pipe. This can potentially result in more precise eruption height estimation and better-resolved pressure peaks. Improve the characteristic mesh size throughout the computational domain to D_h/h >20 or better (i.e., D_h/h = 30, 40 or 50).

- Expand the numerical experiment by incorporating the discussed, but not investigated variables in Equation 2.1. In addition, refine the experimental matrix resolution to identify the limiting and threshold conditions of violent geyser eruptions.

- Incorporate a fully compressible mixture interaction model to the presented simulation method. Focus on incorporating numerical models that are well suited for modeling instabilities between two immersible fluids. This will also result in improved slug formation in the horizontal pipe and improved pressure peaks. While spring-type geyser did not appear to require a fully compressible mixture interac-

tion model, the violent geyser eruptions may be influenced by the surface tension effect or compressibility of water.

APPENDICES

Appendix A: Spring-type geyser case II experiment

Experimental facility detail

Following the flow direction from the upstream to downstream, the first 6.60 m of the horizontal pipe was made of galvanized steel. The Plexiglas section of the horizontal and vertical pipes were 8.39 m and 3.05 m in length respectively. The following list of equipment were installed along the horizontal pipe; a 12 inch butterfly valve, a reducer from 12 inch to 6 inch, a 6 inch gate valve (NIBCO 40227), a five gallon air tank, the vertical pipe and a long stem gate valve (Figure A.1). The 12 inch butterfly valve could allow or completely shut off the flow in the horizontal pipe. The 6inch gate valve was installed to prevent the pressurized air from escaping against the flow direction and towards the upstream head tank. The 6 inch gate valve was fixed at a 3/4 opening throughout the conducted experiments. The five gallon air tank was installed 0.75 m downstream from the 6 inch gate valve. A hand operated ball valve controlled the release of pressurized air into the horizontal pipe. Lastly, the long stem gate valve was installed at the downstream end of the horizontal pipe. The flow rate in the horizontal pipe was varied by adjusting the opening of the long stem gate valve.

Experiment procedure and matrix

In preparation for the initial conditions, the gate valve separating the pipe system from the head tank was opened to allow flow in the horizontal pipe. The long stem gate valve regulated the flow rate in the horizontal pipe. The system came to a steady state

Figure A.1: The 12 inch butterfly valve, reducer, 6inch gate valve and air tank used in the physical experiment.

after several minutes. This was ensured by observing the flow rate in the horizontal pipe. The five gallon air tank was pressurized to a desired pressure using an air compressor. The data collection at the computer station began once the flow rate in the horizontal pipe and the pressure in the air tank reached to a desired pressure. When the experiment was triggered, a hand operated ball valve opened and the pressurized air was released to the horizontal pipe. The air propagated downstream with the flow in the horizontal pipe and eventually released through the vertical pipe. Once the pressurized air was released to the pipe system, the hand operated valve was left open until the end of the trial. Water accumulated in the air tank as a result. The air tank was drained after each experiment run. Three initial air pressure and three flow rate in the horizontal pipe were tested with five repetitions (Table A.1).

Image analysis method

Table A.1: The experimental design matrix is shown. Three flow rates, Q, and three initial air pressure, P_{air}, were tested.

P_{air} (psia/Pa abs) / Q (gpm / m^3/s)	80 /551581	60/413685	40 / 275790
180/ 0.01136	5 repeats	5 repeats	5 repeats
160/ 0.01009	5 repeats	5 repeats	5 repeats
140/ 0.00252	5 repeats	5 repeats	5 repeats

The high speed camera was fixed to a tripod. Optical illusion in the acquired images became greater towards the top of the vertical pipe due to the height limitation of the tripod. A calibration board was used to address the optical illusion prior to the image analysis. The collected images were transposed according to the optical illusion found in the calibration board. Then the image was cropped to the area of interest (Figure A.2). From the bottom of the vertical pipe, marks were made for every 1 foot interval. This indication helped to ensure the optical illusions in the collected images are properly addressed.

The air-water interface was detected using the Gaussian mixture model available within the MATLAB computer vision system toolbox (Stauffer and Grimson, 1999; KaewTraKulPong and Bowden, 2002). The images from the first fifty time step were used to detect the foreground. The detected foreground often included unwanted noise. Any parcel which contain fewer than 150 pixels were filtered out and the unique location of the air-water interface was found (Figure A.3).

Air release mechanism

Residual air accumulated along the crown of the horizontal pipe between the experiment trials. Access points were made for every 0.3048 m along the horizontal pipe

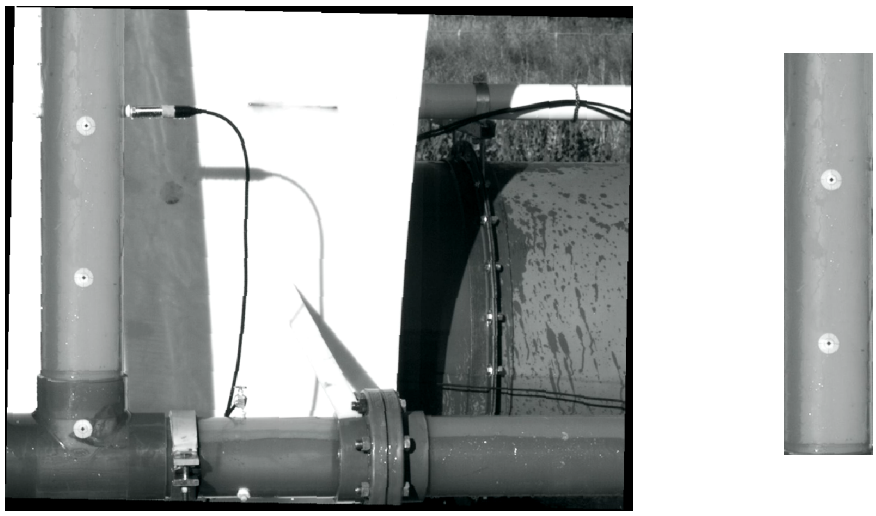

Figure A.2: The image processing steps for the field view segment 1; (a) image loaded to MATLAB and the image was transposed according to the optical illusion found using the calibration board (c) Image cropped to the vertical pipe area.

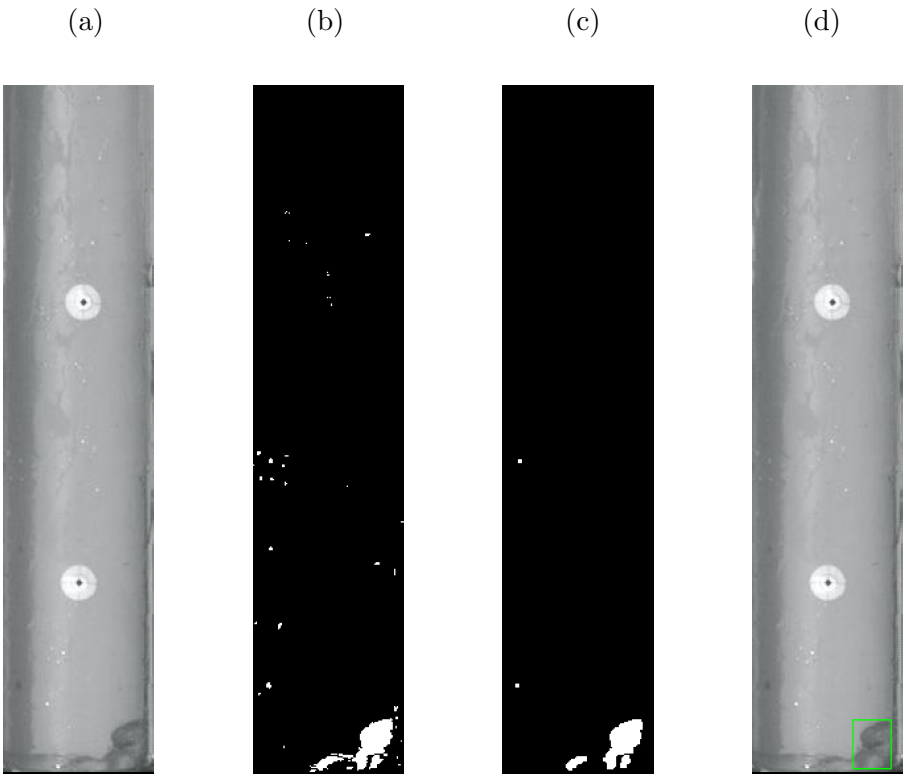

Figure A.3: Process of foreground and air-water interface detection; (a) given a cropped image, (b) the foreground was detected, (c) filtered and the air-water interface was detected, and (d) a rectangle was drawn around the air-water interface.

Figure A.4: Residual air accumulated at the crown of the horizontal pipe after each trial. Air was allowed to bleed through the valves installed along the horizontal pipe.

to release the accumulated air before then next trial begins. A copper tee mechanism assembled with a hand operated valve were installed at the access points (Figure A.4). The valves were opened to bleed accumulated air out. The data collection frequency was 1000 Hz for the pressure and flow rate. The gathered data were processed using a rational transfer function to filter the noise (Oppenheim, 1999).

Pressure measurement

The pressure in the air tank dropped rapidly to hydrostatic pressure after the valve opening. The pressure measured at other pressure transducer locations increased briefly simultaneously. This is because the initial air pressure was significantly higher than the hydrostatic pressure in the pipe system. The pressure perturbation created by introducing highly pressurized air persisted for a few seconds. The pressure returned to the

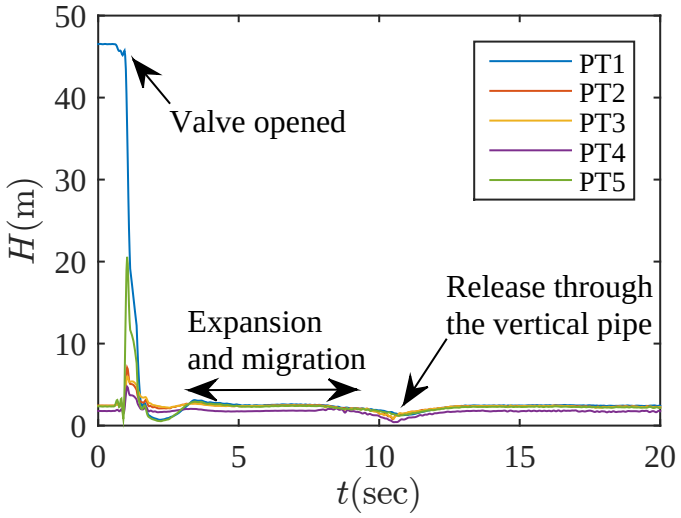

Figure A.5: Pressure head measured from the 180 gpm and 80 psia experiment is shown. Valve opening, air expansion, migration, and release through the vertical pipe are observed in the pressure time series.

hydrostatic pressure before the air pocket arrived at the bottom of the vertical pipe. The air pocket expansion front advanced up the vertical pipe and where the entrapped air was eventually released at the top.

Pressure through out the experiment facility returned to hydrostatic pressure after the valve opening regardless of the initial air pressure. Across the tested initial air pressure and flow rate combinations, the pressure variation during air release through the vertical pipe was found to be larger when the initial air pressure was higher. The advancement and release of the entrapped air occurred earlier when the flow in the horizontal pipe was larger. The process of the air expansion and release was similar across the tested initial air pressure and flow rate combinations.

Bibliography

StormChasingVideo. Interstate 35w exploding sewer stock footage, October 2012. URL http://stormchasingvideo.com/interstate-35w-exploding-sewer-stock-footage.

Staff. Predicting old faithful geyser eruptions, October 2015. URL https://www.yellowstonepark.com/things-to-do/predicting-old-faithful-eruptions.

Gopackup. Gopackup's travel stories - honolulu, oahu: Local restaurants and sites, 2017. URL https://blog.gopackup.com/en/2017/07/18/honolulu-oahu-local-restaurants-and-spots/.

USGS. Geological survey bulletin 1347 - hot water and stream phenomena, January 2007. URL https://www.nps.gov/parkhistory/online_books/geology/publications/bul/1347/sec5.htm.

JS4IV. Manitou springs flood 9/12/2013 - canon avenue manhole geyser blowing..., September 2013. URL https://youtu.be/y_Hgcl2ltSg.

NYCYankinTexas. Downtown houston flooding with dancing manhole cover and metro rail suspension, January 2012. URL https://youtu.be/t9yfdlxq09M.

screenflot. Tacoma storm surge geysers, September 2013. URL https://youtu.be/OHckNm3-LBE.

Harms J. Storm water geyser, September 2013. URL https://youtu.be/pIbonLyM7rE.

Jose G Vasconcelos and Steven J Wright. Geysering generated by large air pockets released through water-filled ventilation shafts. *Journal of hydraulic engineering*, 137 (5):543–555, 2011.

Arturo S. Leon. Mechanisms that lead to violent geysers in vertical shafts. *Journal of Hydraulic Research*, 2018.

Qizhong Guo and Charles CS Song. Dropshaft hydrodynamics under transient conditions. *Journal of hydraulic engineering*, 117(8):1042–1055, 1991.

Steven J Wright, James W Lewis, and Jose G Vasconcelos. Geysering in rapidly filling storm-water tunnels. *Journal of Hydraulic Engineering*, 137(1):112–115, 2010.

James William Lewis. *A physical investigation of air/water interactions leading to geyser events in rapid filling pipelines*. PhD thesis, University of Kentucky, 2011.

Zhiyu S Shao and Scott A Yost. Using a multiphase flow numerical model to simulate geysers in stormwater systems. In *World Environmental and Water Resources Congress 2013: Showcasing the Future*, pages 1827–1838. ASCE, 2013.

Edward R Holley. Surging in laboratory pipeline with steady inflow. *Journal of the Hydraulics Division*, 95(3):961–980, 1969.

MA Hamam and JA McCorquodale. Transient conditions in the transition from gravity to surcharged sewer flow. *Canadian Journal of Civil Engineering*, 9(2):189–196, 1982.

F Zhou, FE Hicks, and PM Steffler. Transient flow in a rapidly filling horizontal pipe containing trapped air. *Journal of hydraulic engineering*, 128(6):625–634, 2002a.

Ling Zhou, De-you Liu, and Chuan-qi Ou. Simulation of flow transients in a water filling pipe containing entrapped air pocket with vof model. *Engineering Applications of Computational Fluid Mechanics*, 5(1):127–140, 2011a.

Kathleen Z Muller, Jue Wang, and Jose G Vasconcelos. Water displacement in shafts and geysering created by uncontrolled air pocket releases. *Journal of Hydraulic Engineering*, 143(10):04017043, 2017.

DE White, RO Fournier, LJP Muffler, and AH Truesdell. Physical results of research drilling in thermal areas of yellowstone national park, wyoming. 1975.

Jay Landers. Design begins of detroit's combined sewer overflow solution, 2006.

City of Edmonton. Report on the july 4, 1995 storm event. Technical report, Drainage Branch of Transportation Dep, Edmonton, Alta. Canada, 1995.

Ibrahem S Elayeb. An experimental study on violent geysers in vertical shafts. Master's thesis, Oregon State University, 2016.

F Zhou, FE Hicks, and PM Steffler. Observations of air-water interaction in a rapidly filling horizontal pipe. *Journal of hydraulic engineering*, 128(6):635–639, 2002b.

F Zhou, F Hicks, and P Steffler. Analysis of effects of air pocket on hydraulic failure of urban drainage infrastructure. *Canadian journal of civil engineering*, 31(1):86–94, 2004a.

James Li and Alex McCorquodale. Modeling mixed flow in storm sewers. *Journal of Hydraulic Engineering*, 125(11):1170–1180, 1999.

YunJi Choi, Arturo S Leon, and Sourabh V Apte. Three-dimensional numerical modeling of air-water geyser flows. In *World Environmental and Water Resources Congress 2014: Water Without Borders*, pages 1535–1548. ASCE, 2014.

Steven J Wright, Jose G Vasconcelos, Calvin T Creech, and James W Lewis. Flow regime transition mechanisms in rapidly filling stormwater storage tunnels. *Environmental fluid mechanics*, 8(5-6):605–616, 2008.

Maurice L Albertson and JS Andrews. Transients caused by air release. *Control of flow in closed conduits*, pages 315–340, 1971.

Jing Cong, Shu Ning Chan, and Joseph HW Lee. Geyser formation by release of entrapped air from horizontal pipe into vertical shaft. *Journal of Hydraulic Engineering*, 143(9):04017039, 2017.

Ling Zhou, Deyou Liu, Bryan Karney, and Qinfen Zhang. Influence of entrapped air pockets on hydraulic transients in water pipelines. *Journal of Hydraulic Engineering*, 137(12):1686–1692, 2011b.

YunJi Choi, Arturo S Leon, and Sourabh V Apte. A one-dimensional numerical model to predict pressure and velocity oscillations of a compressed air pocket in a vertical shaft filled with water. In *World Environmental and Water Resources Congress 2016*, pages 202–211. ASCE, 2016.

Shu Ning Chan, Jing Cong, and Hun Wei Joseph Lee. Numerical modeling of geyser formation by release of entrapped air from horizontal pipe into vertical shaft. 2016.

Star-CCM+ V10 User Guide. Star-ccm+ version 10.04. *CD-adapco-2015*, 2015.

BE Launder, G Jr Reece, and W Rodi. Progress in the development of a reynolds-stress turbulence closure. *Journal of fluid mechanics*, 68(03):537–566, 1975.

David C Wilcox. Reassessment of the scale-determining equation for advanced turbulence models. *AIAA journal*, 26(11):1299–1310, 1988.

Praa Spalart and S Allmaras. A one-equation turbulence model for aerodynamic flows. In *30th aerospace sciences meeting and exhibit*, page 439, 1992.

David C Wilcox. A half century historical review of the k-omega model. In *29th Aerospace Sciences Meeting*, page 615, 1991.

Philippe R Spalart. Strategies for turbulence modelling and simulations. *International Journal of Heat and Fluid Flow*, 21(3):252–263, 2000.

T-H Shih, WW Liou, A Shabbir, Z Yang, and J Zhu. A new k-epsilon eddy viscosity model for high reynolds number turbulent flows: Model development and validation. 1994.

W1 Rodi. Experience with two-layer models combining the k-epsilon model with a one-equation model near the wall. In *29th AIAA Aerospace Sciences Meeting*, volume 1, 1991.

S Sarkar and B Lakshmanan. Application of a reynolds stress turbulence model to the compressible shear layer. *AIAA journal*, 29(5):743–749, 1991.

Thibauld Jongen. Simulation and modeling of turbulent incompressible fluid flows. 1998.

M Wolfshtein. The velocity and temperature distribution in one-dimensional flow with turbulence augmentation and pressure gradient. *International Journal of Heat and Mass Transfer*, 12(3):301–318, 1969.

H Reichardt. Vollständige darstellung der turbulenten geschwindigkeitsverteilung in glatten leitungen. *ZAMM-Journal of Applied Mathematics and Mechanics/Zeitschrift für Angewandte Mathematik und Mechanik*, 31(7):208–219, 1951.

BA Kader. Temperature and concentration profiles in fully turbulent boundary layers. *International Journal of Heat and Mass Transfer*, 24(9):1541–1544, 1981.

Tuncer Cebeci and P Bradshaw. Momentum transfer in boundary layers, hemisphere publ. *Corp., Washington-London*, 1977.

Venkat Venkatakrishnan. Convergence to steady state solutions of the euler equations on unstructured grids with limiters. *Journal of computational physics*, 118(1):120–130, 1995.

Samir Muzaferija and M Peric. Computation of free-surface flows using interface tracking and interface-capturing methods. *Advances in Fluid Mechanics*, 24:59–100, 1999.

JU Brackbill, Douglas B Kothe, and Charles Zemach. A continuum method for modeling surface tension. *Journal of computational physics*, 100(2):335–354, 1992.

R Byron Bird. Transport phenomena. *Applied Mechanics Reviews*, 55(1):R1–R4, 2002.

Joel H Ferziger and Milovan Peric. *Computational methods for fluid dynamics*. Springer Science & Business Media, 2012.

M Perić, R Kessler, and G Scheuerer. Comparison of finite-volume numerical methods with staggered and colocated grids. *Computers & Fluids*, 16(4):389–403, 1988.

J Pierrus and OL De Lange. Experimental and theoretical study of adiabatic, intermediate, and isothermal oscillations in air. *Physical Review E*, 56(3):2841, 1997.

Patrick J Roache. Quantification of uncertainty in computational fluid dynamics. *Annual review of fluid Mechanics*, 29(1):123–160, 1997.

Chris Stauffer and W Eric L Grimson. Adaptive background mixture models for real-time tracking. In *Computer Vision and Pattern Recognition, 1999. IEEE Computer Society Conference on.*, volume 2, pages 246–252. IEEE, 1999.

Pakorn KaewTraKulPong and Richard Bowden. An improved adaptive background mixture model for real-time tracking with shadow detection. In *Video-based surveillance systems*, pages 135–144. Springer, 2002.

Alan V Oppenheim. *Discrete-time signal processing*. Pearson Education India, 1999.

F Zhou, FE Hicks, and PM Steffler. Closure to "transient flow in a rapidly filling horizontal pipe containing trapped air" by f. zhou, fe hicks, and pm steffler. *Journal of Hydraulic Engineering*, 130(1):85–87, 2004b.

V Frei. Huge montreal rainfalls create flooding that nearly blows manhole cover off, September 2015. URL https://youtu.be/pIbonLyM7rE.

E.B. Wylie and V.L. Streeter. *Fluid transients*. FEB Press, 1983. URL https://books.google.com/books?id=M_xRAAAAMAAJ.

J Paul Tullis. *Hydraulics of pipelines: Pumps, valves, cavitation, transients*. John Wiley & Sons, 1989.

B Brunone, UM Golia, and M Greco. Modelling of fast transients by numerical methods. In *Proc. Int. Conf. on Hydr. Transients With Water Column Separation*, pages 273–280, 1991a.

B Brunone, UM Golia, and M Greco. Some remarks on the momentum equation for fast transients. In *Proc. Int. Conf. on Hydr. Transients With Water Column Separation*, pages 201–209, 1991b.

Giuseppe Pezzinga. Quasi-2d model for unsteady flow in pipe networks. *Journal of Hydraulic Engineering*, 125(7):676–685, 1999.

Giuseppe Pezzinga. Evaluation of unsteady flow resistances by quasi-2d or 1d models. *Journal of Hydraulic Engineering*, 126(10):778–785, 2000.

A Vardy and J Brown. On turbulent, unsteady, smooth-pipe friction. In *Bhr Group Conference Series Publication*, volume 19, pages 289–312. MECHANICAL ENGINEERING PUBLICATIONS LIMITED, 1996.

City of San Diego. Sewer design guide (revised may, 2015, 2015. URL https://www.sandiego.gov/sites/default/files/legacy/mwwd/pdf/sewerdesign.pdf.

Dumitru Theodor Dumitrescu. Strömung an einer luftblase im senkrechten rohr. *ZAMM-Journal of Applied Mathematics and Mechanics/Zeitschrift für Angewandte Mathematik und Mechanik*, 23(3):139–149, 1943.

Zai-Sha Mao and AE Dukler. An experimental study of gas-liquid slug flow. *Experiments in Fluids*, 8(3-4):169–182, 1989.

R Moissis and P Griffith. Entrance effects in a two-phase slug flow. *Journal of Heat Transfer*, 84(1):29–38, 1962.

Eugenia-Teodora Tudose and M Kawaji. Experimental investigation of taylor bubble acceleration mechanism in slug flow. *Chemical engineering science*, 54(23):5761–5775, 1999.

Arturo S. Leon, Ibrahem S. Elayeb, and Yun Tang. An experimental study on violent geysers in vertical pipes. *Journal of Hydraulic Engineering (accepted)*, 2018.

Michael Pfister and Hubert Chanson. Two-phase air-water flows: Scale effects in physical modeling. *Journal of Hydrodynamics, Ser. B*, 26(2):291–298, 2014.

Safa Sharaf, Maria Zednikova, Marek C Ruzicka, and Barry J Azzopardi. Global and local hydrodynamics of bubble columns–effect of gas distributor. *Chemical Engineering Journal*, 288:489–504, 2016.

E Kordyban. Horizontal slug flow: a comparison of existing theories. *Journal of fluids engineering*, 112(1):74–83, 1990.

John W Miles. On the generation of surface waves by shear flows part 3. kelvin-helmholtz instability. *Journal of Fluid Mechanics*, 6(4):583–598, 1959.

Raoyang Zhang, Xiaoyi He, Gary Doolen, and Shiyi Chen. Surface tension effects on two-dimensional two-phase kelvin–helmholtz instabilities. *Advances in water resources*, 24 (3-4):461–478, 2001.

DI Pullin. Numerical studies of surface-tension effects in nonlinear kelvin–helmholtz and rayleigh–taylor instability. *Journal of Fluid Mechanics*, 119:507–532, 1982.